Light manipulation and optical imaging through complex media

Rui Luís Vieira Oliveira

Mestrado Integrado em Engenharia Física

Departamento de Física e Astronomia

2018

Orientador

Prof.ª Dra. Carla C. Rosa, Faculdade de Ciências da Universidade do Porto, e
Instituto de Engenharia de Sistemas e Computadores, Tecnologia e Ciência

INESCTEC
ASSOCIATE LABORATORY
PORTUGAL

U.PORTO
FEUP FACULDADE DE ENGENHARIA
UNIVERSIDADE DO PORTO

U.PORTO
FC FACULDADE DE CIÊNCIAS
UNIVERSIDADE DO PORTO

Todas as correções determinadas
pelo júri, e só essas, foram efetuadas.

O Presidente do Júri,

Porto, ______/______/________

MSc

UNIVERSIDADE DO PORTO

MASTERS THESIS

Light manipulation and optical imaging through complex media

Author:
Rui L. V. OLIVEIRA

Supervisor:
Carla C. ROSA

A thesis submitted in fulfilment of the requirements
for the degree of MSc. Engineering Physics

at the

Faculdade de Ciências da Universidade do Porto
Departamento de Física e Astronomia

December 3, 2018

"When life gives you lemons, don't make lemonade. Make life take the lemons back! Get mad! I don't want your damn lemons, what the hell am I supposed to do with these? Demand to see life's manager! Make life rue the day it thought it could give Cave Johnson lemons! Do you know who I am? I'm the man who's gonna burn your house down! With the lemons! I'm gonna get my engineers to invent a combustible lemon that burns your house down!"

J. K. Simmons as *Cave Johnson*,
written by Erik Wolpaw, Jay Pinkerton and Chet Faliszek

Acknowledgements

This work would not have been possible without the support of countless individuals and their contribution to this work.

First and foremost, I would like to thank my supervisor, professor Carla Rosa, for the opportunity to work with her and for all the guidance, whilst never clipping my freedom to pursuit my own research ideas. She presented the world of advanced optical imaging to me, for which I am grateful.

Second, I would like to present my gratefulness to key individuals at the Centre for Applied Photonics: professor Orlando Frazão, for first bringing me into CAP and professor Paulo Marques in his role of centre coordinator, who always made sure the necessary tools for our research were available.

I would also like to acknowledge the funding sources for this project: the North Portugal Regional Operational Programme (NORTE 2020), and the European Regional Development Fund (ERDF).

I also want to leave a most sincere acknowledgement to my family for their love and support. They always provided unconditional support for my career choices.

Finally, I would like to thank to all my friends. To my friends at the university for the company at lunch breaks and all the interesting discussion, even though we research different topics. And to my other friends for their understanding in these busy times. Their support helped keeping a positive morale at all times.

UNIVERSIDADE DO PORTO

Abstract

Faculdade de Ciências da Universidade do Porto
Departamento de Física e Astronomia

MSc. Engineering Physics

Light manipulation and optical imaging through complex media

by Rui L. V. OLIVEIRA

When light propagates through a diffuse medium, it gets scattered and all the spatial information it was carrying is scrambled. However, scrambled does not mean lost. In this work, we explore techniques for imaging and wavefront control through complex media.

Firstly, we explore how we can image object behind diffuse media using the so-called *shower curtain effect*. We demonstrate how the exploitation of far-field conditions for semi-coherent light and the properties of thin diffusers can be used to retrieve the autocorrelation function of an object behind the diffuser. Phase retrieval algorithms are then used for reconstructing the object from its autocorrelation. We show our results, where we were able to image complex patterns using this technique in a scenario where direct observation yields no apparent object information. The results include objects whose patterns could not be seen directly being retrieved without the use of microscopy optics.

For our second experiment, we managed to manipulate light through a diffuse medium via the *transmission matrix characterization*. Resorting to a calibration procedure, using a phase-only spatial light modulator, and without using a two-arm interferometric setup, we managed to measure the complex-valued input-output response of the modes propagating in the diffuse medium. We use this knowledge to generate a tight focused spot at the output of the diffuse medium. This can be useful both for imaging and for micro-manipulating small particles. The speed at which the medium can be characterized can be vastly improved by replacing the spatial light modulator with the significantly faster digital micro-mirror device and Lee holography as a source for phase modulation.

For the third and last experiment, we demonstrate the ability to arbitrarily manipulate light through both a diffuse medium and an optical fibre using *optimization algorithms*.

We generate a single focused spot, multiple focused sports and arbitrary wavefronts after these complex media using this algorithm. Again, this presents a very interesting approach for imaging and light manipulation. This technique can develop into a real-time manipulation technique through dynamic media using a digital micro-mirror device.

Overall, the developed, and now presented work, provides a solid base in the area of imaging and wavefront shaping through complex media, opening up pathways for interesting developments in this subject.

UNIVERSIDADE DO PORTO

Resumo

Faculdade de Ciências da Universidade do Porto
Departamento de Física e Astronomia

Mestrado Integrado em Engenharia Física

Manipulação de luz e imagiologia ótica em meios complexos

por Rui L. V. OLIVEIRA

Quando raios de luz atravessam um meio difuso, eles são espalhados, misturando a informação que transportavam. Contudo, misturado não significa perdido. Neste trabalho, exploramos técnicas para controlo da frente de onda da luz propagada por meios difusos e para imagem ótica através destes meios.

Em primeiro lugar, exploramos como podemos recuperar informação sobre um objeto escondido atrás de um meio difuso usando o chamado método da cortina de chuveiro. Demonstramos como podemos explorar as propriedades da difração a campo distante e de luz semi-coerente, em conjunto com as características de meios difusos finos para obter informação sobre a autocorrelação do objeto escondido atrás do meio difuso. Depois, fazemos uso de algoritmos de recuperação de fase para reconstruir os objetos a partir da informação da autocorrelação. Os resultados demonstram a capacidade de fazer imagem de padrões complexos usando esta técnica, inclusivamente de objetos com detalhes que obrigariam ao uso de óticas de microscopia quando vistos por sistemas óticos convencionais.

A nossa segunda experiência prende-se com manipulação de luz através de meios difusos por via da caracterização da matriz de transmissão do meio. Recorrendo a um processo de calibração, usando um modulador espacial da fase da luz, mas sem precisar de um sistema interferométrico de dois braços, fomos capazes de medir a relação de amplitude e fase entre os modos de propagação de entrada e de saída do meio difusor. Fizemos uso desta caracterização para gerar um foco de luz à saída do meio difuso. Este sistema pode ser aplicado em imagiologia ótica ou em micromanipulação de pequenas partículas. A velocidade de caracterização do meio pode ser melhorada recorrendo a um controlador digital de micro-espelhos e usando holografia de Lee como fonte de modulação de fase.

Na nossa terceira e ultima experiencia, demonstramos a capacidade para manipular luz através de meios difusos e de fibra ótica usando algoritmos de otimização. Como prova de conceito, fomos capazes de gerar, à saída do meio difusor, um ou múltiplos focos de luz e formas arbitrárias de frente de onda. Esta técnica, tal como a anterior, é promissora nas áreas de imagiologia ótica e micromanipulação de partículas. Esta técnica tem o potencial de ser transformada numa técnica para controlo de frentes de onda por meios difusos dinâmicos em tempo real com o uso de um controlador digital de micro-espelhos.

O trabalho realizado e apresentado neste documento providência uma base sólida nas áreas de imagiologia e controlo de frente de onda por meios complexos, abrindo caminho para futuros desenvolvimentos na área.

Contents

List of Figures

Glossary

CCD	Charge-Coupled Device (camera)
CMOS	Complementary Metal-Oxide-Semiconductor
CW	Continuous Wave
DMD	Digital Micromirror Device
(F)FT	(Fast) Fourier Transform
FOV	Field-of-view
FPGA	Field Programmable Gate Array
MOEMS	Micro-Opto-Electromechanical System
MMF	Multimode Fibre
MMFI	Multimode Fibre Imaging
NA	Numerical Aperture
PSF	Point Spread Function
RoI	Region of Interest
SBC	Single Board Computer
SCE	Shower Curtain Effect
SLM	Spatial Light Modulator
SNR	Signal-to-Noise ratio
TLI	Turbid Lens Imaging
TM	Transmission Matrix
TMI	Turbid Media Imaging

Chapter 1

Introduction

Vision is a fundamental part of human, and essentially of all animal life. From navigating through terrain to reading these lines of text, an imaging system is in permanent use: our own eyes (eventually with the aid of a pair of glasses or contact lenses). Very early, humankind realized the need to extend its own capabilities: Sines and Sakellarakis' book "*Lenses in antiquity*" [1] suggests the use of primitive lenses as burning glasses or magnifying glasses. As soon as year 77 A.D., Pliny the Elder, on his work "*Natural history*" [2] confirms the use of lenses as a burning glass and mentions that the Roman emperor Nero himself used an emerald lens as corrective lens for his vision. Fast forwarding a millennium to early modem Europe and we have navigators using spyglasses for long range scouting. Then Galileo Galilei decided to point his telescope up to the sky, leaving a mark in astronomy, contributing valuable observations and methods used for acquiring such data. These are, without a doubt, of the uttermost historical relevance to the field. At the same time, painters were using pinhole chambers (the "*Camera Obscura*", or "dark chamber") to image the view from the workshop, allowing easy tracing of the scene. Couple hundred years go by and mankind finds itself taking photographs: an imaging system images an object into a photosensitive material from which the image could be retrieved after chemical processing. Half a century later and the advent of silicon technology gives us digital cameras, with photo-electric transducers, ways of digitally storing that information and displays to watch it back. In the meanwhile, humanity realized that optical systems could do more than just magnification and correction: several exotic imaging techniques were born: fluorescent microscopy, optical coherence tomography (OCT), super-resolution microscopy, light-sheet photography, to name a few. This meant that all of a sudden we were seeing what could not be seen before. Of course, at the same time, non-optical imaging techniques also emerged, like x-ray imaging, magnetic resonance, ultrasonic imaging and others, but those are out of the scope of this work.

There is, however, something that all traditional optical imaging techniques cannot escape from: the medium where light propagates must have as much optical transparency as possible. We, as humans, can't see through dense fog, neither can optical cameras. Glasses can correct for errors in the curvature of the eye but they cannot correct for cataracts. This means that not all is done. And as with any scientific and technological progress, we start with a question, a challenge:

> How can we image an object that's behind or enclosed on a medium where light does not propagate trivially? How can we manipulate light propagating in these media?

Answering the above-mentioned questions was the proposed challenge, resulting in this document which is the keystone of work developed in the context of achieving masters degree in engineering physics from Faculdade de Ciências da Universidade do Porto.

The work was developed at the Centre for Applied Photonics (CAP) of Instituto de Engenharia de Sistemas e Computadores, Tecnologia e Ciência (INESC-TEC) in the context of the project NanoSTIMA: Macro-to-Nano Human Sensing: Towards Integrated Multimodal Health Monitoring and Analytics[*]. NanoSTIMA's philosophy is that human sensing is shifting from a macro clinical diagnosis paradigm to one where individuals would rather use nano-scale (in a broad sense), personal devices for monitoring and diagnosis.

In this context, the work developed aims to tackle the specific problem of imaging and manipulating light through biological tissue. With this contribution, we aim to contribute to a final goal of simple optical systems for *"in-vivo"* microscopy, namely single multimode fibre as means for an all-optical, minimally invasive, ultra-thin endoscopy. Other applications include direct imaging of objects of interest that are enclosed in biological tissue, a situation where traditional optical microscopy is not capable of providing any information.

---

[*] NanoSTIMA: Macro-to-Nano Human Sensing: Towards Integrated Multimodal Health Monitoring and Analytics/NORTE-01-0145-FEDER-000016" is financed by the North Portugal Regional Operational Programme (NORTE 2020), under the PORTUGAL 2020 Partnership Agreement, and through the European Regional Development Fund (ERDF).

1.1 The problem of light control through complex media: State of the Art

The problem is now set: We want to be able to control light through complex media[*]. The obvious question arises:

> What is the way to approach these problems?

Many have questioned themselves before about either manipulating light or imaging objects through complex media. To the broad set of techniques to image through complex, diffuse media we call **turbid media imaging** (TMI). The problem of imaging through multimode fibres shall be referred as **multimode fibre imaging** (MMFI).

In the case of general diffuse media, we can imagine the problem as a scattering one: light coming from an object is scrambled when photons scatter on the particles of the turbid medium. In the case of light travelling through multimode fibre optics, the scrambling problem is modelled differently: light from the object will couple to different modes on the fibre which travel at different speeds, due to them having different effective refractive indexes. These modes will interfere in a way that's not possible to accurately model theoretical. Furthermore, any bending or defects on the fibre will change the way modes interact and propagate.

Despite the different nature of the scrambling of information carried by light travelling through diffuse materials and fibre optics, they share a number of common behaviours that are exploitable for imaging. This will become more evident throughout the document, as relevant properties are discussed.

It is worth to make a tour through the past and present of the single multimode fibre imaging problem, due to the cumbersome variety of approaches to these problems. We shall now discuss the most relevant techniques.

1.1.1 The 1990s: pulsed laser, time-gated or polarization-locked imaging techniques

Going all the way back to 1990, one can find some of the first approaches to solving the scattering media problem: before the advent of readily available high computational

---

[*] Throughout this document, the expression "light manipulation/control" can include the action of imaging. Likewise, complex media can refer to either bulky scattering materials or fibre optics. The reader is advised to be aware of the context.

power, the approach chosen by authors like Andersson-Engels et al. [3], Leith et al. [4], or Das et al. [5] was to use a very simple assumption about the light travelling through scattering medium: scattered photons should travel a lesser distance, and therefore have a smaller time of flight between the source and the detector. The idea of time gating is born: using ultrafast lasers, with very short pulses and very well synchronized electronics one could open the integration window of the detector during the spawn of ballistic photons[*], as whereas any other light is considered noise. Therefore, the shape of objects enclosed in even highly scattering media could be resolved.

In 1998, Ramachandran and Narayanan [6] take this technique a step further, releasing a paper titled "*Two-dimensional imaging through turbid media using a continuous wave light source*". The scheme presented is a transmission imaging system where continuous wave (CW) laser light polarization modulation is used to resolve the image. Horinaka et al. [7] established the equivalence between temporal gating (used on imaging methods based on pulsed lasers techniques) and polarization modulation, providing the theoretical ground for this imaging technique. Demos and Alfano [8, 9] applied this principle on pulsed laser schemes and Emile et al. [10] built a continuous wave (CW) laser imaging scheme. In their setup (figure 1.1), a laser beam crosses a half-wave plate (HWP) rotating at an angular velocity Ω, effectively rotating the polarization at 2Ω. Two pin-hole apertures (A_1 and A_2) limit the illuminated area, contributing the most to the resolution limit of the system. The turbid medium contained the object of interest is placed on a 2-axis translation stage. Polariser P serves as an analyser and the photomultiplier detector D is connected to a lock-in amplifier that takes Ω as centre of its bandwidth filter. This allows to pick out the ballistic component of the light over the diffused one, effectively creating a spot-scanning imaging system.

Later, in 2004, Mujumdar and Ramachandran [11] studied the dependence on scattering anisotropy for this kind of technique. Ramachandran and Narayanan's method used a combination of temporal and spatial Fourier transforms for imaging. A spatial filter is used instead of two pinholes, allowing for recording on a camera sensor array, ditching the need for a translation stage and scanning image. This imaging scheme is depicted in figure 1.2. In their system, a rotating polariser (or HWP if using linearly polarized laser light) rotates at an angular speed ω and shines upon the turbid medium with the object

---

[*] In this document, it is adopted the terminology used by many of the authors cited in this chapter where the word ballistic refers to photons that don't suffer significant scatter in their travel through the turbid medium

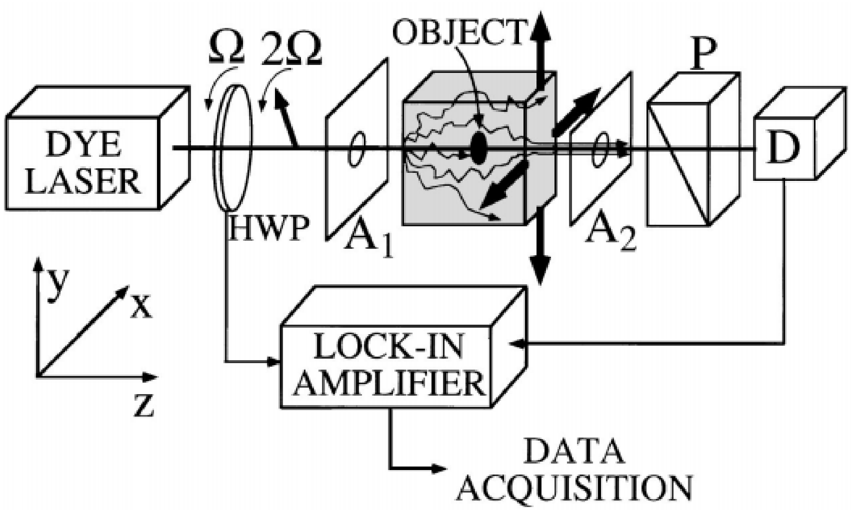

FIGURE 1.1: Emile et al. [10] proposed imaging scheme.

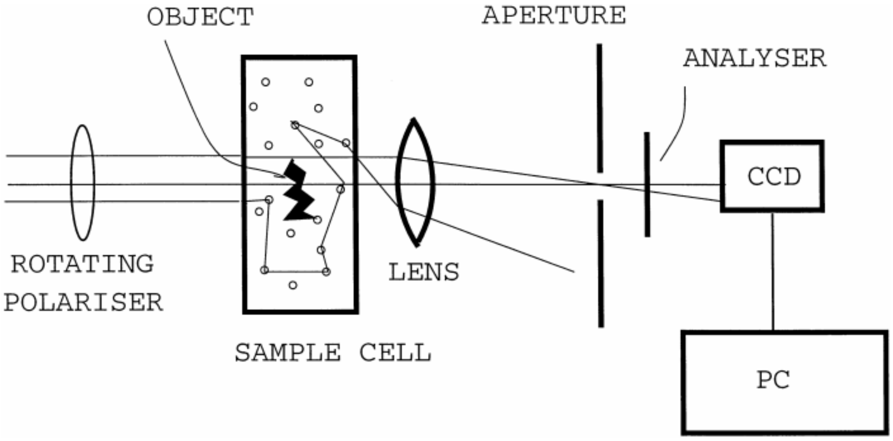

FIGURE 1.2: Ramachandran and Narayanan [6] TMI scheme.

inside. The emergent light is filtered by a lens-aperture system, reducing the diffuse component. The filtered component goes through an analyser and then shines on the CCD camera. If the medium is not diffuse, a variation in the pixel intensity with $\cos^2(\omega)$ is expected. This property is exploited by acquiring pictures with the camera at a given known fixed rate and doing an FFT to the variation of each pixel intensity over time. A temporal frequency bandpass filter is applied, letting only the 2ω component go through (equivalent to $\cos^2(\omega)$), effectively filtering the diffuse component, which is expected to have a random polarization variation.

These techniques unequivocally prove the feasibility of imaging objects enclosed or behind diffuse media, these techniques aren't exactly interesting for the problem of MMFI. Whereas the described techniques work in transmission, in MMFI one seeks to work in reflection instead. Besides, the ballistic/dispersive photons model is not applicable to fibre optics. In optical fibres, modal dispersion is the source for the scrambling of the image information. This is a case where the model for information scrambling on diffuse media can't be used for multimode fibre optics. Nevertheless, the work developed by these authors provides a historic background that shouldn't be disregarded.

1.1.2 Measuring the transmission matrix with interferometric setups

Choi et al. [12] present an alternative way to deal with turbid media imaging. Instead of considering the turbid medium as an obstacle to overcome, they look at it as an information "encoder", aiming their work in finding a way to decode the information. They build upon the idea of the **transmission matrix** (TM). The plane waves from the various object plane points at different angles are chaotically, but *not* randomly[*], scattered through the turbid medium, effectively scrambling all the information, leaving apparent nonsense at the image plane. But scrambled does not mean lost! Characterizing the input-output response of the turbid medium, it can now be treated as just yet another optical element of the system. After this characterization, one now knows how light travels through the complex medium, and it can be used equivalently to a lens. The matrix that defines the input-output response of the system is what one defines as the TM. The idea of **turbid lens imaging** (TLI) is thus born.

According to Choi et al. [12]., a turbid medium can couple optical waves coming from steep angles yielding a high effective numerical aperture (NA). This means that if all the information is recovered from the turbid medium, it should allow images with more resolution than it would be possible simply imaging through a lens with a lower NA. At the same time, light from points away from the axis of the imaging system can also be propagated, effectively widening the field of view (FOV). Figure 1.3 is explicative of this effect: (a) shows conventional lens imaging while (b) demonstrates how waves which would be outside the numerical aperture range in traditional imaging can now reach the camera sensor, increasing the numerical aperture of the system. Finally, (c) shows the widening of the field of view due to the scattering of light in the turbid media. Figure 1.4 shows an object imaged with a high-NA objective lens ($\mathrm{NA} = 1$) where the image of a barcode is clearly resolved. Then, the same barcode is imaged through a lens with $\mathrm{NA} = 0.15$ where the features are not resolved because the smallest features are smaller than the resolution

---

[*] Wave scattering in turbid media is highly chaotic, but not random, in the sense that the same input field will yield the same output field.

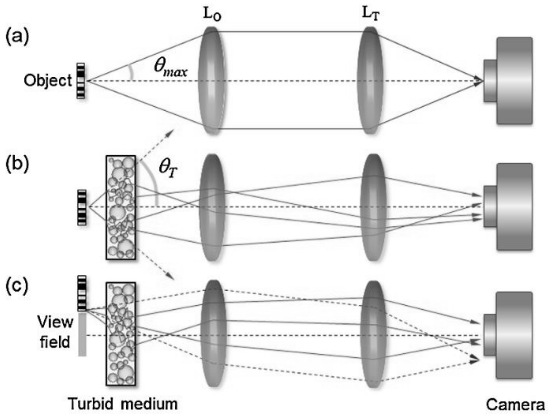

FIGURE 1.3: Figure 1 from [12]. (a): conventional imaging system with lens; (b): increasing of the numerical aperture by the diffuse medium; (c): widening of the FOV via the diffuse medium.

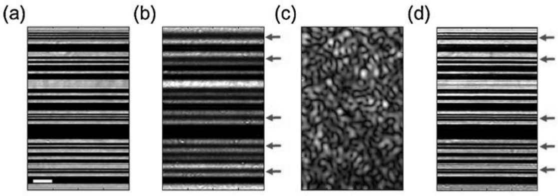

FIGURE 1.4: Figure 3 from [12] (excerpt). (a): object imaged with a high-NA lens (NA = 1); (b): object imaged with a low-NA lens (NA = 0.15); (c) single image as recorded by the camera after inserting the diffuse medium in the optical path; (d) reconstructed image with the diffuse medium in the optical path.

limit of such imaging system. Finally, a layer of ZnO acting as a turbid medium is added between the object and the small numeric aperture lens, yielding a system with equivalent NA = 0.85, resulting in an over 5-fold increase in numeric aperture and consequentially, resolution, allowing again to resolve the smallest object features after reconstruction. In 2012, these authors applied this principle on imaging through multimode fibres, as published in Physical Review Letters [13]. They came up with an in-reflection holographic 3D system, allowing digital refocusing, as whereas TLI systems until then were typically transmission techniques only. Multimode optical fibres are used as illumination device, information propagation device and as a turbid medium. They employed the described TLI scheme to revert the distortion of the light on the object plane to the image plane path, and speckle imaging techniques to revert the distortions from the illumination source to the object plane. Results of this scheme can be seen in figure 1.5. This system's resolution is limited by the NA of the optical fibre and the use of digital holography allows for numeric refocusing. But it has its drawbacks. The fibre cannot move after calibration and should be as straight as possible to avoid higher mode loss on bends. Also, as the calibration is performed in transmission, and acquisition time typically takes a couple of seconds, limited by the sensor array acquisition rate. These are very limiting properties of this imaging system regarding its use as in-vivo endoscope. In 2015 they published a paper first-authored by H. Jang where they use MMFs coated with a turbid material to increase the input NA even further [14].

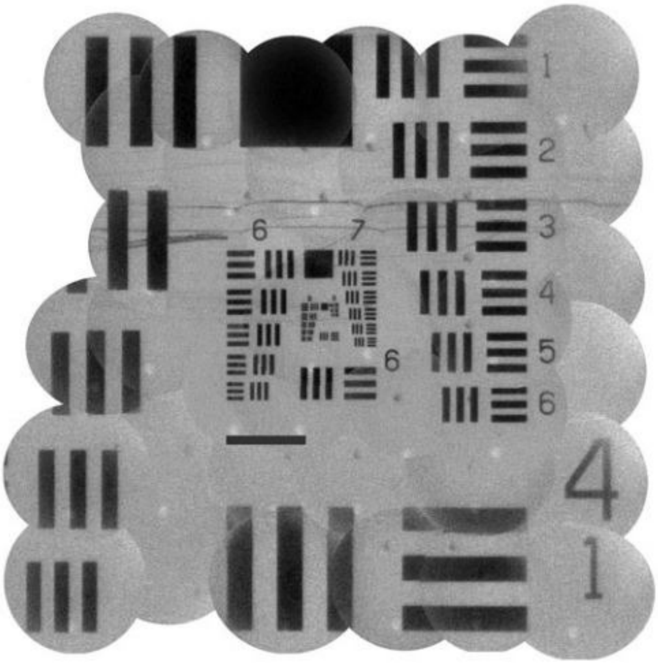

FIGURE 1.5: Figure 2 from [13] (excerpt). Each circle corresponds to one position of the optical fibre relating to the object.

The idea of determining the TM from calibration and then using it to make the diffuse medium a predictable optical component is applied by many other authors. Li and Zhong [15] go for a simple setup with a Mach-Zehnder interferometer and spatial filtering. Others go with more or less intricate setups using optical components, ranging from spatial light modulators (SLMs) [16, 17] to optoacoustic deflectors (OADs) [18, 19]. The approach on building such systems with optical modulators is always alike: build a basis set of optical encoding masks and use that basis to modulate the light entering the diffuse medium and record the output. With the help of off-axis digital holography, one can retrieve the complex-valued TM. Farahi et al. [20] propose a technique using a polymeric film with an encoded hologram over the tip of the multimode fibre. This hologram is phase conjugate of the propagation over the MMF under some conditions, for example, using a straight fibre. A monitoring system, alongside an accompanying algorithm make sure that the light field at the distal tip of the fibre keep phase conjugate with the hologram. This is made using an SLM to compensate for the change in modal dispersion in the fibre due to bending.

Common applications of these techniques where a complex media is characterized by its transmission matrix include light/dark-field microscopy, fluorescent imaging and optical trapping. The applications in biophotonics become very evident as described in the review articles by Kim et al. [21] and Gigan [22].

1.1.3 Measuring the transmission matrix without a reference arm

Interferometric techniques for measuring the TM require reference arms and high optical stability. To try to simplify the optical systems, reference-less methods for calculating the TM were proposed. Popoff et al. [23] published the paper titled *Measuring the Transmission Matrix in Optics: An Approach to the Study and Control of Light Propagation in Disordered Media*. In this work, they present a scheme to measure the transmission matrix without a reference arm. It's worth noting that, although this is still an interferometric method, it is an *in-line* method, meaning that both an optical reference and a modulated region are carried on the same optical channel. The removal of the reference arm massively simplifies the optical system both in component count and alignment. They make use of a spatial light modulator to control the light incident on the diffuse medium for later characterization. The details of how this is made are discussed in section 4, as this is also the basis of the work developed on that chapter. Later, others follow similar paths, either using SLMs or digital micromirror devices (DMDs) for light control. Conkey et al. [24], Caravaca-Aguirre and Piestun [25], Tao et al. [26] use this kind of devices in their works. They use a DMD and Lee holography as the source for the modulated wave basis for TM calibration. The advantage of the DMD is the high-speed capability. Coupled with a high-speed photodetector kilo-Hertz acquisition rates are possible, rather than sub-100Hz typical in LCD SLMs. Dremeau et al. [27] also used a DMD for a reference-less technique, but they rely on binary intensity modulation and phase retrieval algorithms for imaging, rather than phase modulation used by the other authors. N'Gom et al. [28] also develop on this idea, using semi-definite programming algorithms to approach the TM acquisition problem. The knowledge of the TM can either be used for imaging or, most commonly, light manipulation through the diffuse medium, especially in the case of focusing light. Focusing light through diffuse media (or fibre optics) allows for single-pixel imaging schemes, which is a technique particularly simple for fluorescent imaging: once can either focus on multiple locations at the object plane or just move the object with translation stages and then acquire the back-scattered signal using a simple photodetector with the help of a dichroic mirror.

1.1.4 Optimization algorithms

Despite many efforts, acquiring information of the complex-valued transmission matrix of a system is arguably a hard challenge. This pushed many authors to go for optimization based approaches instead. Vellekoop and Mosk [29, 30] built a simple setup where the input wave incident on a scattering sample is controlled by an SLM. An optimization algorithm tries to compute the optimal input wave to produce the desired output, usually a tight focus, for the reasons previously mentioned. Caravaca-Aguirre et al. [31] also explored this technique, once again using a DMD and Lee holography for phase modulation to achieve high-speed optimization. Akbulut et al. [32] also explore the use of DMDs for high-speed optimization but on a direct way, avoiding holographic techniques. Phase modulation approaches try to align all modes propagating to the complex medium in a way that causes maximum constructively interference at the desired spot, whereas the approach by Akbulut takes the simpler idea of just eliminating modes that contribute negatively to the optimization goal. These optimization based approaches were also explored during this work and they are thoroughly explored in chapter 5.

1.1.5 The shower curtain effect: memory effect and phase retrieval

> *An observer standing away from a shower curtain can detect the presence of a person standing just behind it whereas the opposite is not true.*
>
> TREMBLAY ET AL. [33]

More recently, Edrei and Scarcelli [34, 35] proposed a totally novel way to think about turbid media imaging: the shower curtain effect (SCE). Exploiting the so-called memory effect on its far-field version, these authors figured out a scheme to image objects that have diffuse media behind and after them.

Optical memory effect was recently studied in depth by Osnabrugge et al. [36], although it already had provided ground for imaging system through diffuse media by Bertolotti et al. [37]. In essence, angular optical memory effect states that the speckle pattern generated by some beam shining on a diffuse medium is heavily correlated to another beam shining on the same medium but a different angle. In fact, the output speckle rotates by the same amount as the difference between the angle between the input beams. So, if we have an object hidden behind a diffuse medium or in the distal tip of a multicore fibre, we can acquire images for different angles of the incident beam and get enough information to get an estimate of the light field . Now, with the use of the so-called phase retrieval algorithms, it is possible to retrieve the original object information. The advantage of this technique in multicore fibres is that now the maximum resolution is given by the maximum number of independently propagating modes in the multicore fibre which is much greater than the number of cores, assuming they are multimode and/or they have mutual coupling between them. This demonstrates how modern computational power can be of use to improve on existing techniques and turn what was previously considered as a noise inducing phenomena into something exploitable to actually enhance the system capabilities.

Shower curtain effect imaging was also explored in this work, so the thorough explanation of how this system operates can be encountered on chapter 3. Their work is preceded by the work from Bertolotti et al. [37] and later also explored by Yang et al. [38] and where a technique using near-field memory effect is explored. Both techniques depend on phase retrieval algorithms, a subject heavy settled by Fienup [39, 40, 41], and also explored in this work. It's also worth mentioning the work of Amitonova et al. [42] where they explore the rotation memory effect of multimode fibres which opens a new path to explore the pursuit of multimode fibre imaging.

1.1.6 Other approaches to TMI

Stasio et al. [43, 44] developed a scheme for enhanced imaging through multicore fibre optics. Traditionally, the way of using multicore fibres is analogue to how uses fibre bundle endoscopes for imaging. This limits the resolution on one image pixel per core and multicore fibres have cross-talking because of core-to-core coupling, creating a penalty to the SNR. However, multicore fibre optics have the property of optical memory effect.

Singh et al. [45] take the diffuse media imaging problem in a totally different path, developing an holographic technique. This technique consists on illuminating both the object and the diffuser directly with a split laser beam. The interference of these waves generates a hologram of the object right after the diffuser. This hologram is imaged into a camera with a lens. This hologram will be heavily speckled. Overcoming speckle illumination is known in literature [46]. To solve this, the authors rotate the diffuser and acquire several images. The average of the reconstructed holograms yields the object information.

This description of techniques used for complex media imaging and light manipulation is still not exhaustive. The number of authors and variety of techniques tackling this problem shows how important this problem is and how there is still much to do, regarding the search of techniques that suit the most diverse use cases.

1.2 Outline of this work

We have now stated the problem and described some of the techniques used to tackle it. For our work, we wanted to get acquainted with the formulations, techniques, hardware and software involved in tackling the problem of light manipulation through complex media.

For this, we developed three experiments. The first one is a technique of imaging through diffuse media based on the shower curtain effect, reported in chapter 3. The second experiment, described in chapter 4, has to do with the reference-less measurement of the so-called transmission matrix, used to characterize a complex medium. And last, but not least, we experiment with manipulating light through complex media using optimization algorithms, which we report in chapter 5. In each of these chapters, we start with the description of the theory behind both the optical setup and the digital signal processing chain. We then present how we implement this knowledge, describing the optical setup and the code developed. We finish by presenting and discussing out results.

Before all that, besides this introductory chapter, in chapter 2 we take some time to describe some of the tools, both software and hardware, used in these experiments, as they are common to most or all the experiments and have some specifications worth mentioning and discussing.

We finish with an overall conclusion of the work developed, and a roadmap for future developments in this area.

Chapter 2

Getting started: The tools used

During the development of any project, one needs good tools. The work developed features optical systems with digital instrumentation control and data processing. Especially, the latter amounts to a great volume of the work developed. In this chapter, we present the most notable software and hardware tools used, justifying the choice for them, and emphasizing their relevance in the developed work.

2.1 Hardware

The optical assemblies constructed during the development of this work consist of many components: laser, lenses, cube beam-splitters, light modulators, sensors, etc. While the optical systems themselves are described with detail on the appropriate sections, there are key components that are worthy of particular discussion, namely the light modulators and the sensor array (camera).

2.1.1 Spatial light modulators

As described in the introductory chapter, the advent of practical and accessible dynamic light modulation apparatus is of the uttermost relevance for light manipulation and imaging through turbid media. In this work, we used both a Liquid Crystal Display Spatial Light Modulator and a digital micromirror device. While the latter was not used for the final results of this work, the work developed with the device is worthy of mention and its discussion will provide context in discussing future paths of research.

2.1.1.1 LCD SLM: the Holoeye PLUTO-2 family

FIGURE 2.1: Holoeye PLUTO-2 [47].

For spatial light modulation, we opted in for the Holoeye PLUTO-2-VIS-016 LCoS (liquid crystal on silicon) reflective SLM [47]. This SLM was available in-house and provides phase modulation in the 420 – 650nm wavelength range, compatible with our choice for 532nm illumination. It interfaces with the computer via the graphics card, using a DVI link. For the host computer, the SLM is just a secondary display. Each pixel can be addressed with an 8-bit value, corresponding to a grey level on the display (from "black" to "white" so to say). Note that this black-to-white addressing does not translate into amplitude modulation. The amount of phase shift over the light shining on a pixel with a particular grey level depends on configurable parameters, described further down. Another SLM was available in-house, the Holoeye LC-R 2500, but the PLUTO-2-VIS-016 proved to be a better option. The reasons why will become evident in this text.

The PLUTO-2 family is a newer generation than the LC-R 2500. The LC-R 2500 modulates light both in amplitude and phase not independently and requires careful control of the input and output polarizations of light to achieve phase-only modulation, whereas the PLUTO-2 family only requires the input polarization to be aligned with the wider axis of the display to achieve phase-only modulation. The PLUTO-2 manual recommends normal incidence. This means that a cube beam splitter (BS) should be used in conjunction with the device, as described in figure 2.2. If we consider a loss-less 50/50 cube BS only 25% of the light shining on the device actually comes out as usable light, representing an insertion loss of 6dB without considering the losses by diffraction on the SLM, as its pixel structure unavoidably generates diffraction gratings. This proved to not be a problem due to the generous power budget form the laser used, which had to be attenuated in many situations anyway, and the high sensitivity of the detector array.

But the greatest advantage of the PLUTO-2-VIS-016 was yet to be mentioned: the VIS-016 model is a "high retardation version". SLMs are generally plagued with phase flicker. This means that for a constant displayed grey level that would, in theory, correspond

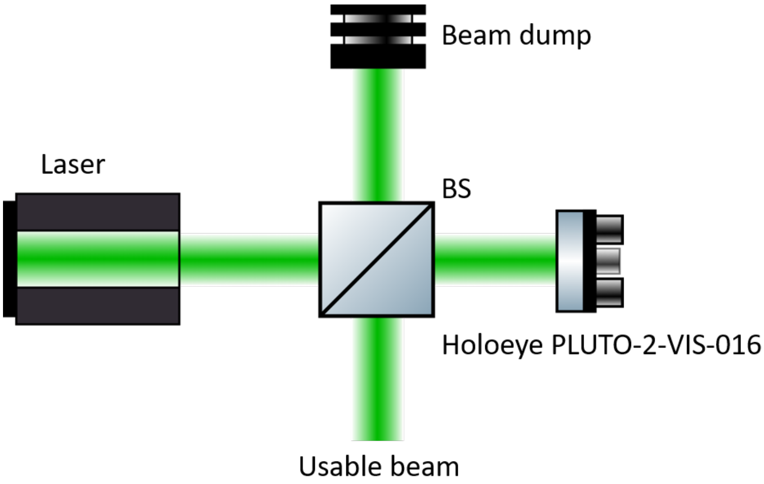

FIGURE 2.2: Correct way to setup the Holoeye PLUTO-2 SLM. Beam expansion apparatus is not shown.

to some phase modulation, the modulation phase actually flickers between two values centred around the desired value. This is totally undesirable for the proposed use-case. Fortunately, the PLUTO-2-VIS-016 can be configured in a way that the electrical control of the liquid crystals (LCs) provides high phase stability, trading off speed performance. Furthermore, the LC-R 2500 require manual calibration by the user: for each particular combination of wavelength, angle of incidence, and input/output polarizations, the grey-level to phase curve is different and requires characterization. The VIS-016 model provides user-configurable gamma curves that guarantee linear modulation for a particular range, assuming the user is using the recommended polarization and incidence angle. We opted for high-stability LC addressing with $[0, 2\pi]$ modulation for the $[0, 255]$ (8-bit) range of values assignable to pixels. This means that any phase to grey-level conversion can be trivially made: $P_v = \theta \times 255/2\pi$ where P_v is the pixel value, rounded to the nearest integer and θ is the desired phase modulation. The resolution of the device is 1920×1080 pixels with a pixel pitch of 8.0μm.

2.1.1.2 DMD: Vialux DLP V-7000

Digital micromirror devices have a totally different working principle than LCD SLMs. They fall under the category of micro-opto-electromechanical system (MOEMS), so they are actually a system with moving parts. Each pixel is actually a (micro)mirror on a binary positioner: each pixel can be either on (the positioner points the mirror in a way it reflects light to the output) or off (the positioner makes the mirror point light elsewhere). So these devices are binary amplitude modulators, not phase modulators, although with the clever use of Lee holography one can actually make a DMD become an arbitrary phase-only modulator, which is described further down this section.

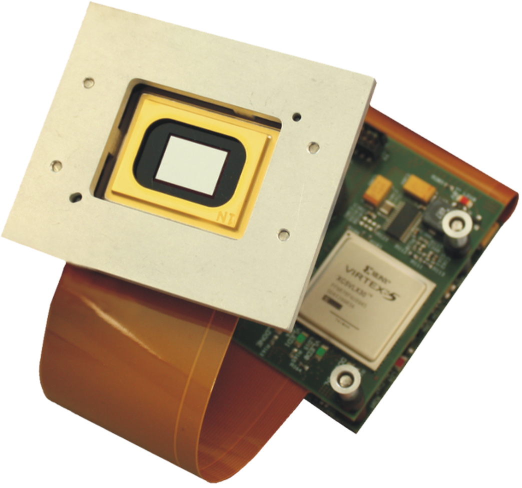

FIGURE 2.3: Vialux DLP V-7000 DMD [48].

The DMD used was a Vialux DLP V-7000. It uses the Discovery$^{\text{TM}}$ 4100 DLP chip [48]. The resolution is 1024 × 768 pixels with a pixel pitch of 13.7μm. Contrary to the Holoeye PLUTO-2, the interface with the DMD is USB. This means the desired display pattern(s) is(are) uploaded and then displayed. The controller board has SO-DIMM RAM onboard and two FPGAs for control. The controller board offers a header with trigger input/output pins for synchronization. The trigger input can, for example, trigger the next frame stored in memory. This FPGA+RAM approach has a clear advantage: while the SLM can only change frames at typical display refresh rates (60Hz), the DLM 4100 can change frames at the rate of 22.727 kHz (over a 370 fold increase in display rate). Furthermore, the PLUTO-2-VIS-016 in the most phase stable configuration actually takes a considerable amount of time to change the displayed frame: pixel reconfiguration is actually observable with the naked eye. The SLM effective usable frame-rate is between 5 to 10Hz, while with the DMD the bottleneck becomes the detection apparatus. In the other hand, an obvious disadvantage arises: on optimization algorithms where the next frame must be calculated every iteration it's not efficient to upload and display the frame every time. This will actually tremendously reduce the effective frame rate to about the one of the SLM or lower. Caravaca-Aguirre et al. [31] actually tackles this problem actually programming the DMD's FPGA with an optimization algorithm directly, interfacing the DMD control board with an analogue-to-digital converter (ADC) connected to a high-speed detector. While this is a clever solution, FPGA programming requires speciality knowledge about hardware description languages, like Verilog, and it's very time consuming, so this kind of approach was not tackled in this work, but it's left as an open end to follow on future work developed in this area.

And what about the phase-only modulation using the DMD?

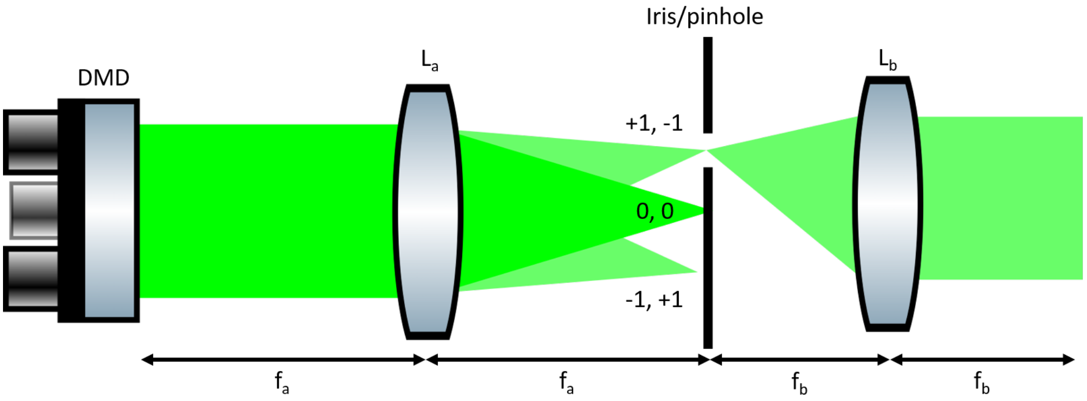

FIGURE 2.4: Scheme for achieving phase only modulation with a DMD using Lee holography [50].

For that, as hinted, Lee Holography is the answer [49]. Sébastien Popoff [50] describes this process in short: Let $\Phi(x, y)$ be the desired phase modulation. We generate the following amplitude pattern:

$$f(x,y) = \frac{1}{2}\left[1 + \cos(2\pi(x-y)\nu_0 - \Phi(x,y)\right] \tag{2.1}$$

Equivalently, one can write:

$$f(x,y) = \Re\left\{\frac{1}{2} + \frac{1}{4}e^{+i2\pi(x-y)\nu_0}e^{-i\Phi(x,y)} + \frac{1}{4}e^{-i2\pi(x-y)\nu_0}e^{+i\Phi(x,y)}\right\} \tag{2.2}$$

Interpreting this equation carefully, if ν_0 is greater than the highest spatial frequency of $\Phi(x, y)$ what we actually have is $\Phi(x, y)$ on a spatial carrier frequency, $(\nu_x = \nu_0,\ \nu_y = -\nu_0)$ or $(\nu_x = -\nu_0,\ \nu_y = \nu_0)$. This means that by using a 4-f system with an iris filtering for the (1, -1) or the (-1, 1) diffraction orders, we have the desired phase modulation. This is represented on figure 2.4. The obvious disadvantage to this system is the losses by diffraction efficiency. Even in theory, only one-fourth of the power is actually carried to the diffraction orders of interest. To make things worse, the pixel nature of the DMD generates its own diffraction, making the ratio between output and input power even lower.

But this discussion isn't over yet. Once again, the amplitude modulation offered by the DMD is only binary. This is incompatible with $f(x, y)$. The solution is actually to binarize it, generating what is effectively a diffraction grating structure:

$$g(x,y) = \begin{cases} 1 & \text{if } f(x,y) \geq 0.5 \\ 0 & \text{otherwise} \end{cases} \tag{2.3}$$

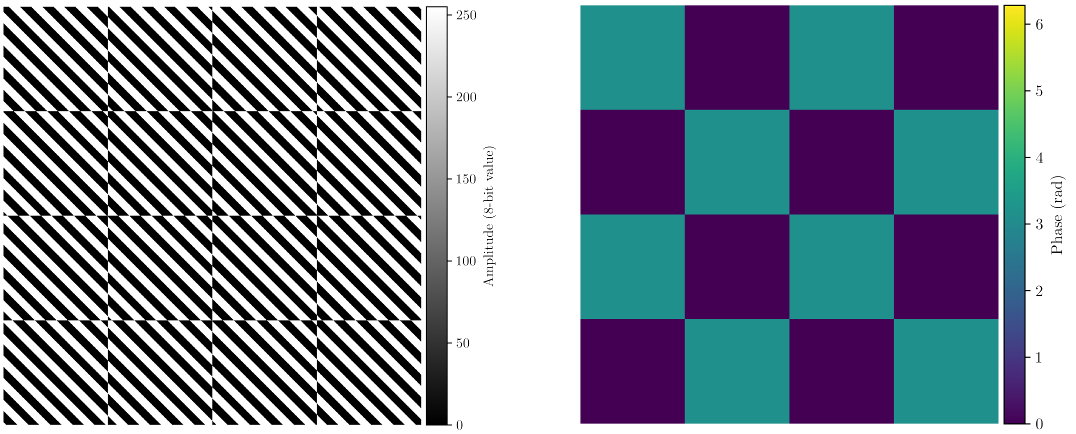

(A) Gratting pattern displayed at the DMD. (B) Resulting phase mask.

FIGURE 2.5: Relation between the pattern displayed at the DMD and the corresponding resulting phase mask after the Lee holography scheme. Note that the period of the grating is generously enlarged for display purposes. In a practical scenario, the number of periods per macro-pixel would be greater.

This solution does not come without trade-offs. This binarization has the drawback of partially blurring the phase modulation, due to the approximation of a sin-wave with a square wave. For a correct approximation of the target phase modulation, ν_0 has to be at least greater than the greatest frequency of $\Phi(x, y)$ but it must be kept under a value that guarantees good resolution on the binarization of $f(x, y)$, meaning that the "black" and "white"* stripes must be distinguishable. At the same time, each (macro)pixel one wants to modulate phase on must have a large enough number of grating periods on it. This limits how many independent phase macropixels one can have, limiting the resolution of the system. Careful tuning of ν_0 is essential. Figure 2.5 shows the relation between the pattern displayed at the DMD and the resulting phase modulation when using the Lee holography scheme.

2.1.2 Detector array: Ximea CMOS cameras

Another key element of the puzzle is the optical detection system. We opted for a CMOS camera, the Ximea MQ013MG-ON, from the XiQ family [51]. The sensor is an Onsemi PYTHON 1300 with a resolution of 1280 × 1024 pixels with a pixel size of 4.8μm. It features 56dB of dynamic range and it can work either on 8 or 10 bits per pixel modes. The main advantages of this device are the maximum achievable frame rates: up to 210 frames per second at full resolution and over 1000 fps at a 640 × 400 resolution,

---

*meaning pixels turned off and on, respectively via region of interest (RoI). Other great feature in the interface: a single USB 3.0 cable. This saves up on cost, compared to devices that require dedicated frame-grabbers. It also has a socket for trigger I/O. Ximea also has an official API [52] for the Python programming language and LabVIEW, which add value to the device considering the typical software solutions used at CAP. For practical purposes, mainly to reduce file sizes, the camera was used on downsampling mode, yielding an effective resolution of 640 × 512 and at 8 bit per pixel mode.

FIGURE 2.6: Ximea XiQ MQ013MG-ON [51].

2.2 Software: the Python programming language

> *Python is a truly wonderful language. When somebody comes up with a good idea it takes about 1 minute and five lines to program something that almost does what you want. Then it takes only an hour to extend the script to 300 lines, after which it still does almost what you want.*
>
> DR. JACK JANSEN, MAINTAINER OF MACPYTHON

So, until now, we discussed the hardware used. But hardware alone does not do much. As mentioned in the introduction to this work, algorithmics is key for TMI, so a conscious choice of framework is absolutely important. As the title of this section unveiled, the language chosen was the Python programming language. For simplicity, the Anaconda distribution, from the Anaconda organization [54] was used. This distribution features the Python 3.x core plus all the libraries typically needed for scientific use.

FIGURE 2.7: The Python$^{\text{TM}}$ foundation logo [53].

While this brief introduction to why Python was deemed an adequate fit to the work to be developed does not aim to describe in depth how the Python stack for scientific development works, it is still worth justifying the decision to go for it. Lets then present the reasons motivating the choice for this development setup:

- **Previous know-how** on the language: learning the Python programming language is part of the curriculum for the integrated MSc in engineering physics at FCUP. More so, the language and its scientific modules were often used in classes relating to computational physics, consolidating the know-how.

- Fast, very complete, **scientific libraries**: Python has a well established base of libraries for scientific programming, like the *numpy* and *scipy* packages [55]. These, with the addition of the *matplotlib* data visualization package [56] make for what is said by many to be a functional replacement to commercial solutions like MatLab [57].

- The Jupyter **Notebook**. Programming in notebooks rather than script files is a paradigm well established on Wolfram's Mathematica. The project Jupyter for Python [58] aims to bring the functionality of the notebook paradigm into the Python ecosystem. This revealed extremely helpful in optimizing the workflow. Rather than having to re-run scripts, with sometimes considerable amounts of run-time, one can divide the code by blocks (called cells) and only run cells individually. This means that data acquisition and visualization on the same programming file becomes very easy, especially with the now established integration between *matplotlib* and Jupyter. This means that one can acquire data and/or change visualization parameters on the fly without the need to re-run the often lengthy acquisition process, or without having to write it to a file and load it again by a visualization script.

- **Third-party libraries**: As a wide-spread and popular programming language, Python sees a lot of support of random contributors. Ximea, as mentioned, provides an official API to use on Python, so we had an easy way to interface out camera system into our software implementations. For the SLM and the DMD, Popoff [59] provides open source libraries to interface with these devices.

Chapter 3

Shower Curtain Effect Imaging

The first technique for imaging through diffuse media experimented with during this project was the so-called Shower Curtain Effect (SCE) Imaging. As described in the introductory chapter of this work, SCE was pioneered by the work of Edrei and Scarcelli [34]. It's a technique that does not require special optical devices other than a camera for acquisition, and it does not require that the diffuse media is stable, as most of other techniques do. The only requirement for the diffuse media is the distance to the object: the light should propagate in a transparent media a distance large enough so that the far field approximation becomes a good approximation to the electromagnetic field. This might seem very limiting at first since the typical scale of far field distances at the optical range is several meters. However, as we shall see, using speckle illumination techniques, we can dramatically drop this condition into the few centimetres range.

This technique is heavily dependent on digital signal processing. In particular, we shall discuss phase retrieval algorithms: what do they do, how they work and how do they serve a purpose on this technique. Let us then begin with an overview of the theory behind the technique, then follow to a discussion of the practical implementation. After that, we shall discuss the digital processing chain, where we will detail phase retrieval algorithms. We then shall end this chapter with our results and discussion.

3.1 SCE Imaging: how does it work?

Let's consider an object placed between two diffuse media: one of them is on the side of an incoming coherent illumination source, and the other one is placed on the detection side (outgoing from the object), between the object and the camera. Light from the

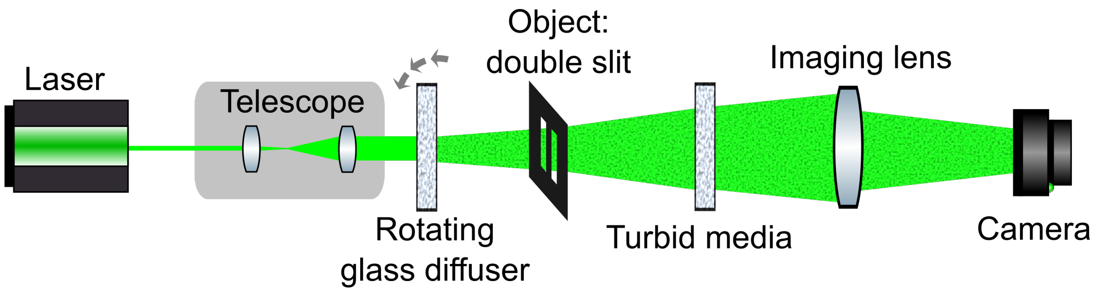

FIGURE 3.1: Setup for SCE imaging. Refer to section 3.2 for detailed description of the components.

coherent source get dispersed by the first diffuser, forming a speckle patterns due to the interference from the scattered waves. This diffuser serves two purposes: on one hand, it simulates what would happen on an in-reflection technique where the illumination light would be scattered by the diffuse reflector; on the other hand, it generates speckle illumination patterns which are necessary for the shortening of the far-field condition. Figure 3.1 provides an illustration of this scheme.

We split the problem in two: the problem of the object being illuminated with a speckle pattern, rather than uniform light and the problem of the information coming out from the object being blurred by the diffuse media. Blurring from the second diffuser is tackled using the far-field shower curtain effect. This effect unlocks a way to make an intensity pattern be retrievable after passing through a thin diffuse media or diffuse reflective surface. For the problem of speckle illumination, we resorted to de-speckle techniques based on averaging multiple speckle illuminations. To retrieve the object itself, we looked into exploiting the relation between far-field diffraction from an object and its autocorrelation. This autocorrelation is undone resorting to phase retrieval algorithms.

3.1.1 Overcoming blurriness from diffuse media

Let's start by analysing the problem of light coming out from the object being scrambled by the diffuser placed before the imaging system. Let's keep in mind the object is illuminated by a speckle pattern, and call $f_n(x,y)$ to the light field coming out of the object, be it by reflection or transmission. A property of speckle is its partial coherence, so $f_n(x,y)$ is actually composed by a coherent component and an incoherent one. Propagating this field to the far-field, we can distinguish two components: the coherent term, which will have a field intensity approximated by its Fourier transform, $|\mathcal{F}\left[f_n(x,y)\right]|^2$, plus the incoherent term. The incoherent term can be regarded as just noise into our system and we can deal with it later. Focusing on the coherent term, we will make use of the Wiener–Khinchin theorem, which is a particular case of the more general cross-correlation theorem.

The cross-correlation theorem states that:

$$f(t) \star g(t) = \mathcal{F}\left[\bar{F}(\nu)G(\nu)\right] \tag{3.1}$$

where $\star$ denotes the correlation operation, $\bar{F}$ means the complex conjugate of F, and $F(\nu)$ and $G(\nu)$ are the Fourier transforms of $f(t)$ and $g(t)$ respectively. The proof to this theorem is trivial and can be expressed in few lines [60]:

$$\begin{aligned} f(t) \star g(t) &= \int_{-\infty}^{+\infty} \bar{f}(\tau) g(t+\tau) d\tau \\ &= \int_{-\infty}^{+\infty} \left[\int_{-\infty}^{+\infty} \bar{F}(\nu) e^{2\pi i \nu \tau} d\nu \int_{-\infty}^{+\infty} G(\nu') e^{-2\pi i \nu'(t+\tau)} d\nu' \right] d\tau \\ &= \int_{-\infty}^{+\infty} \int_{-\infty}^{+\infty} \int_{-\infty}^{+\infty} \bar{F}(\nu) G(\nu') e^{-2\pi i \tau(\nu'-\nu)} e^{-2\pi i \nu' t} d\tau d\nu d\nu' \\ &= \int_{-\infty}^{+\infty} \int_{-\infty}^{+\infty} \bar{F}(\nu) G(\nu') e^{-2\pi i \nu' t} \left[\int_{-\infty}^{+\infty} e^{-2\pi i \tau(\nu'-\nu)} d\tau \right] d\nu d\nu' \\ &= \int_{-\infty}^{+\infty} \int_{-\infty}^{+\infty} \bar{F}(\nu) G(\nu') e^{-2\pi i \nu' t} \delta(\nu'-\nu) d\nu d\nu' \\ &= \int_{-\infty}^{+\infty} \bar{F}(\nu) G(\nu) e^{-2\pi i \nu t} d\nu \\ &= \mathcal{F}\left[\bar{F}(\nu)G(\nu)\right] \end{aligned} \tag{3.2}$$

The proof uses the definition of the Fourier transform and properties of integrals: manipulating the order of integration one can reach the result being proven. The Wiener–Khinchin theorem is the particular case for when $f(t) = g(t)$, meaning that [61]:

$$C_f(t) = f(t) \star f(t) = \mathcal{F}\left[|F(\nu)|^2\right](t) \tag{3.3}$$

If we look into equation 3.3 we recognize that $|F(\nu)|^2$ is exactly the coherent term obtained by the far field propagation of the speckled object field, $f_n(x,y)$. So, with a simple Fourier transform we can obtain the autocorrelation of the speckled object information:

$$f_n(x,y) \star f_n(x,y) = \mathcal{F}\left[\left|\mathcal{F}\left[f_n(x,y)\right]\right|^2\right] \tag{3.4}$$

The next step is to retrieve object information from its autocorrelation. For that we use phase retrieval algorithms. The name phase retrieval algorithm comes from the fact that the object field and its autocorrelation share the same amplitude of their Fourier components, differing only on their phase components making it is necessary to figure out the correct phases that generate the object field instead of the autocorrelation. This will be discussed later, in an appropriate section.

The Shower Curtain Effect comes in at this point. We use this effect to overcome the second diffuser, between the object and the camera system. We can model the shower curtain effect as a low pass filter with a cut-off dependant on the distance to the curtain itself [62, 63]. This is actually a good model for the apparent paradox of the "one observer can see someone behind the curtain but not the opposite" as the quote by Tremblay et al. [33] on the introductory chapter of this work. And how does this help us? Since we put the diffuse media at a distance that complies with the far field condition, what we want to image, which is the intensity field of light, is being projected on one of the surfaces of the diffuse media. If we image the other surface into our camera, we're actually the observer watching an "object"* right behind the shower curtain! This means minimal cut-off on the "filter" produced by the diffuse media, providing us with enough information for attempting to reconstruct the object with a phase retrieval algorithm.

3.1.1.1 Far-field conditions for partially coherent light

So far, we've mentioned that the far-field condition is achieved in far shorter distances than what is usually considered when using perfectly coherent light. Edrei and Scarcelli [35] discuss this issue, using the formalism from Goodman [64, chapter 5]. First, we remember the far field condition for perfectly coherent illumination:

$$z > 2\frac{D^2}{\lambda} \tag{3.5}$$

where D is the size of the object. Let's now consider partially coherent light coming from an aperture placed on the object plane. The object plane spacial coordinates will be denoted as (ξ, η). The field intensity at some place a distance z away from the source aperture is given by a Fresnel integral:

$$I(x,y) \approx \frac{1}{(\lambda z)^2} \iint\limits_{-\infty}^{+\infty} \iint\limits_{-\infty}^{+\infty} \boldsymbol{J}_t\left(\xi_1, \eta_1, \xi_2, \eta_2\right) e^{-i2\pi/\lambda(r_2'-r_1')} d\xi_1 d\eta_1 d\xi_2 d\eta_2 \tag{3.6}$$

---

*Here the "object" is the far-field intensity pattern.

where $\boldsymbol{J}_t$ is the mutually transmitted intensity function r'_1 and r'_2 are the distances between the points in the aperture plane and the observation plane. The mutually transmitted intensity function is defined as [65, chapter 3]:

$$\boldsymbol{J}_t\left(\xi_1, \eta_1, \xi_2, \eta_2\right) = \left\langle U^*\left(\xi_1, \eta_1\right) U\left(\xi_2, \eta_2\right)\right\rangle \tag{3.7}$$

where $U\left(\xi, \eta\right)$ is the complex amplitude of the optical field at $\left(\xi, \eta\right)$ and $\langle\cdot\rangle$ denotes a time average. This function can also be written using what is defined as the complex coherence factor, $\mu\left(\Delta\xi, \Delta\eta\right)$:

$$\boldsymbol{J}_t\left(\xi_1, \eta_1, \xi_2, \eta_2\right) = \mu\left(\Delta\xi, \Delta\eta\right)\sqrt{I\left(\xi_1, \eta_1\right)}\sqrt{I\left(\xi_2, \eta_2\right)} \tag{3.8}$$

Furthermore, we can use the low angle of diffraction approximation on $r'_2 - r'_1$:

$$r'_2 - r'_1 \approx \frac{1}{2z}\left[\left(\xi_2^2 + \eta_2^2\right) - \left(\xi_1^2 + \eta_1^2\right) - 2\left(x\Delta\xi + y\Delta\eta\right)\right] \tag{3.9}$$

which simplifies to:

$$r'_2 - r'_1 \approx \frac{1}{z}\left[\Delta\xi\left(\underline{\xi} - x\right) + \Delta\eta\left(\underline{\eta} - y\right)\right] \tag{3.10}$$

where $\underline{\xi} = \frac{\xi_1+\xi_2}{2}$ and $\underline{\eta} = \frac{\eta_1+\eta_2}{2}$. We can then compute the light intensity at the observation plane as:

$$I(x,y) \approx \frac{1}{(\lambda z)^2}\iint\limits_{-\infty}^{+\infty}\iint\limits_{-\infty}^{+\infty}\boldsymbol{J}_t\left(\xi_1, \eta_1, \xi_2, \eta_2\right)e^{-i2\pi/(\lambda z)\left[\Delta\xi\left(\underline{\xi}-x\right)+\Delta\eta\left(\underline{\eta}-y\right)\right]}d\xi_1 d\eta_1 d\xi_2 d\eta_2 \tag{3.11}$$

The far-field conditions means that the integral in equation 3.11 can be approximated by a Fourier transform. On a naive look at the equation, it would seem that this condition would be given by: $z \gg \left(\underline{\xi}\Delta\xi + \underline{\eta}\Delta\eta\right)/\lambda$. However, we should inspect what happens to $\boldsymbol{J}_t$. This function is proportional to the complex coherence factor, $\mu\left(\Delta\xi, \Delta\eta\right)$, which is zero outside the coherent area of the illumination beam. This means that $\underline{\xi}$ and $\underline{\eta}$ are bounded by $D/2$. At the same time, $\mu\left(\Delta\xi, \Delta\eta\right)$ looses significance when either $\Delta\xi$ or $\Delta\eta$ becomes greater than half the correlation radius, R_c of the speckle pattern. This reduces the far field condition to:

$$z \gg \frac{DR_c}{4\lambda} \tag{3.12}$$

While we don't present a model for R_c nor did we measure it experimentally, we verified this condition by the working conditions of the SCE experiment.

3.1.2 Despeckling the object field

So far, we managed to get the autocorrelation of the speckled object, as per equation 3.4. This is not exactly what we want to feed into our phase retrieval algorithm: we want, as closely as possible, to get the autocorrelation of the clean object field. This is where speckle imaging techniques come into play: we record multiple images where, in each one, the object was illuminated with a different speckle pattern. In our case, the different speckle patterns are obtained by rotating the first diffuser during acquisition.

Let us model our object as a binary function, $O(x, y)$, valued 1 within the object and 0 otherwise. The speckled image is modelled as this function $O(x, y)$ convoluted with a point spread function (PSF), $S_n(x, y)$ specific for each speckle illumination. This means:

$$f_n(x, y) = O(x, y) * S_n(x, y) \tag{3.13}$$

Summing over N different images with independent speckle illuminations:

$$\sum_{n=1}^{N} |f_n(x, y) \star f_n(x, y)|^2 \propto |O(x, y)|^2 \star |O(x, y)|^2 * \sum_{n=1}^{N} |S_n(x, y) \star S_n(x, y)|^2 \tag{3.14}$$

We can see already the object autocorrelation convoluted with the sum of the autocorrelation of the speckle patterns' point spread functions*. Let us take a close look to this sum: speckle patterns obtained from strong scattering have no spatial correlations. This means that each element of this sum is essentially a high peak at the origin, so the sum will tend to Dirac's delta function as N is large enough. As the Dirac's delta function is the neutral element of the convolution function, we are left with the desired autocorrelation of the object.

At the same time, this need of acquiring a considerable number of samples helps with the aforementioned incoherent noise generated by the first diffuser. We start by getting an average of all camera frames. As the speckle patterns come from a coherent process, and they are uncorrelated between them we expect that, for a large number of frames, we are left with an uniform illumination as, in average, each pixel will be black or white in half of the frames. So the average of all frames will essentially carry information about the incoherent illumination. We take this average frame and subtract it to all acquired frames before further processing.

---

*As we defined the object field as a binary mask, the modulus square makes no difference

3.1.3 Phase retrieval

Up to this point, we have managed to obtain a clean object autocorrelation, $|O(x,y)|^2 \star |O(x,y)|^2$, from which we want to retrieve object information from. Here, phase retrieval algorithms come into play, in order to retrieve complex information from intensity measurements and information that might exist a priori.

As mentioned in the introductory chapter, the phase retrieval problem is studied in depth by Fienup [39]. This article mentions a typical problem in crystallography: one wishes to recover some function of space (the *object*), $f(x)$, given a measurement of the amplitude of its Fourier transform, $|F(\nu)|$ with the constraint that $f(x)$ is both real and positive. This is, in fact, the same problem as in here: we have access to the modulus of the FT of our object via the autocorrelation, and we know that an image of an object should, in fact, be real and positive.

> But how do we use this information to try to retrieve information about the object?

For our work, we used two of the phase retrieval algorithms presented by Fienup [39]: the error-reduction Algorithm, and its variation, the Gerchberg-Saxton algorithm, and the hybrid input-output algorithm. These are amongst the most successful approaches to the phase retrieving problem and they consist on transforming back and forth between the Fourier domain and the object domain, and imposing our constraints in each domain, iteratively. How they differ is on how exactly these conditions are imposed.

While we won't present the proof of convergence, they are convergent, but not necessarily to the intended solution: the autocorrelation is a lossy operation, even from a purely mathematical sense. For example, it doesn't keep information about the position of the object in the plane, so the reconstruction can actually place it anywhere. Adding to that, there is not a really good guess for the starting conditions for the algorithms: in our case, the starting guess is just a random pattern. This means that, while the algorithm is deterministic, the random initial conditions make the output rather unpredictable. In an extreme scenario, the autocorrelation is an actual solution to the phase problem, so the algorithm might converge back to the autocorrelation instead of into the object itself.

These algorithms can be executed for either a number N of iterations, or until a figure of merit, called the error function, is under a defined threshold. This error function will be present next, while describing the algorithms in particular.

With no loss of generality, we now present the phase retrieval algorithms for the one-dimensional case. Changing to the two-dimensional case is trivial, as it only requires applying the described transformations on all axis. The nomenclature used is the one by Fienup [39].

3.1.3.1 Gerchberg-Saxton/Error-Reduction Algorithm

This phase retrieval algorithm consists of 4 steps. Let us assume we have some estimate, $g_k(x)$, of the object field, $f(x)$. For any iteration, k, of the algorithm, this $g_k(x)$ will result from the previous iteration. At iteration zero we generate a random pattern as first guess. Additionally, remember we have the modulus of the Fourier transform of the object field, acquired from the measured autocorrelation. So, at any iteration, k, we follow these steps:

1. Fourier transform $g_k(x)$, resulting in $G_k(\nu) = |G_k| \, e^{i\Phi_k}$;
2. Replace $|G_k|$ with the measured $|F(\nu)|$, resulting in $G'_k(\nu) = |F| \, e^{i\Phi_k}$, which is the estimate of the FT of the object;
3. Calculate the inverse FT of $G'_k(\nu)$, generating $g'_k(x)$;
4. Now, impose the object domain constraints:
    (a) In case of a problem where an object domain intensity measurement is available, $|f(x)|$, make $g_{k+1}(x) = |f| \, e^{i\phi_k}$.
    (b) In case of a problem where no object domain measurement is available, which is our case, modify $g'_k(x)$ the least amount possible to satisfy the constraints knows a priori. In our case, this means forcing it to be real and positive, so we apply the transformation:

$$g_{k+1}(x) = \begin{cases} g'_k(x) & x \notin \gamma \\ 0 & x \in \gamma \end{cases} \tag{3.15}$$

where γ is the set of points where $g'_k(x)$ violates the object domain constraints.

The Gerchberg-Saxton and the error-reduction algorithms differ on the use of option 4a or 4b, respectively.

The convergence of the algorithm can be monitored resorting to this error function:

$$E^2_{\mathcal{F},k} = \frac{1}{N^2} \sum_{\nu} \left| |G_k(\nu)| - |G'_k(\nu)| \right|^2 \tag{3.16}$$

For this family of algorithms, this is equivalent to:

$$E_{\mathcal{F},k}^2 = \frac{1}{N^2}\sum_{\nu} \left| |G_k(\nu)| - |F(\nu)| \right|^2 \tag{3.17}$$

The subscript $\mathcal{F}$ means that this is the Fourier domain error. We can also compute the object-domain error function:

$$E_{\mathcal{O},k}^2 = \sum_{x} \left| g_{k+1}(x) - g'_k(x) \right|^2 \tag{3.18}$$

For the Gerchberg-Saxton algorithm, this is the same as:

$$E_{\mathcal{O},k}^2 = \sum_{x} \left| |f(x)| - |g'_k(x)| \right|^2 \tag{3.19}$$

And for the error-reduction:

$$E_{\mathcal{O},k}^2 = \sum_{x\in\delta} \left[g'_k(x) \right]^2 \tag{3.20}$$

3.1.3.2 Hybrid input-output algorithm

For the input-output algorithm we drop the requirement that $g_k(x)$ is the best estimate so far of $f(x)$. This means that $g_k(x)$ no longer has to obey object domain constraints, allowing for a great deal of flexibility. This algorithm is specifically for situations where only the Fourier domain measurement is available. The algorithm can then be translated into the following steps:

1. Fourier transform $g_k(x)$ resulting in $G_k(\nu) = |G_k|\, e^{i\Phi_k}$;
2. Replace $|G_k|$ with the measured $|F(\nu)|$, resulting in $G'_k(\nu) = |F|\, e^{i\Phi_k}$;
3. Calculate the inverse FT of $G'_k(\nu)$, generating $g'_k(x)$;
4. Transform $g_k(x)$ as:

$$g_{k+1}(x) = \begin{cases} g'_k(x) & x \notin \gamma \\ g_k(x) - \beta g'_k(x) & x \in \gamma \end{cases} \tag{3.21}$$

   where, again, γ is the set of points where $g'_k(x)$ violates the object domain constraints, and β is a real, positive number and a parameter of the algorithm.

For the input-output algorithm, since neither $g_k(x)$ nor $G'_k(\nu)$ are estimates of the object or its FT, equation 3.20 provides the only meaningful metric for the error. Note that if some point of $g_k(x)$ is negative, it is not eliminated right away but rather grows ever larger on each iteration. This would happen until no more negative points exist. The parameter β must be chosen with care: a value too high and the algorithm is unstable; a value too low and the algorithm is slow. In our implementation this parameter is actually not constant, starting from larger values and decreasing towards the end of the process to provide finer iteration steps.

3.2 Our implementation of SCE imaging

The optical setup for our attempt at shower curtain effect imaging has already been pictured on figure 3.1. The hardware used includes a 532nm laser from SUWTECH LASER, a PASCO scientific OS-8523/9 double slit (0.04mm opening, 0.25mm pitch) and the Ximea MQ003MG-CM camera (described on chapter 2). The laser is expanded with a microscope objective (20x, NA $= 0.4$), pinhole (5 μm), plus a bi-convex lens (10cm focal length) system providing a Gaussian beam with a waist of about 25mm. The diffusers are both round glass diffusers from Thorlabs, 1200 GRIT for the first diffuser and 300 GRIT for the second. The first diffuser is mounted on a rotating mount (Thorlabs PRM1/M) and is manually rotated during acquisition. The imaging lens (Leica) images the right surface of the diffuser into the camera sensor. Because of the available laser power, a neutral density filter (not shown) was used to regulate the power. Camera exposure time was around 2ms.

3.2.1 The code

The code is divided into 3 different scripts, written as Jupyter notebooks. The first one is responsible for acquisition alone, the second does all the processing needed before phase retrieval and the last one does the phase retrieving itself.

3.2.1.1 Acquisition process

The acquisition process is straight-forward. The script takes an user-configurable number, N, of camera shots while the user rotates the first diffuser. The other configurable parameters are camera exposure and gain. The gain is usually set at 0dB due to the generous power budget from the laser. The low values of exposure used, of about 2ms, allow for the camera to run at its maximum frame-rate, limited by the bandwidth of the USB bus. During this experiment no camera downsampling was used, this is about 125fps. The

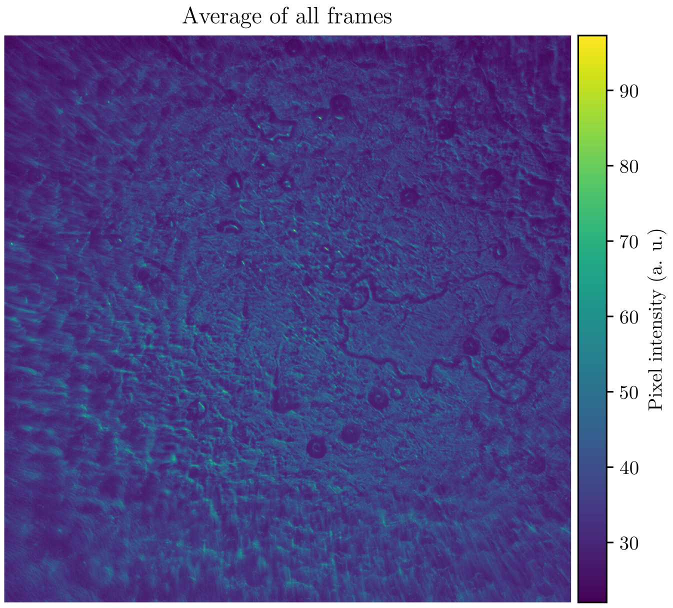

FIGURE 3.2: Example of the average of all frames after an acquisition of data for SCE imaging.

typical frame count used was $N = 3000$ pictures, yielding an acquisition time of less than 5 seconds. While the time for the camera to take 3000 frames is only 2.4 seconds at 125fps, some overhead from the Python language itself adds to the runtime. The result is saved to a file (*.npy, numpy pickle file) which is loaded by the script responsible for the next step.

3.2.1.2 Processing the raw data

A second script provides the processing needed before attempting phase retrieval, as described in section 3.1. The first computation made is the average frame, so it can be subtracted from all the frames to mitigate the incoherent component of light, as already described. An example can be seen in figure 3.2. The computation of the average frame does not come without a challenge: the data structure that holds the camera frames is a numpy array with 3 dimensions, being the different frames assigned across the first dimension. Numpy actually provides a function that calculates the average along a given axis, exactly what we need, but we cannot use it. The mentioned data structure uses either 8-bit or 16-bit unsigned integers as data type to store the values, depending on whether the 8-bit or 10-bit resolution modes of the camera is used. The averaging function of numpy casts all data into 64-bits, double precision, floating point numbers before doing the averaging, which would require more RAM than the 32GB available on the system used. Instead, we opted to use numpy's *sum* method, which can do the necessary sum along the first dimension in the unsigned integer type. We then cast the result into double precision floating point and divide by the number of frames of the acquisition. This results in only having one frame stored in floating point, rather than all the data.

Remember, from section 3.1 that now we have to: 1) subtract the average frames from all frames; 2) Fourier transform all frames; 3) average the transformed frames. In Python notation, each one of these steps would be actually just a single line of code and it would not require any kind of iteration to be involved. However, there is the problem of the data being in unsigned integer form and all the operations above needing it on double precision floating point. We can't just cast all the data into floating point at the same time, as that would exceed the maximum amount of system memory available. So what we did was to divide the processing into *nsteps* and only do the cast to floating point and the necessary processing only on portions of the data at a time and just accumulate the average. This is done resorting to this piece of code:

```
nsteps = 50
step=dataint.shape[0]//nsteps
for i in range(0,dataint.shape[0],step):
    data = dataint[i:i+step].astype(np.float_, casting="safe")
    data = data - mean  #Do the mean removal here
    data_ffted = fft.ifft2(data)
    mediaFT += sp.sum(sp.absolute(data_ffted)**2,axis=0)/dataint.shape[0]
```

This takes more computing time but it's the only way this can be done without running into memory space issues.

There is yet another challenge regarding practical implementation of out processing chain. As the average value of each frame is actually greater than 0, the centre of the Fourier transform, i. e., the DC component, grows very large and has no actual physical significance. To solve that, we make a histogram of the intensity values resulting from the previous processing, which corresponds to the correlation of the object, visually inspect it and threshold it. Figure 3.4 displays a typical histogram after performing the threshold cut-off. The maximum pixel intensity value 0.62 (arbitrary units) is reached by only one pixel. In fact, after the intensity value of 0.05, there are no other pixels with such high value, besides that one and its neighbours. Figure 3.3 shows a computed object autocorrelation after thresholding, obtained from a double slit sample. Finally, the thresholded

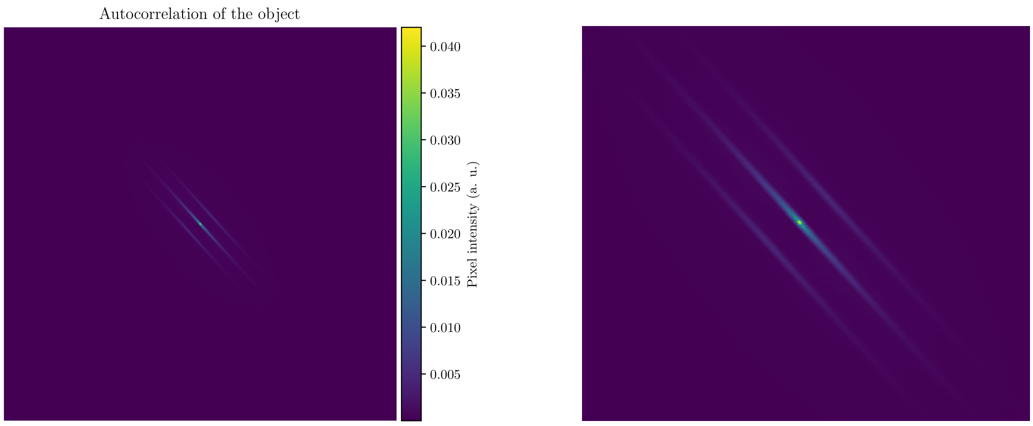

(A) Detail of the autocorrelation.

Computed object autocorrelation.

FIGURE 3.3: Computed object correlation of the double slit pattern.

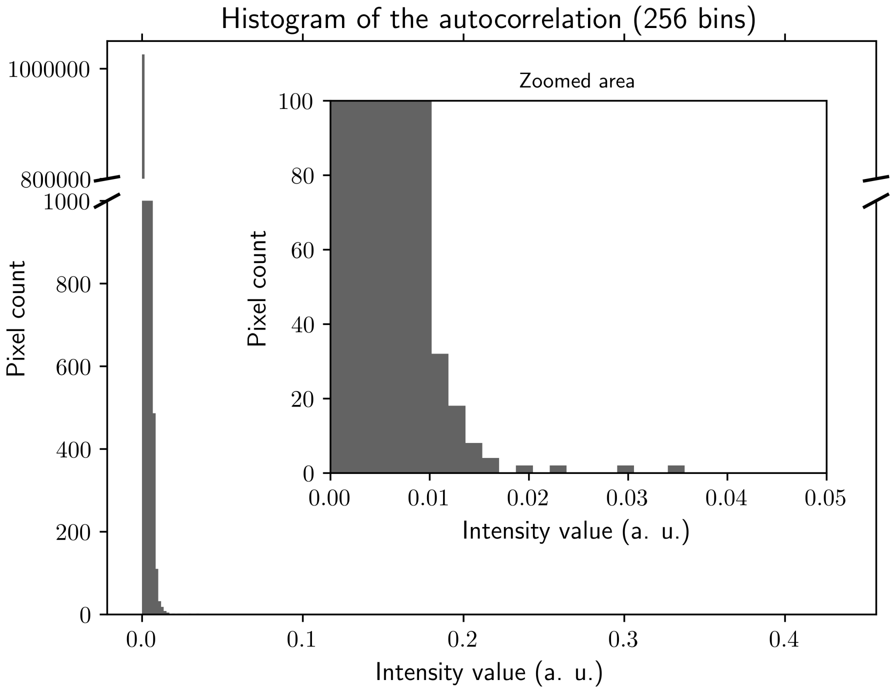

FIGURE 3.4: Histogram of the generated object autocorrelation.

autocorrelation is saved into a file (*.npy, numpy pickle) and we're ready for the next step.

At this point, we're also able to verify the far field condition as stated in section 3.1.1.1. Taking the absolute value of the Fourier transform of the autocorrelation we get what's shown in figure 3.5. This pattern is identified with what is expectable as the far-field diffraction pattern of a double slit, confirming that we are, in fact, in the far field condition, even though the distance between the object and the diffuser is around ten centimetres.

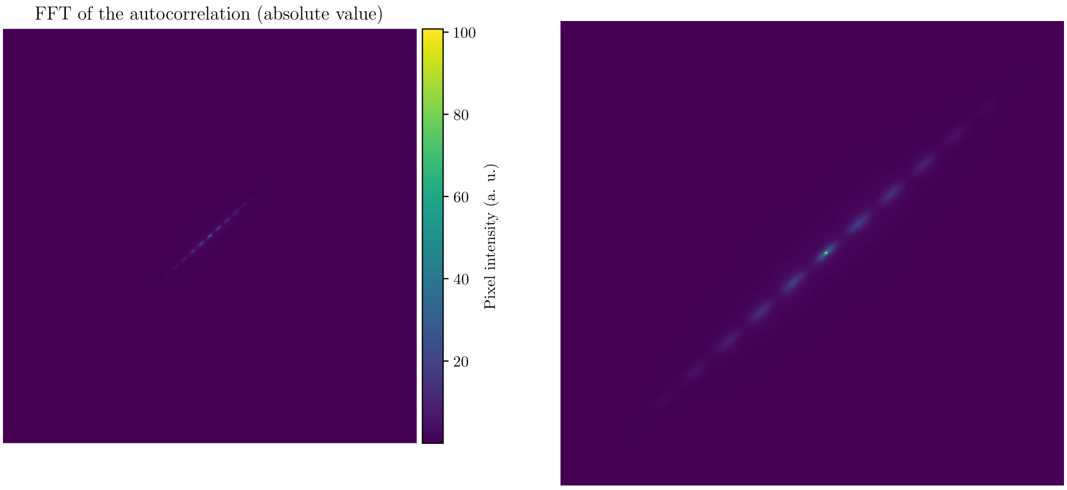

(A) Fourier transform of the autocorrelation of the object.

(B) Detail of the far-field pattern.

FIGURE 3.5: Fourier transform of the autocorrelation of the object evidencing the far-field pattern of a double slit pattern.

3.2.1.3 Phase retrieval

In our implementation of the phase retrieval algorithms, we start with a random image as the first $g_k(x, y)$. We start with the hybrid input-output algorithm: it runs varying the β parameter from 2 to 0.05 in steps of 0.05 . Each β is typically used for 20 iterations. This keeps on until the object domain error gets under a defined threshold or the maximum number of iterations is achieved. If the computed image error is still above the threshold the algorithm changes to the error reduction one, running until the error gets under the threshold or until the maximum number of iterations is achieved, typically 1000. After the algorithm is deemed complete, the resulting object image is stored into a *.png file.

As we've mentioned in section 3.1.3, we don't present a formal proof of convergence, but we can analyse it experimentally, analysing the error progression. We recorded the object domain error (equation 3.20) for both a hybrid input-output algorithm process, and for an error-reduction process. Results can be seen in figure 3.6. We can see that, for both algorithms, the trend is for the error to diminish. The error values between the two algorithms are not directly comparable, as these two algorithms have different working principles. This is justified by the fact that the error reduction algorithm always generates a valid object-domain image after each iteration while the same cannot be said for the hybrid input-output algorithm. In the latter, the object domain field at each iteration might still contain invalid points that count in the measuring of the object domain error. We can see that for the hybrid input-output algorithm the error progression starts with very slow rate of descent, increasing after the parameter β gets smaller. When β gets even smaller, the error drops slower. For the error-reduction algorithm, we can see that the error value drops dramatically in the first iterations, then diminishing slower as the iterations pass.

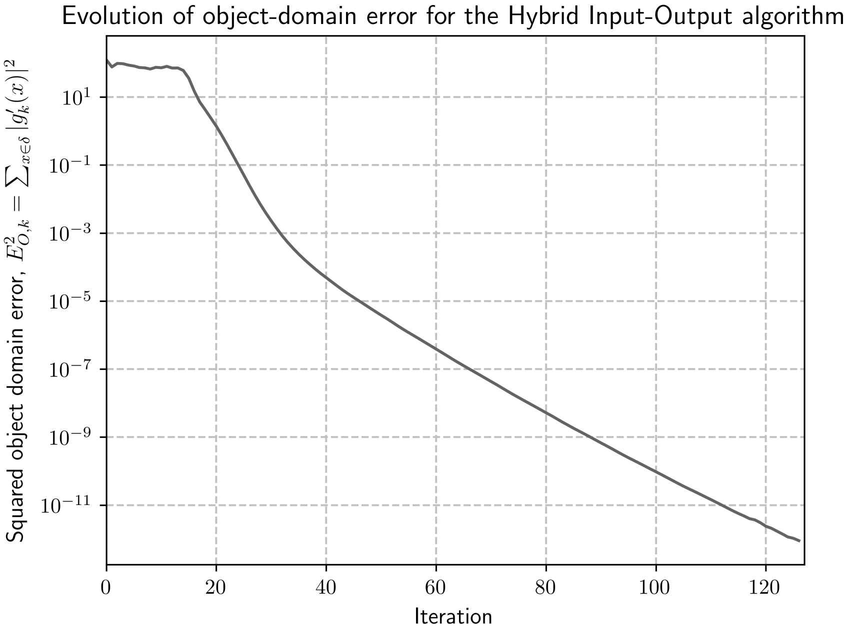

(A) Error function behaviour using the hybrid input-output algorithm.

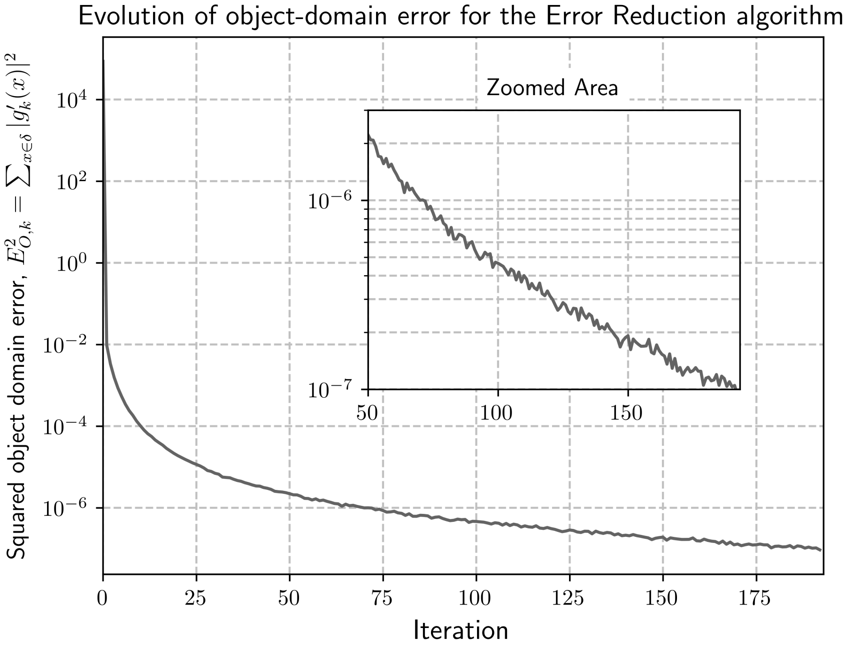

(B) Error function behaviour using the error-reduction algorithm.

FIGURE 3.6: Error function behaviours of the used algorithms in SCE imaging for phase retrieval.

3.3 Our results

Now that we've described out our process for SCE imaging we can discuss our results. For imaging targets, we used objects from the PASCO Scientific OS-8453 wheels (figure 3.7). We imaged a double slit from the multiple slits wheel ($a = 0.04$mm, $d = 0.25$mm) and the square and hexagonal patterns from the single slits wheel (figure 3.8). For every sample, we performed multiple attempts of phase retrieval process. The ones shown are either the best or the ones that provide useful info for discussion.

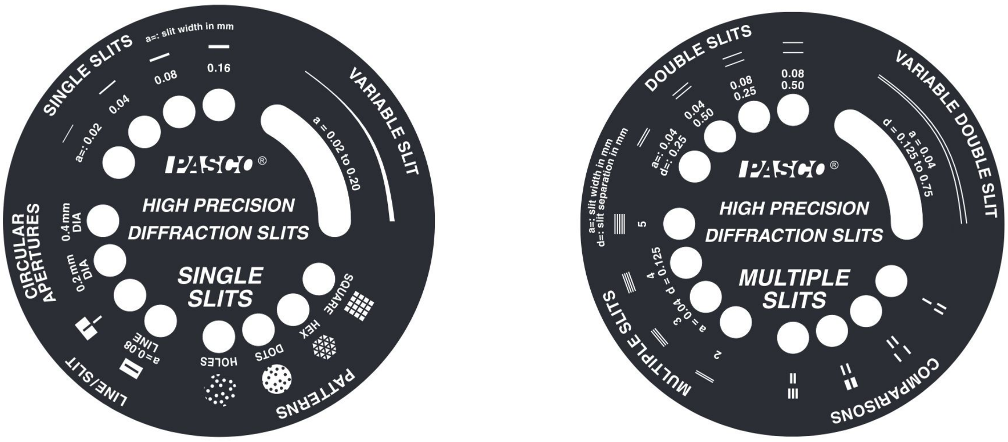

(A) Single slits wheel with composite patterns.

(B) Multiple slits wheel.

FIGURE 3.7: PASCO Scientific OS-8453 wheels [66].

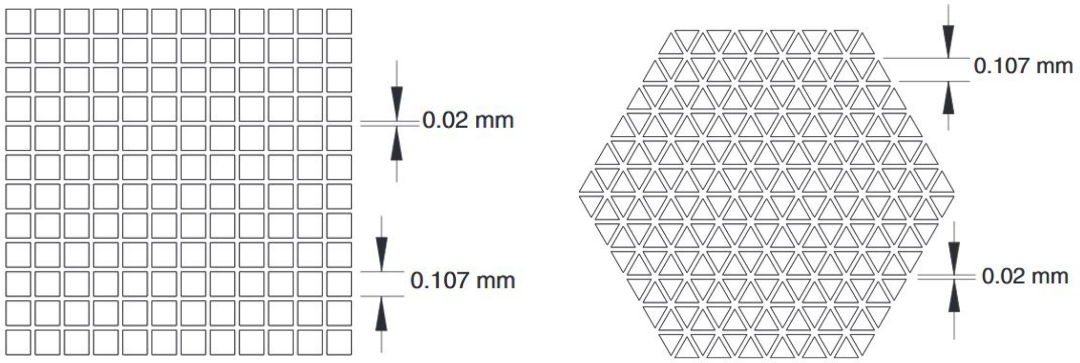

(A) Square pattern.

(B) Hexagonal pattern.

FIGURE 3.8: PASCO Scientific OS-8453 square and hex patterns from the single slits wheel [66].

3.3.1 Double slit

In figure 3.9 we can see an example of the double slit resolved after an attempt at phase retrieval. The slits are clearly resolved, although with some artefacts. At the same time, figure 3.9 presents an interesting insight to a limitation of the technique, already mentioned in section 3.1.3: the autocorrelation is a lossy operation and the position of the object in the image plane cannot be determined. This results in the effect observable in the mentioned figure 3.9c, where the retrieved object warps around the image plane.

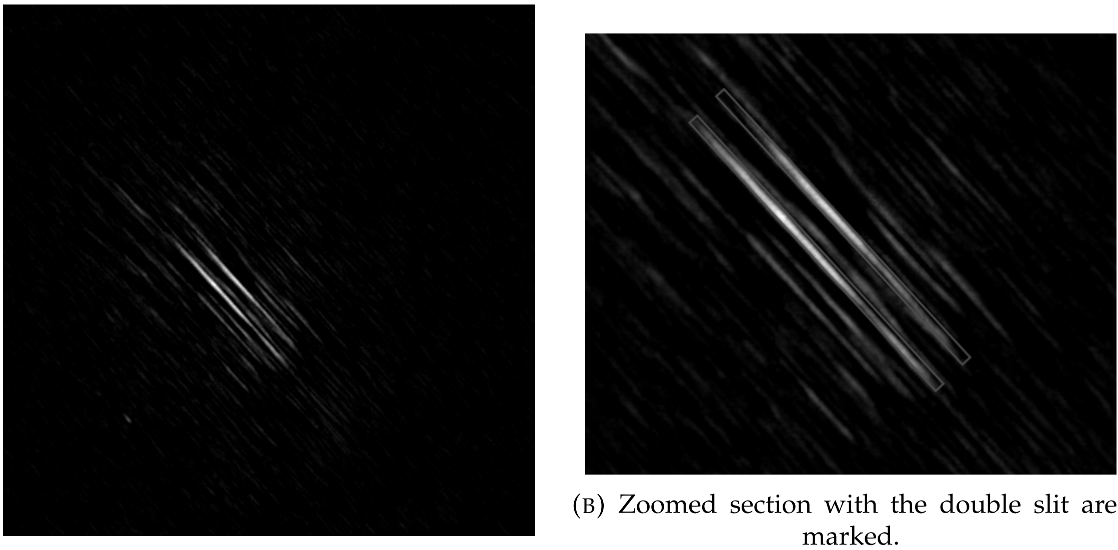

(A) Full image

(B) Zoomed section with the double slit area marked.

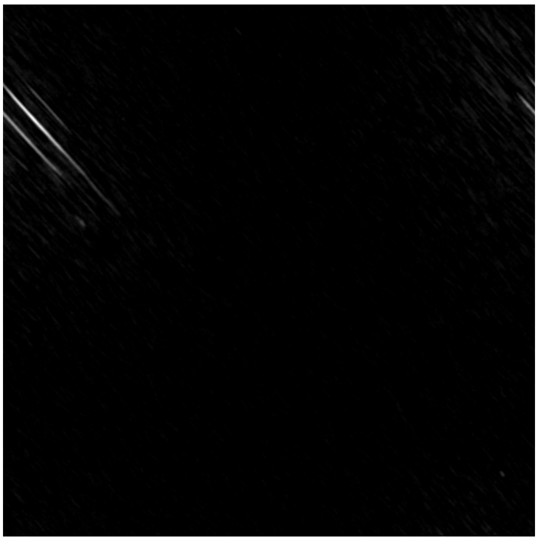

(C) Double slit resolved after phase retrieval from the autocorrelation where the warping effect is evident.

FIGURE 3.9: Double slit resolved after phase retrieval from the autocorrelation.

3.3.2 Square pattern

Figure 3.10a shows an image as acquired by the camera, demonstrating that no object information is observable directly. But, after our retrieval process, we get what's pictured on figure 3.10, which shows the square pattern clearly resolved, demonstrating out ability to retrieve complex patterns. We can see the pattern is Even the 0.02mm distance between the squares is resolved, demonstrating good resolution, despite the fact the surface of the diffuser is imaged into the camera with a simple imaging lens, not with a microscope objective. For this test pattern in particular, all the phase retrievals were very consistent, differing only on the position of the object on the plane, as discussed already.

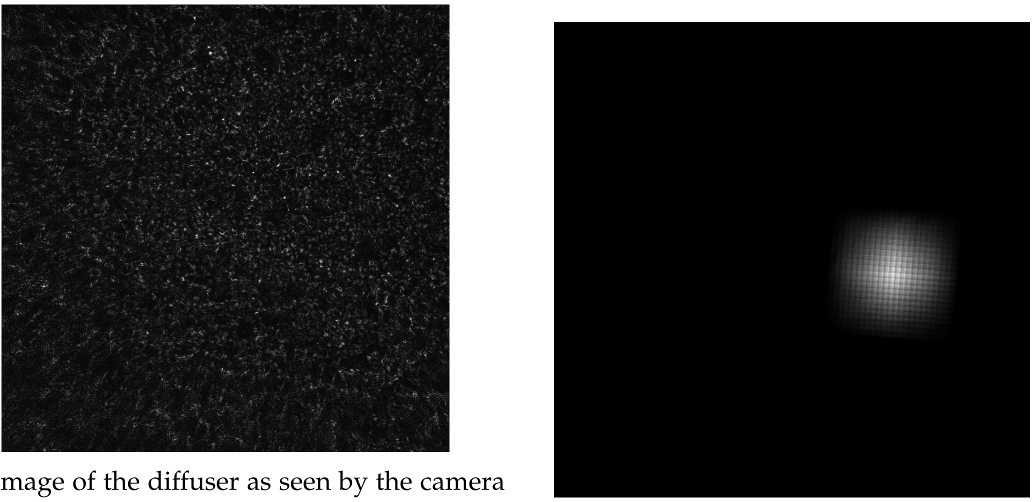

(A) Image of the diffuser as seen by the camera when testing with the square pattern. No object information can be trivially observed.

(B) Full image

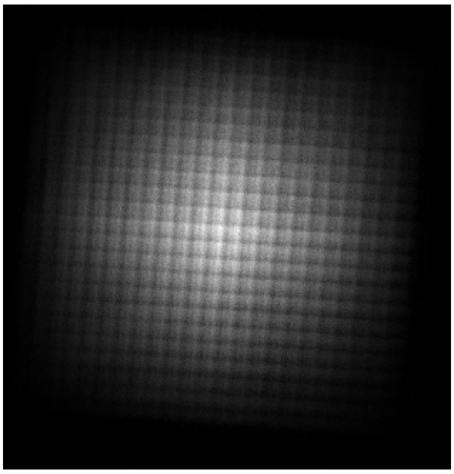

(C) Zoomed section.

FIGURE 3.10: Square pattern from the PASCO Scientific OS-8453 wheel resolved after phase retrieval.

3.3.3 Hexagon pattern

Mixed results can be seen on figure 3.11: while the smaller features of the pattern are resolved, exactly as the case for the square pattern, the technique could not resolve the whole area of the object, regardless of the attempts. This is likely due to the non-uniformity of the illumination light, making the edges too dark to be properly imaged.

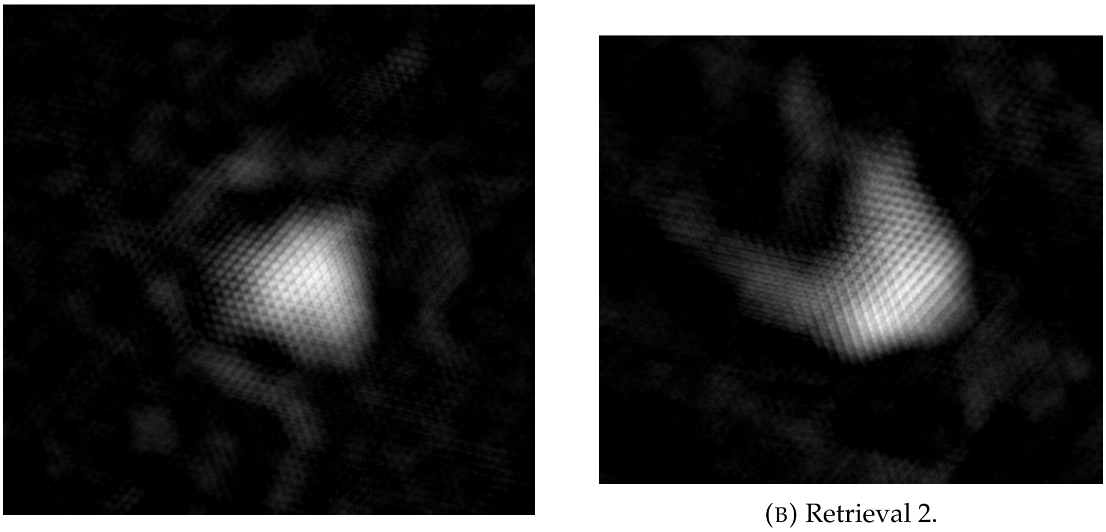

(A) Retrieval 1.

(B) Retrieval 2.

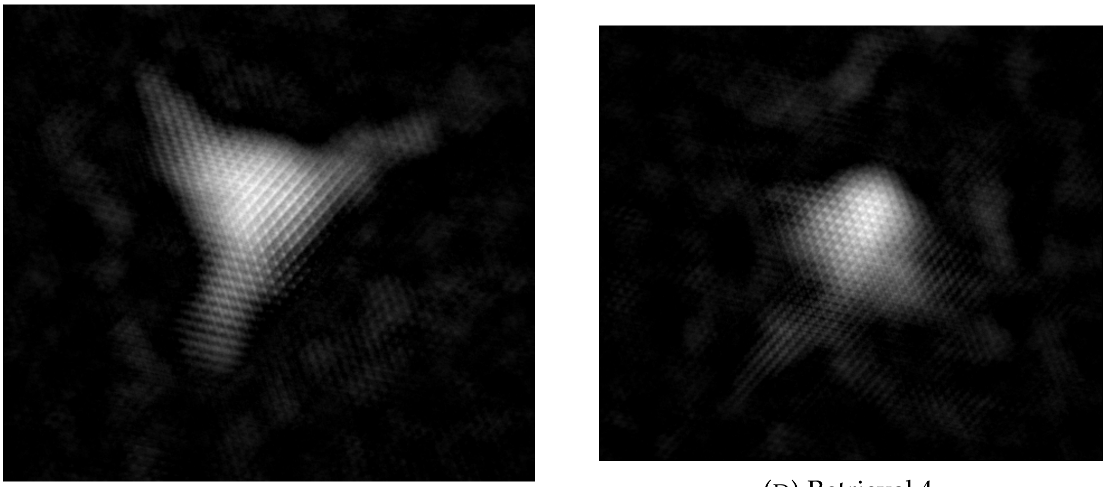

(C) Retrieval 3.

(D) Retrieval 4.

FIGURE 3.11: Hexagonal pattern from the PASCO Scientific OS-8453 wheel resolved after phase retrieval. Each retrieval attempt was cut to the area of interest.

3.4 Conclusions

We managed to build an imaging system based on the shower curtain effect. The optical setup is very simple, requiring no speciality optics other than the detector array. Micrometric features of objects behind scattering media were resolved without using microscopy apparatus. The data acquisition process can be made quick via the use of high frame-rate cameras and enough laser power to compensate for the short integration times. We acquired experimental proof of the shortened far-field condition due to the use of partially spatially coherent light. We demonstrated the effectiveness of phase retrieval algorithms, and demonstrated that the value given by the defined error function tends to decrease with each iteration.

The technique requires a lot of post-processing, with run-times in the order of several minutes when using a modern CPU* that are hard to optimize even using compiled software, rather than interpreted Python code. The data acquisition also results on big files which, for an acquisition containing 3000 camera frames yields about 4GBytes in size. The idea of optimizing the processing run-time with the resource to GP-GPU techniques is impractical: boolean operations, required for computing the δ-space are slow on this kind of processing hardware.

This technique is more stable using image arrays of uneven size on its dimensions (we used 1023×2013 pixels images). If the frame was of even side there would be no centre pixel, which corresponds to the position of maximum of the autocorrelation. Fast Fourier Transform (FFT) algorithms, used for computing Fourier transforms are dramatically faster at sizes that are powers of two or, at least, even.

Furthermore, as the hybrid input-output algorithm requires the object domain image from the previous iteration for the last step of the algorithm, the FFTs cannot be done "inline" (meaning that during the process of the FFT, the calculated values are stored in the same memory area as the source array), which would save on memory access times. All of this, along with the unpredictability of the phase retrieval algorithm, forcing the user to run the phase retrieval process multiple times to try and get the best image possible, make this technique very hard to develop into a real-time imaging system. Still on the reaml of disadvantages, the need for the object to be some distance apart of the second diffuser makes this technique limited in applications: objects actually enclosed in diffuse media cannot be imaged. Such is the case of imaging through biological tissue.

---

*Intel Core i7-2600, (4-core, 8-thread, 3.4GHz), 32GB RAM (DDR3 1600MHz, dual channel).

On a positive note, the technique still poses many advantages: the simplicity of the optical hardware is one of them. It does not require interferometric stability nor that either of the turbid media stay static. The diffuser between the illumination and the object is rotated to generate different speckle illuminations and for the second diffuser, the premise of the shower curtain effect does not require for it to stay static. If the second diffuser actually moves, it can help averaging out areas that might not be well illuminated due to any eventual particularly opaque spots on the diffuser.

The technique has applications like seeing around wall corners when implemented as an in-reflection system, as suggested by Edrei and Scarcelli [34]. The phase retrieval algorithms demonstrated their capabilities to reconstruct complex patterns, albeit with some limitations, as depicted on figure 3.11, demonstrating their capabilities.

For future work, the suggestion is to explore shower curtain effect imaging for microscopic imaging, and exploring the resolution limits of the technique.

Chapter 4

Measuring the Transmission Matrix: in-line reference techniques

Another technique we experimented in this work was controlling light propagating in complex media via the measurement of the transmission matrix (TM) using an in-line reference. Our work takes foundation in the work by Popoff et al. [23], Conkey et al. [24], Caravaca-Aguirre and Piestun [25]. The measurement of the TM allows for both imaging and manipulation of light through diffuse media. This kind of technique allows us to explore in light manipulation and opens a path for possible imaging techniques.

Having a full characterization of the input-output response of a given scattering media provides access to full control of the light travelling through it. The implementation of optical tweezers, single-pixel cameras or even direct imaging is possible from this knowledge. Besides, having a pre-characterization of the diffuse medium eliminates additional acquisition and processing time for manipulation or imaging, allowing for dynamic manipulation/imaging techniques. This makes this technique of immense value, and absolutely worth exploring.

In this chapter, we will begin with the theoretical background behind our system, then move onto describing our implementation, both at the software and hardware level, reveal our results, and finally discuss our conclusions.

4.1 Measuring the TM: how does it work?

We define the transmission matrix (TM) as the linear transformation between the input and output modes of an optical system. This means that for any linear optical system, the following holds true:

$$E_m^{\text{out}} = \sum_n k_{mn} E_n^{\text{in}} \tag{4.1}$$

where E_m^{out} is the electric field of a given output mode, m, E_n^{in} is the electric field of the n-th input mode, and k_{mn} is the complex valued element of the transmission matrix that describes the input-output relation between these modes.

4.1.1 Phase shifting interferometry

Determining k_{mn} can be done using the so-called phase shifting interferometry. Phase-shifting interferometry is a well studied subject [67–71] and its goal is to determine the phase component of a wavefront, $\Psi(x, y)$, from a series of interferometric measurements where the reference arm is phase-shifted by some predetermined set of values. To understand this, we shall begin with the intensity function of two coherent waves interfering at an interferometer [72]:

$$I(x, y; \phi) = I'(x, y) + I''(x, y) \cos\left[\Psi(x, y) + \phi\right] \tag{4.2}$$

where $I' = I_1 + I_2$ and $I'' = 2\sqrt{I_1 I_2}$, being I_1 and I_2 the intensity component of the wavefronts propagating on the individual arms of the interferometer, and ϕ is the artificially introduced phase shift in the reference arm. In the so-called four-phases algorithm, we measure $I(x, y; \phi)$ for $\phi = 0$, $\pi/2$, π , and $3\pi/2$. To simplify the notation, we'll drop notating the spatial dependence, and $I(x, y; \phi)$ will simply be notated as I_ϕ. These 4 measurements yield:

$$\begin{aligned}
I_0 &= I' + I'' \cos(\Psi) \\
I_{\pi/2} &= I' - I'' \sin(\Psi) \\
I_\pi &= I' - I'' \cos(\Psi) \\
I_{3\pi/2} &= I' + I'' \sin(\Psi)
\end{aligned} \tag{4.3}$$

which can be applied in determining for the phase component of the wavefront:

$$\Psi(x, y) = \arctan\left[\frac{I_{3\pi/2} - I_{\pi/2}}{I_0 - I_\pi}\right] \tag{4.4}$$

4.1.2 In-line phase shifting interferometry as way to measure the TM

This ideas was adapted for in-line measurement of the TM [23]. When injecting light into a diffuse medium, we consider only a limited number of spatial modes as controllable input modes. The others play the role of reference. This can be done in practice with an

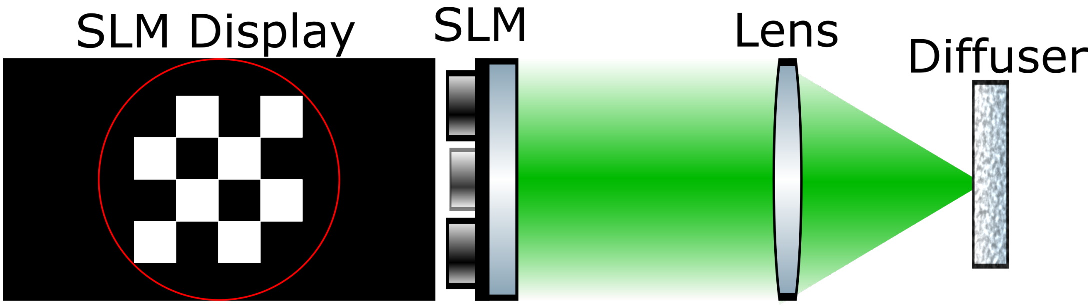

FIGURE 4.1: SLM modulation scheme. The area on the left represents the whole area of the SLM display. The red circle denotes the area that the lens captures into the diffuse media.

SLM, by focusing the spatially phase-modulated plane waves coming out from the SLM onto the scattering medium, making so that each (macro)pixel on the SLM controls an independent input mode, as illustrated in figure 4.1. In this figure we can see that, inside the area captured by the focusing lens, a Hadamard basis element is displayed, while the surrounding area serves as phase reference. This square-in-a-circle scheme dictates that about 64% of the light entering the lens is from the basis element and 36% is from the phase reference. This reference area will be scattered in the diffuse media and produce a speckle pattern at the output. We'll write the complex electrical field of this speckle pattern as s_m where, again, the subscript m refers to a particular output mode. Re-writing equation 4.2 with the information from equation 4.1, we get:

$$I_{m,\phi} = \left|E_m^{\text{out}}\right|^2 = \left|s_m + \sum_n e^{i\phi} k_{mn} E_n^{\text{in}}\right|^2 \tag{4.5}$$

Making measurements for a particular input mode, n, with $\phi = 0, \pi/2, \pi$, and $3\pi/2$, we can write:

$$\frac{I_{m,0} - I_{m,\pi}}{4} + i\frac{I_{m,3\pi/2} - I_{m,\pi/2}}{4} = s_m^* k_{mn} E_n^{\text{in}} \tag{4.6}$$

One can see already that the measurements do not provide k_{mn}, but rather $s_m^* k_{mn}$. This is actually not a problem. As the SLM is a phase-only modulation device, the reference area used for this technique will reflect light regardless of whether we are in calibration mode or not. This means that we will have a static reference speckle at the output of the complex medium coming from what was previous the phase-shifting reference area. We can interpret $s_m^* k_{mn}$ as being the effect of the n-th input mode over the static speckle reference at the output mode m.

From the characterization of the complex medium by the matrix defined by $K_{\text{obs},mn} = s_m^* k_{mn}$, we are ready to manipulate light propagating through it. If we define E^{target} as the target output electrical field at the detection plane, we can determine the input vector that will produce this target output field after going through the characterized, complex optical system:

$$\overrightarrow{E^{\text{in}}} = K_{\text{obs}}^{-1} E^{\text{target}} \tag{4.7}$$

This $\overrightarrow{E^{\text{in}}}$ is a vector whose components represent the contribution of each input mode. So, the input field is the sum of each input mode weighted by the respective component of $\overrightarrow{E^{\text{in}}}$:

$$E^{\text{in}} = \sum_n \overrightarrow{E^{\text{in}}} \cdot E_n^{\text{in}} \tag{4.8}$$

However, computing K_{obs}^{-1} is challenging. Usually K_{obs} is not a square matrix and it might not be computation friendly, as computer algorithms favour matrices that have a high diagonal mass ratio and values within a close range, two characteristics we do not expect to find in transmission matrices, making numerical computation of the (pseudo)inverse very hard. However, we can perform a simple test for the validity of the measures transmission matrix by focusing light through the diffuse media. This requires choosing an output mode and computing $\overrightarrow{E^{\text{in}}}$ in a way that guarantees constructive interference in the selected output mode. This is achieved when:

$$\overrightarrow{E^{\text{in}}} = K_{\text{obs},m}^{*} \tag{4.9}$$

where $K_{\text{obs},m}$ means the m-th line of K_{obs}.

4.1.3 A Hadamard basis as input wave basis

The choice of an adequate wave basis system for this setup is of the uttermost importance. For the output wave basis, it is trivial to use the canonical wave basis. Repeating the process previously discussed, we can make independent output wave modes correspond to a specific (macro)pixel on the camera sensor plane simply by focusing a lens at the desired output plane. However, the canonical plane wave basis is not suitable as input basis. Since we're using a phase-only modulator, any given input mode on the canonical basis, which, again, is described by a (macro)pixel on the SLM plane, will see the rest of the area around it as reference. This brings two problems: first, the visibility of the effect of this input mode will be severely crippled because only a small portion of the light is actually from the mode, being the overwhelmingly majority from the reference, and secondly, what was supposed to be a static speckle reference for all modes actually

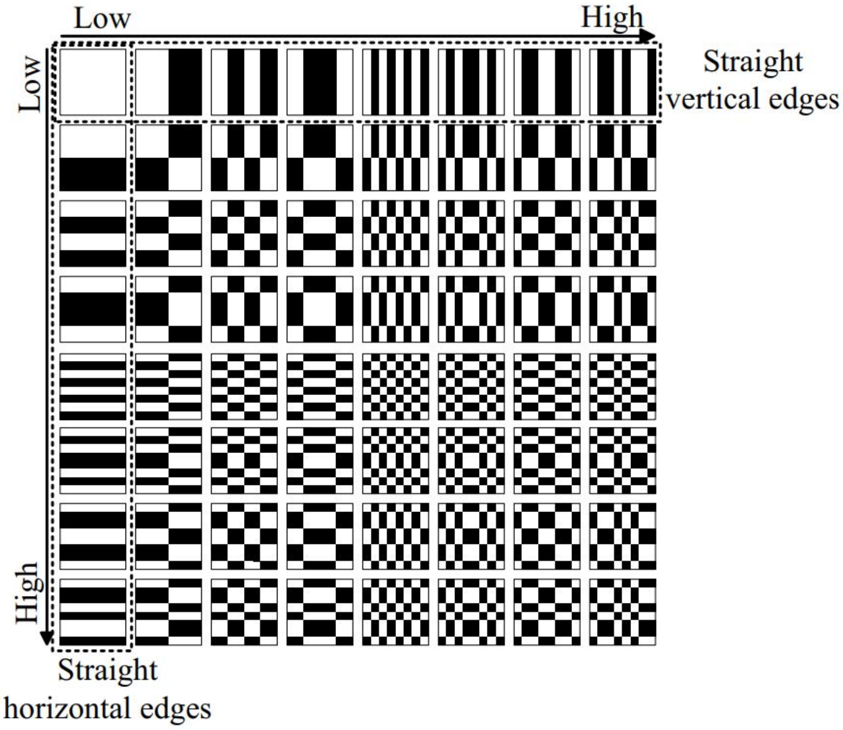

FIGURE 4.2: 64 modes Hadamard basis. The modes are in dyadic order, in the direction of the marked axes. White and black indicate amplitude $+1$ and -1 respectively. Figure by Park [73].

change with the mode being tested. The reference area is everywhere but in the area of the mode being tested so, for each input mode, the reference area is everywhere but in that mode's area, violating the static condition. So we need a different solution for an input basis system: an orthogonal basis whose elements all occupy the same area in the SLM display. The Hadamard basis provides exactly this: on a Hadamard basis system, all the components from the basis vectors are either $+1$ or -1 in amplitude, which we translate as a 0 or π phase shift on light reflected on the SLM. Using this basis, each independent input mode uses the same area on the SLM: exactly the area defined to be modulated, which both massively improves SNR and guarantees our static reference condition. Figure 4.2 illustrates a 64 modes Hadamard basis.

4.2 Our implementation of TM measurement

The setup for our implementation can be seen on figure 4.3. The objective represented by L2 transforms wave vectors at the desired output plane into spatial positions at the camera's sensor plane. We perform our calibration for an arbitrary plane away from the complex media's surface as, in practice, our goal might be to image or manipulate objects

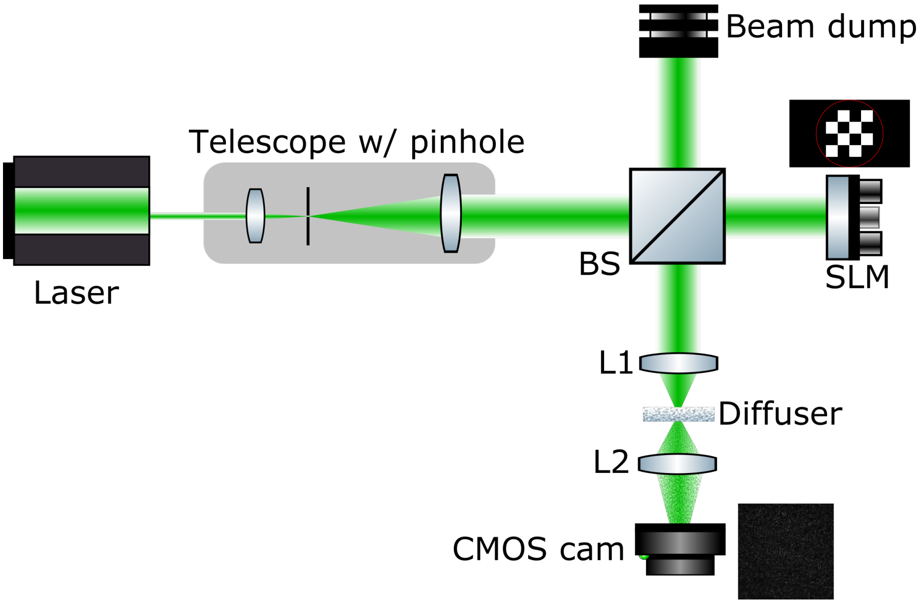

FIGURE 4.3: Optical setup for TM measurement. Laser: 532nm, SUWTECH LASER; telescope w/ pinhole: pinhole diameter 5 μm, microscope objective, 20x, NA = 0.4, biconvex lens, 10cm focal length; Beam splitter for 532nm from Altechna, 50/50; L1 and L2: microscope objectives, Edmund Optics, 40x, NA = 0.65; CMOS camera from Ximea (as described in chapter 2). The diffuse media used was built from stacked translucent tape strips.

FIGURE 4.4: Material used as diffuse media for TM measurement. The object is optically opaque.

that are away from the diffuse media, not over it. The diffuse media used for testing was made of sheets of translucent tape and it can be seen on figure 4.4. Some tests were also performed using an optical fibre as complex media (diameter 600 μm, NA = 0.39, length 2.5m). We kept the imaging lens but we used a Thorlabs fibre collimation lens, model F240SMA-532, for light input, as this provides an alignment-less solution to the correspondence between pixels on the SLM and input wave modes at the fibre.

4.2.1 The code

The software in our implementation is split into four stages. First, we must generate the appropriate Hadamard basis, plus the calibration frames, which consist of the Hadamard basis elements surrounded by the different reference phase shifts. Secondly, the acquisition process takes place. After that, the acquired frames are processed to obtain the TM. The last step consists on testing the validity of the TM using a script that computes the input field to focus light at a given point on the target plane.

4.2.1.1 Generating the Hadamard basis

As mentioned, the first step is to generate the set of elements to form the basis and to generate the frames to be displayed on the SLM during the calibration process. To generate the Hadamard basis elements we first need to generate a Hadamard matrix of adequate dimension. While Hadamard matrices can have arbitrary dimension, computing them isn't always easy [74, 75]. The method by Sylvester [76] generates Hadamard matrices of size 2^n where n is a positive integer. This method of generating Hadamard matrices is available through the linear algebra package of *scipy*. This means that the basis dimension is limited to powers of four, as the basis dimension is the square of the number or lines/-columns of the Hadamard basis. We used a basis of 256 elements (Hadamard matrix of size 16), which implies the use of 1024 calibration frames for the 4 phases method. We also run tests with a basis of dimension 1024 (Hadamard matrix of size 32). The process for generating the basis elements goes as follows:

1. Generate the Hadamard basis of size n. As an example, we use size 4:

$$H^4 = \begin{bmatrix} 1 & 1 & 1 & 1 \\ 1 & -1 & 1 & -1 \\ 1 & 1 & -1 & -1 \\ 1 & -1 & -1 & 1 \end{bmatrix} \tag{4.10}$$

2. Go through each combination of line and column in the Hadamard matrix and "meshgrid" them. Meshgrid is an operation that returns coordinate matrices from coordinate vectors, meaning that we get two 2D coordinate arrays, given one-dimensional coordinate arrays $\mathbf{x}_1$ and $\mathbf{x}_2$. These coordinate arrays have dimension $\dim \mathbf{x}_1 \times$

$\dim \mathbf{x}_2$. For illustration purposes we'll make $\mathbf{x}_1 = (a_1, b_1, c_1)$ and $\mathbf{x}_2 = (a_2, b_2)$:

$$\begin{aligned} \underset{\mathbf{x}_1,\mathbf{x}_2}{\text{meshgrid}}\, \mathbf{x}_1 &= \begin{bmatrix} a_1 & b_1 & c_1 \\ a_1 & b_1 & c_1 \end{bmatrix} \\ \underset{\mathbf{x}_1,\mathbf{x}_2}{\text{meshgrid}}\, \mathbf{x}_2 &= \begin{bmatrix} a_2 & a_2 & a_2 \\ b_2 & b_2 & b_2 \end{bmatrix} \end{aligned} \tag{4.11}$$

Picking the second line and fourth column of our example Hadamard matrix:

$$\begin{aligned} \text{meshgrid} \begin{pmatrix} 1 & -1 & 1 & -1 \end{pmatrix} &= \begin{bmatrix} 1 & -1 & 1 & -1 \\ 1 & -1 & 1 & -1 \\ 1 & -1 & 1 & -1 \\ 1 & -1 & 1 & -1 \end{bmatrix} \\ \text{meshgrid} \begin{pmatrix} 1 \\ -1 \\ -1 \\ 1 \end{pmatrix} &= \begin{bmatrix} 1 & 1 & 1 & 1 \\ -1 & -1 & -1 & -1 \\ -1 & -1 & -1 & -1 \\ 1 & 1 & 1 & 1 \end{bmatrix} \end{aligned} \tag{4.12}$$

3. Multiplying these two matrices element-wise, we get the Hadamard basis element:

$$H^4_{2,4} = \begin{bmatrix} 1 & -1 & 1 & -1 \\ -1 & 1 & -1 & 1 \\ -1 & 1 & -1 & 1 \\ 1 & -1 & 1 & -1 \end{bmatrix} \tag{4.13}$$

To use this generated Hadamard basis on the SLM, we have to scale these matrices, so that each element actually becomes a macro-pixel on the SLM display. For that we can take advantage of the Kronecker's product. As an example, to scale a matrix by a factor of two, we generate a two-by-two matrix of ones and apply the Kronecker's product, as demonstrated by this example:

$$\begin{pmatrix} a & b & c \\ d & e & f \\ g & h & i \end{pmatrix} \otimes \begin{pmatrix} 1 & 1 \\ 1 & 1 \end{pmatrix} = \begin{pmatrix} a & a & b & b & c & c \\ a & a & b & b & c & c \\ d & d & e & e & f & f \\ d & d & e & e & f & f \\ g & g & h & h & i & i \\ g & g & h & h & i & i \end{pmatrix} \tag{4.14}$$

This process only allows for scaling by integers factors. Since the goal is to have the basis element fit to the circle defined by the input aperture of the microscope objective, as previously shown in figure 4.1, this becomes a limiting factor. Because of this integer-only scaling and that the size of the generated Hadamard basis is always a power of four, each basis element occupies an area given, in pixels, by $m \times 2^n$. For our specific configuration, the Hadamard basis elements have a size of 480 × 480 pixels for the Hadamard basis of dimension 256 (matrix of size 16), meaning a scaling factor of 30.

The last step is to include each basis elements in "container frames" for calibration: for each basis element and each reference phase for calibration, we generate an "empty" frame whose value is the grey level corresponding to the necessary phase modulation, and we set the middle region of the frame to be the Hadamard basis element. Both the Hadamard basis and the calibration frames are stored into a file for use in the following steps of the process.

4.2.2 Acquiring calibration data

For acquiring the calibration data, a second Python script is used. The desired basis parameters are set and the script loads the file containing that basis, given it exists. The script initializes the camera and sets the defined exposure and gain parameters. The SLM library is also initialized at this point. The data acquisition happens at this point. Despite the maximum display rate of the SLM being 60 frames per second, as discussed already in section 2.1.1, the devices is working in its most phase stable mode, resulting in the fact that the SLM takes extra time to update the displayed frame. This extra time, in the order of the dozens of milliseconds, forced the introduction of an artificial pause time between 100 and 200 milliseconds between the instruction for the SLM to update its displayed image and actually acquiring from the camera. This dramatically reduces the effective capture rate to less than ten frames per second, leading into acquisition times in the order of several minutes. A typical 1024 frames acquisition for calibrating a 256 element basis using the four phases methods takes around five minutes.

After the acquisition is complete, the data from the camera is saved into a file for post-processing.

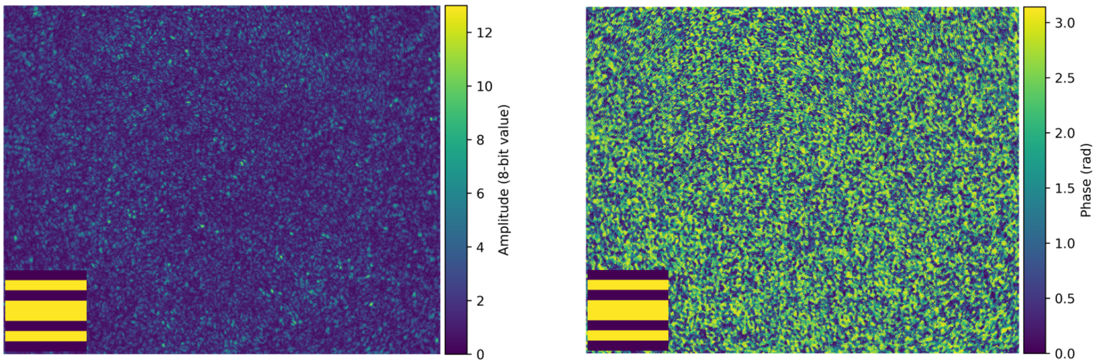

(A) Amplitude plot.

(B) Phase plot.

FIGURE 4.5: Propagation of a given Hadamard basis element through the diffuse media. The basis element in question is displayed in the insets in the plots.

4.2.3 Computing the TM

Having the calibration data, we can compute the TM by implementing 4.6. The resulting TM will have a dimension given by the number of input modes and the number of output modes. For the case where a 256 element basis was used, and the camera is set in its downsampling mode, with a resolution of 512 × 640 pixels, the transmission matrix has a dimension of 327680 lines by 256 columns. We can select a given column of the matrix and reshape it back into the dimensions of the camera sensor to observe how a given mode of the input basis gets propagated to the output. This is illustrated in figure 4.5. Alternatively, we can also take a look on how all the basis elements affect a given pixel. Figure 4.6 shows, as an example, how the different input modes affect the centre pixel.

4.2.4 Manipulating light using the TM

After obtaining the TM, we can use it for manipulating light through the turbid medium. As previously mentioned (section 4.1), focusing light through the turbid medium is an appropriate test to the validity of our TM, hence we developed a Jupyter notebook for this purpose. Given a selected pixel at the camera , which corresponds to a line on the TM, the script computes $\overrightarrow{E^{\text{in}}}$ and E^{in}, as per equations 4.7 and 4.8, and displays the computed phase mask on the SLM display. Because E^{in} is complex-valued, we have to discard any amplitude information as the SLM used is a phase-only spatial light modulator. The reference area is kept at the “black” level, corresponding to no phase shift.

Focusing light, by definition, concentrates light spatially. This means that using the exposure and gain settings for the camera used while acquiring the calibration frames

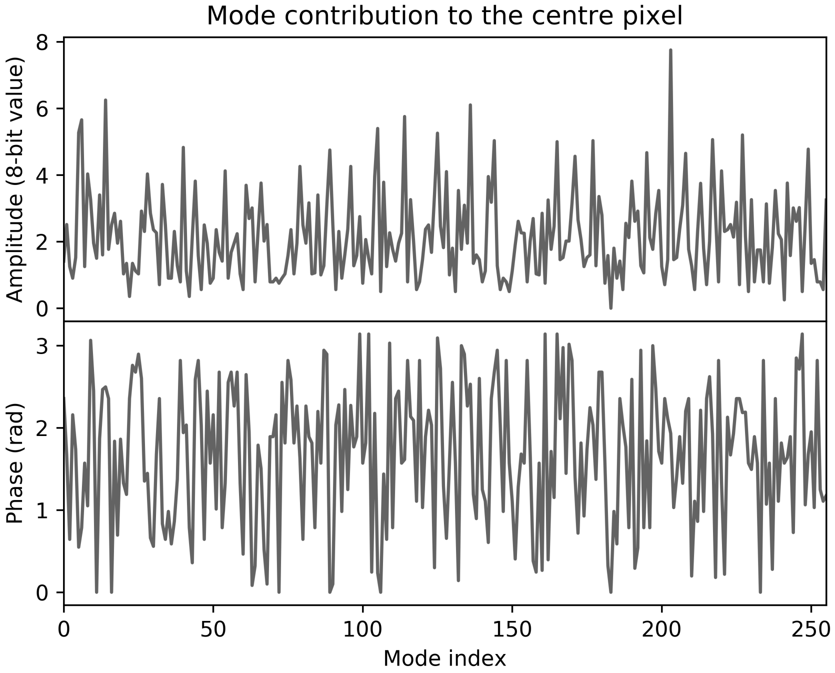

FIGURE 4.6: Contribution of the several modes for the centre pixel.

might result in the camera sensor overloading. During the focusing process, the script automatically adjusts the camera settings so that the intensity of light in a given region around the pixel (mode) chosen for focusing is under a definable threshold.

4.3 Our results

We tested the ability to perform a calibration of the transmission matrix on both the diffuser shown in figure 4.4, and on a multimode optical fibre (diameter 600 μm, NA $= 0.39$, length 2.5m).

4.3.1 Diffuser

To measure the TM of the diffuser, we used a 256 modes basis. Figure 4.7 showcases a spot focused through this medium. The intensity at the region of the focus is about 18 times more intense than the average background intensity.

To demonstrate we are are also capable to focus elsewhere we can resort to the so-called focusing operator [23], defined as:

$$O_{\text{foc}} = K_{\text{obs}} K_{\text{obs}}^{\dagger} \tag{4.15}$$

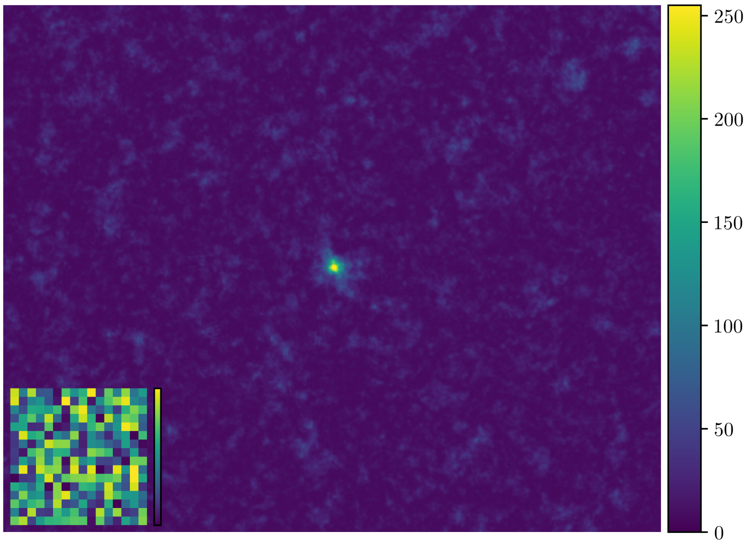

(A) Image after focusing though the turbid media. The inset shows the input array as displayed on the SML.

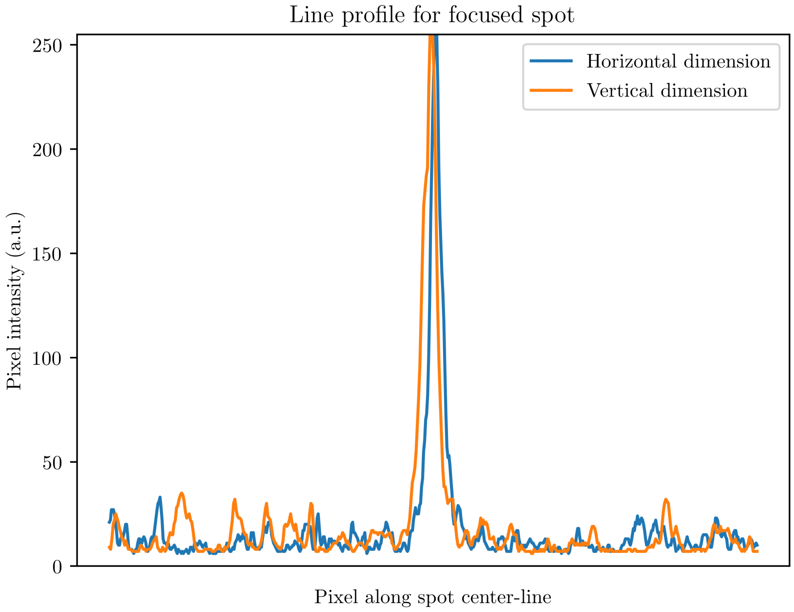

(B) Line profile cut around the centre of the focused spot.

FIGURE 4.7: Light focused on the diffuse media via the calibrated TM.

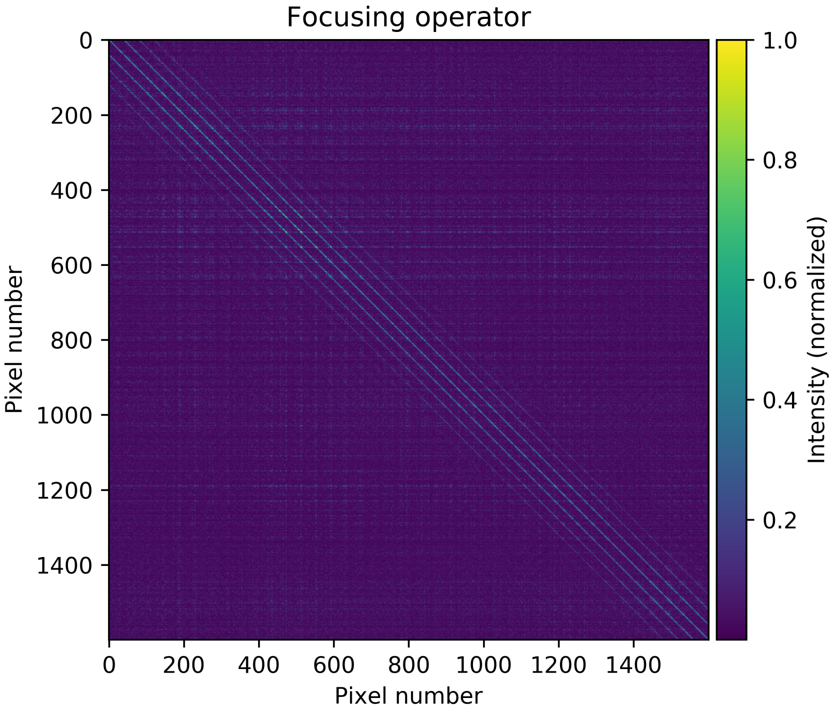

FIGURE 4.8: Normalized focusing operator for a region of 40 × 40 pixels around the centre pixel. Indexing starts at the top-left and counts to the right and then down one line at the time.

In essence, what this operation does is checking the output response of all modes when the input field is the complex conjugate of a particular pixel. This allows us to predict how trying to focus on a particular pixel will affect all other pixels. Figure 4.8 shows the results for a square region, 40 pixels wide, around the centre pixel. The strong diagonal means that we can, in principle, focus on any of these stops. The secondary diagonals mean that there is a certain correlation between the pixel we want to focus on and neighbouring pixels. This is due to the fact that the magnifying system used at the output plane makes each speckle spot, which correspond essentially to independently controllable output modes, occupy an area larger than a single pixel at the output, which visually holds true in figure 4.7.

4.3.2 Optical fibre

Results when using the optical fibre can be seen on figure 4.9. Here the signal to background ratio has the value of 8.7, which is considerably smaller than the diffuser case. This mostly has to do with the far greater number of different speckle spots observable at the output of the fibre, meaning that we have a considerably higher number of output

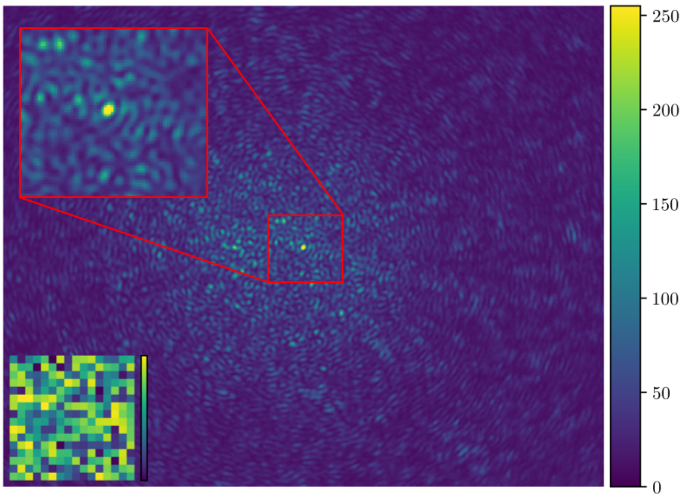

FIGURE 4.9: Light focused through an optical fibre. The inset shows the phase mask as displayed on the SLM.

modes to be controlled than before. This becomes overwhelming for the relatively small availability of independent input modes.

4.4 Discussion and conclusion

With this experiment, we successfully managed to build a light manipulation scheme by determining the transmission matrix of the optical system where light propagates. The acquisition time for a 256 input modes calibration using the four-phases method is around 5 minutes. We verified experimentally the validity of the computed TM by focusing light both through a diffuse medium and via fibre optics. We also analysed the focusing operator as way of predicting where focusing is possible, given the TM correctly describes the optical medium.

This system requires the diffuse medium to be absolutely static during both calibration and operation. This is a clear disadvantage of this approach. The generation of the Hadamard basis elements with Sylvester's method also generates a problem: given that the Hadamard matrices used as source for the wave basis have a size that is a power of two, the number of elements of a basis can only change by a factor of 4. An acquisition featuring 256 basis elements takes around 5 minutes, and since the next possible number of input basis elements is 1024 elements, the acquisition time would be around 20 minutes. This becomes impractical for most applications. On the other hand, once the optical medium is fully characterized, we can manipulate light in the medium just by computing the inverse of a matrix or, for the case of focusing, just by finding the complex conjugate of the elements of the TM for a particular output mode. This means that changing the wavefront becomes a computational problem and its speed depends only on the computational power available. This is an advantage over optimization algorithms, as we shall explore in the following chapter.

Another problem we were also faced with has to do with the reference speckle light. As the reference speckle comes from the outside regions of the input aperture of the lens after the SLM, rather than from a separate interferometric arm, it is necessary to be very careful about having enough light for interferometric visibility. This proved to be a problem when using optical fibres as propagating medium and using a fibre collimation package as input lens, as it is not possible to be absolutely certain about what's actually coupling to the fibre.

For future work, it would be interesting to explore this light manipulation technique for practical use cases. Optical trapping and imaging would both be of interest. For trapping, this technique could be interesting for dynamical optical trapping via fibre optics. In the imaging side, this technique can be used as a spot-scanning vision system, using a detector for the back-scattered light.

During our experimentation at the lab we experimented with the use of a DMD as the source of phase modulation using Lee Holography, because it allows for high-speed reconfiguration. However, due to time constraints, this path is left as a suggestion for further exploration. The use of the DMD would allow for acquisition times in the realm of just a couple of seconds, massively improving the time necessary to compute the TM, at the expense of complicating the optical system.

Chapter 5

Manipulating light via optimization algorithms

The third experiment developed during this work has to do with light manipulation using optimization algorithms. In this approach, rather than fully characterizing our diffuse medium, we use an iterative process to determine the input field that generated the desired output. This technique is relevant as a mean for light manipulation through complex media, with applications like optical tweezers using fibre optics and single-pixel camera systems.

While an optimization technique may seem limiting at first, as it requires a new input field to be computed every time the target function changes, this can actually be exploited positively. Computing the TM from the reference frames is computationally expensive and requires complex number algebra. This inhibits the possibility of porting this technique to embedded devices or single board computers (SBCs), as they would not provide enough computational power or memory availability. Besides, re-computing the TM in the case of dynamic media is slow and might actually be outdated by the time it is done. Conkey et al. [24] actually demonstrated how optimization techniques can be used for sub-second reconfiguring in focusing light through turbid media.

We take foundation in the work by Conkey et al. [24], Vellekoop and Mosk [29, 30]. This experiment uses the same optical setup as the one already described in section 4.2 from the previous chapter, used for acquiring the TM, requiring only an additional coding effort, hence experimenting with this technique comes as a natural step to take.

In this chapter, we will start by describing the working principles of phase-only optimization algorithms and then we will describe how we tackled this problem in our particular implementation. We will show our results, and how the functional parameters if the algorithm affect it, and then we will present our conclusions and a roadmap for further exploration.

5.1 Phase-only optimization: how does it work?

As we've discussed in previous chapters, our device for wavefront control is a phase-only spatial light modulator, eliminating the possibility of amplitude modulation on the controlled input modes.

First, let's remember the input-output relation of propagating modes in complex media, which we had defined already in section 4.1:

$$E_m^{\text{out}} = \sum_n k_{mn} E_n^{\text{in}} \tag{5.1}$$

To separate the amplitude and phase components of the elements in this equation, we make $E_n^{\text{in}} = \left|E_n^{\text{in}}\right| e^{i\phi_n}$ and $k_{mn} = |k_{mn}|\, e^{i\theta_{mn}}$:

$$E_m^{\text{out}} = \sum_n |k_{mn}| \left|E_n^{\text{in}}\right| e^{i(\theta_{mn}+\phi_n)} \tag{5.2}$$

For every m-th output mode, each n-th input mode will contribute with an amplitude given by $|k_{mn}| \left|E_n^{\text{in}}\right|$ and with a phase shift given by $(\theta_{mn} + \phi_n)$. In our optimization scheme, we can only control ϕ_n .

Now, let us assume we want to optimize for some binary intensity function at the output plane. In essence, the goal is to maximize the intensity of light in some regions of the output plane and minimize it in the others. This is the case when focusing through complex media, as we aim to achieve a small spot of light at the defined output plane. We define the δ-space as the set of points in the output plane where we *want* to concentrate light on. The intensity of light in this region, as captured by the camera, is given by:

$$I_\delta^{\text{out}} = \sum_{m\in\delta} \left| \sum_n |k_{mn}| \left|E_n^{\text{in}}\right| e^{i(\theta_{mn}+\phi_n)} \right|^2 \tag{5.3}$$

I_δ^{out} reaches is maxima when the set of input phases, ϕ_n, maximizes the sums. In the case of a single focus target, δ consists of just the output mode (pixel) m where we want to focus on.

As this technique does not involve characterizing the complex medium, it is not possible to compute the set of ϕ_n that achieves this condition. Instead, we go through each n-th input mode and sweep the phase ϕ_n to find the one that best suits our target, i. e., the one that maximizes I_δ^{out}.

Different options are available on how to iterate over these input modes. Vellekoop and Mosk [30] present three approaches: the "stepwise sequential algorithm", the "continuous sequential algorithm" and the "partitioning algorithm". In the stepwise sequential algorithm all input modes are set to provide no phase modulation and only the one being tested actually is active. In the continuous sequential algorithm each mode is optimized with the previously optimized modes already on their optimal modulation setting. In the partitioning algorithm, in each iteration a random set of half the input modes is chosen and they optimized. When the selected modes have finished optimizing, their computed best modulation value is displayed on the SLM, and another random set is chosen. This goes on for a certain number of iterations. Optimization graphs by Vellekoop and Mosk [30] show that regardless of the algorithm, each mode should be optimized more than once. This mostly has to do with two factors: using the stepwise or partition algorithms while the enhancement is still low makes for measurements very sensitive to noise; secondly, the conditions on which a mode was optimized can change (and do change) when another mode is then processed. One can think that phase shifting a given mode changes the condition where any other mode would have maximum constructive interference with the former.

5.2 Our implementation of optimization algorithms

Three different optimization scripts were developed in order to implement different target scenarios: one optimizes for a tight focus on the output plane, one that optimizes for multiple spots, and finally one that optimizes for a given arbitrary mask.

Optimizing for a single tight focus by maximizing the intensity at a given output mode (pixel) at the output plane is very susceptible to noise, and cripples the sensitivity of the system. So, our script optimizes for a given region around the selected camera pixel instead, typically a four by four square. The same happens for the multiple spot optimization algorithm: we optimize for a small area around each pixel instead. For the region optimization algorithm, the definition of the region of interest is set by a black and white image (*.png format), where white defines desires illumination area.

As already mentioned in section 4.2.4, focusing on a spot at the output plane very easily concentrates the light by an amount that exceeds the camera's dynamic range for a given value of exposure and gain settings. In all scripts, it is implemented a feature that keeps the intensity of light in the target area(s) under the limit where the camera sensor would overload. If this was not the case, in the worst case scenario, all pixels at a given optimization area would be overloaded, and it would become impossible to see any difference between different phase values for each optimized mode, breaking the algorithm. Attenuating the light before the process starts is not a viable option as having more light allows for better contrast, thus improving resistance to noise in the system.

The optimization method chosen was the continuous sequential algorithm, as it is easy to implement and very tolerant to noise after the first couple iterations.

As mentioned before now, the SLM is very slow to update its displayed frame in relation to the maximum possible acquisition rate of the camera. This makes testing the whole domain of possible input modes and phases practically impossible. So, as in the previous experiment, we use macro-pixels instead of single pixels as independent input modes. In this technique, the different input modes are used individually, as a canonical basis system. The number of independent macro-pixels is a configurable parameters of the system. Since testing the possible 256 different phases for each mode is also impossible in useful time, we also divide the $[0, \pi]$ phase domain in a configurable number of evenly spaced phase shifts to be tested. The number of times the algorithm runs through all input modes for a single optimization is also configurable.

Putting all of this together, we present a pseudocode that generally described the optimization process:

```
Import modules
Initialize SLM
Define camera parameters: exposure, gain, use automatic exposure adjustment, automatic exposure adjustment parameters ($maxpower@RoI$, $exposureStep$)
Define optimization parameters: optimization region size, number of modes ($nmodes$), number of phases per mode ($nphases$), number of passes ($npasses$)
Define RoI: Single spot, multiple spot, from *.png mask
Initialize camera
Set camera parameters
Generate variables: array of possible phases ($posphases$), optimization mask ($optMask$)
```

```
for pass in npasses do
    for mode in nmodes do
        for currphase in posphases do // current phase and possible phases
            Set mode's phase as currphase
            Update SLM display
            Acquire frame
            Compute SNR
            if current SNR $<$ old SNR then
                Revert mode's phase to previous phase
            end if
        end for
        Compute power@RoI
        if power@RoI $>$ maxpower@RoI then
            Decrease camera exposure by exposureStep
        end if
    end for
end for
Acquire result
Display result
Process result
```

5.3 Results

We present our results using this technique for focusing through a diffuse medium and and optical fibre. In the latter, we also did multiple spot focusing and optimizations for specific target shapes. We also present a characterization of the technique parameters.

5.3.1 Single spot optimization

In figure 5.1 we can see the intensity maps at the output plane, as recorded by the camera sensor. For these results, we used the diffuser already displayed in figure 4.4 (page 48). The optimizations were performed with 256 modes using 9 possible phase shifts per mode and a single pass per mode. The ratio between the intensity at the focus area and the average background intensity per same amount of area defines our figure of merit for the

SNR. The optimization time is about 5 minutes. In figure 5.2 we also demonstrate the ability to focus through fibre optics using this technique. The optimization was executed with the same parameters as used for the diffuser, and the final SNR after the optimization is of 14.8.

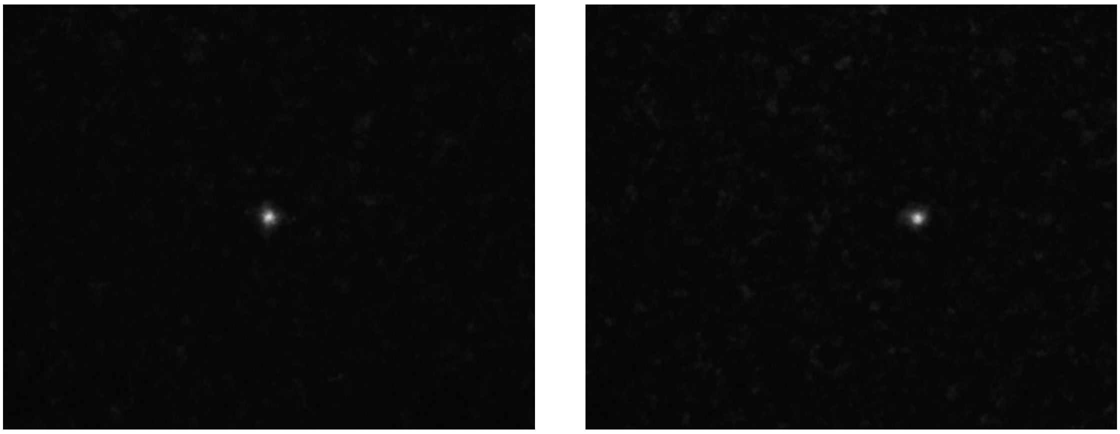

(A) Optimization at $x = 256$, $y = 320$.
SNR = 23.4

(B) Optimization at $x = 256$, $y = 400$.
SNR = 23.3

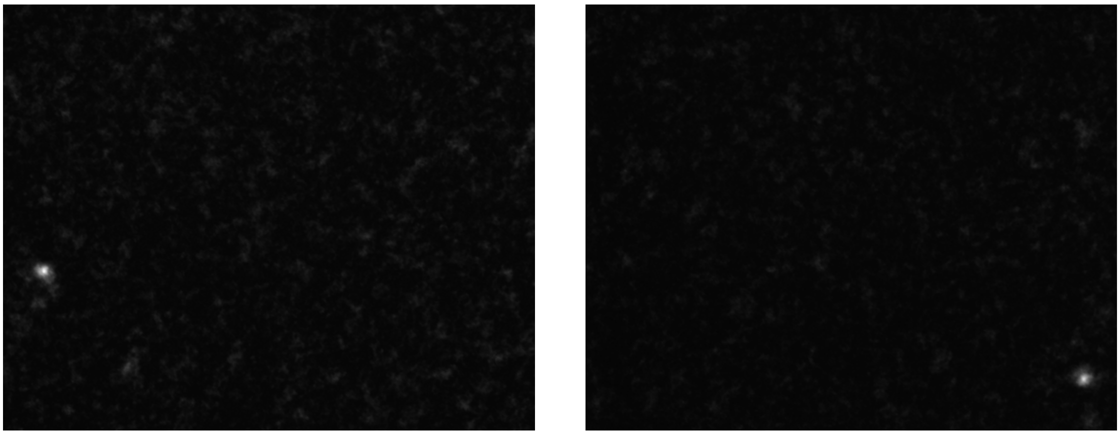

(C) Optimization at $x = 320$, $y = 50$.
SNR = 22.2

(D) Optimization at $x = 450$, $y = 600$.
SNR = 22.9

FIGURE 5.1: Single spot focusing at various places in the output plane. Spot coordinates are in pixel dimensions.

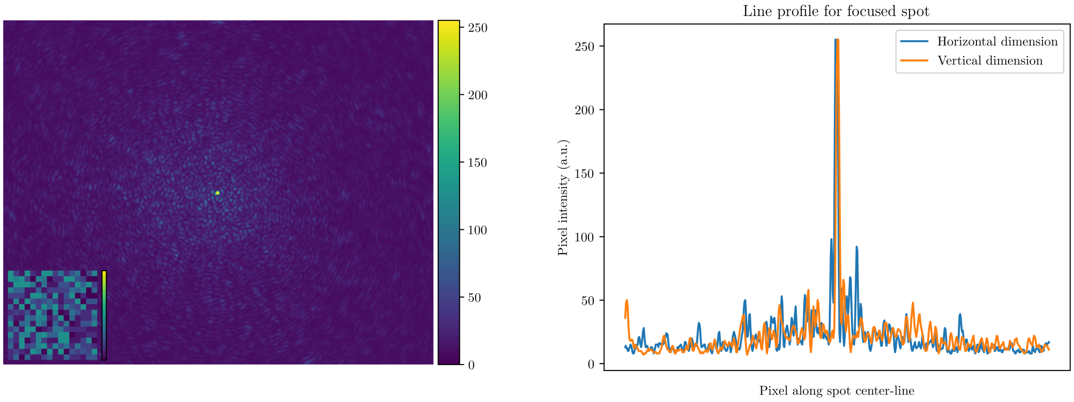

(A) Optimization result. The inset shows the optimized phase mask.

(B) Line profile on vertical and horizontal cuts through the plane at the focused spot.

FIGURE 5.2: Single spot focusing through fibre optics.

5.3.2 Multiple spot optimization

In figures 5.3 and 5.4 we demonstrate our ability to generate multiple focused spots at the output plane. We tested a four spot optimization in a “diamond” and in a “square” configurations. The complex media used in these demonstrations is a multimode optical fibre and, again, we used 256 modes, 9 possible phase shifts per mode and a single pass per mode. The SNR for the diamond shape is of 11.0 and 14.32 for the square shape.

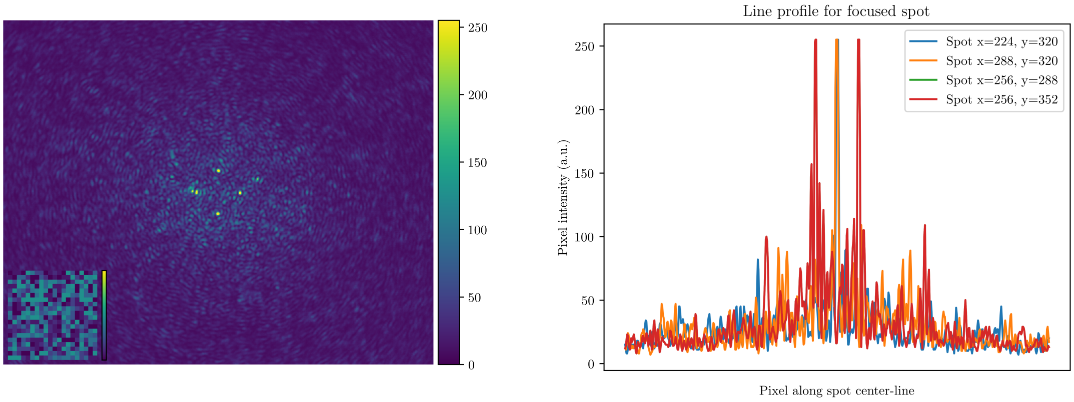

(A) Optimization result. The inset shows the optimized phase mask.

(B) Line profile on vertical and horizontal cuts through the plane at the focused spots.

FIGURE 5.3: Multiple spot focusing through fibre optics in a diamond fashion.

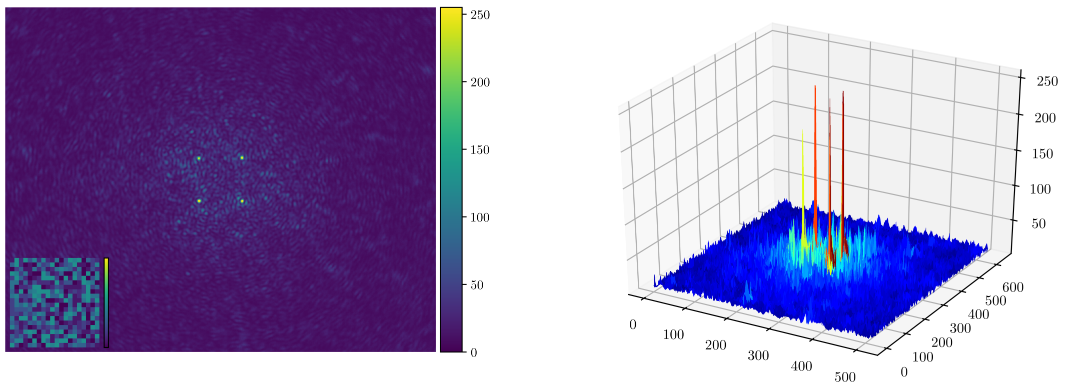

(A) Optimization result. The inset shows the optimized phase mask.

(B) *Wireframe* plot of the optimization result where the four spots can be seen.

FIGURE 5.4: Multiple spot focusing through fibre optics in a square fashion.

5.3.3 Target image optimization

We also demonstrate out ability to shape light into an arbitrary pattern. In figure 5.5 we can see light manipulated into an "I" beam shape, and in figure 5.6 we manipulate light into a "L" shape. The optimization conditions were the same as for the focusing multiple spots. The SNR for the "L" shape is of 4.3. As expected, controlling this high number of output modes with a fairly limited number of input modes reduces the achievable signal to noise ratio.

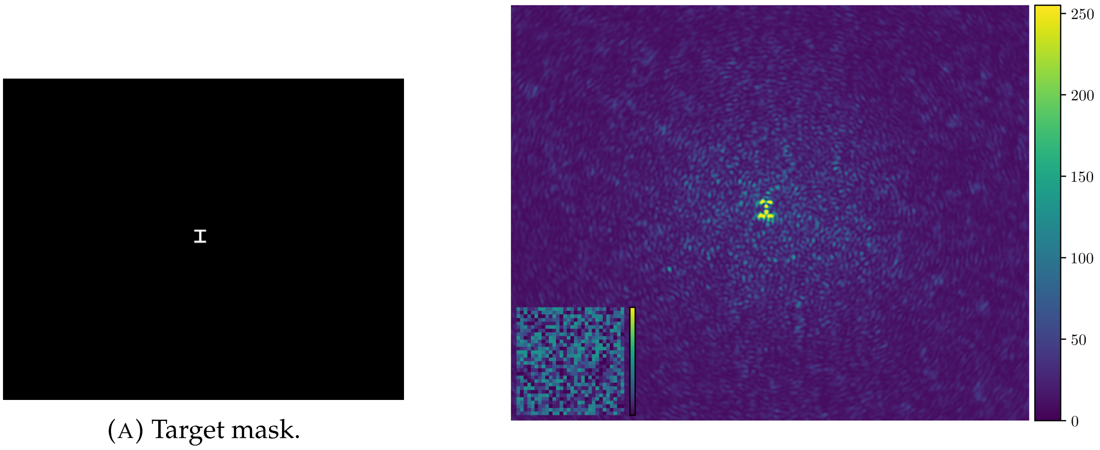

(A) Target mask.

(B) Optimization result. The inset reveals the optimized phase mask.

FIGURE 5.5: Result of optimizing for an "I" shape.

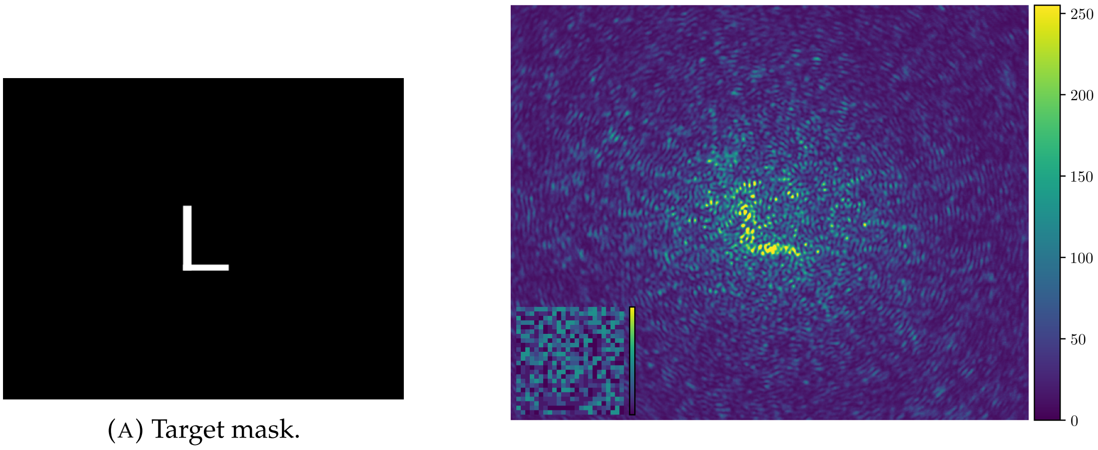

(A) Target mask.

(B) Optimization result. The inset reveals the optimized phase mask.

FIGURE 5.6: Result of optimizing for a "L" shape.

5.3.4 Study of optimization parameters

In this section, we present the study of the dependence of the optimization performance of its main parameters: number of input modes used, and number of possible phases per mode. The measurements were performed for a single focus point optimization at the centre of the camera.

5.3.4.1 Optimization response to the number of input modes

To keep consistency and possibility of comparison with the TM measurement based setup, we chose to only modulate a square region in the SLM area, limited by the input aperture of the lens used to couple the input modes to the complex medium. We used 480 pixels as length of the side of the optimization area. This number has to be an integer multiple of the square root of the number of input modes (macropixels) used for optimization because, as mentioned in section 4.2.1.1, the Kronecker's product method for scaling up the input phase array only allows for integer scale factors. 9 phases per mode were used during this experiment. In figure 5.7 we present how the SNR changes with the increase of input modes. We can see the achievable SNR increases with the number of modes optimized but with ever-diminishing returns, meaning that the same amount of increase in input modes produces a lesser improvement in the achievable SNR for a higher number of input modes. Fitting the points to a bounded exponential curve, we estimate the maximum achievable SNR being about 25. The fit parameter $\tau = 124.8$ gives us a hint of the number of modes needed for a given optimization: if we use $4\tau = 499.2$ (rounded

500) modes we should be able to achieve around 98% of the full SNR potential, meaning a value of 24.5. In figure 5.8 we see how the profile of an optimization for a single focused spot evolves as the number of modes increases: with only 16 modes we cannot say we achieved tight focusing, as other areas have similar intensities. As we increase the number of modes the noise surrounding the focused spot tends to lower and flatten, maximizing the SNR. Naturally, with an increase in the number of input modes, it takes more time to achieve optimization. In figure 5.9 we can confirm the intuitive linear dependence between the time to optimize the input phase mask and the number of modes used. Optimizing a single mode takes 1.1 second. Surprisingly, we see that we have a non-zero y-intercept. One would also expect that optimizing zero modes would take virtually no time, but we can observe an initial 4.93 seconds (y-intercept) delay. This value might be due to Python's processing overhead, like byte-code compilation and the generation of variable in memory. Figure 5.10 provides an interesting insight: do we benefit from taking more time to optimize regarding the SNR we achieve? The answer is clearly yes, as the curve of the time-to-SNR ratio goes on a down-slope with the increase of the number of independent input modes. However, we are again faced with a situation of ever-diminishing returns in increasing the number of modes being optimized: the same increase in the number of modes being optimized leads to a lesser increase in time-to-SNR ratio, as the number of modes optimized increases.

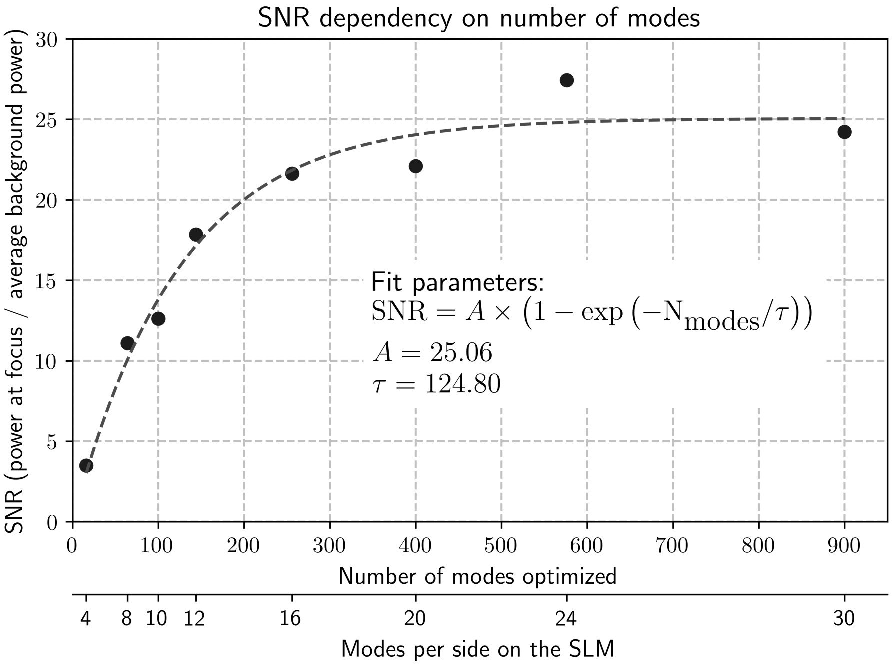

FIGURE 5.7: SNR evolution with the number of modes optimized.

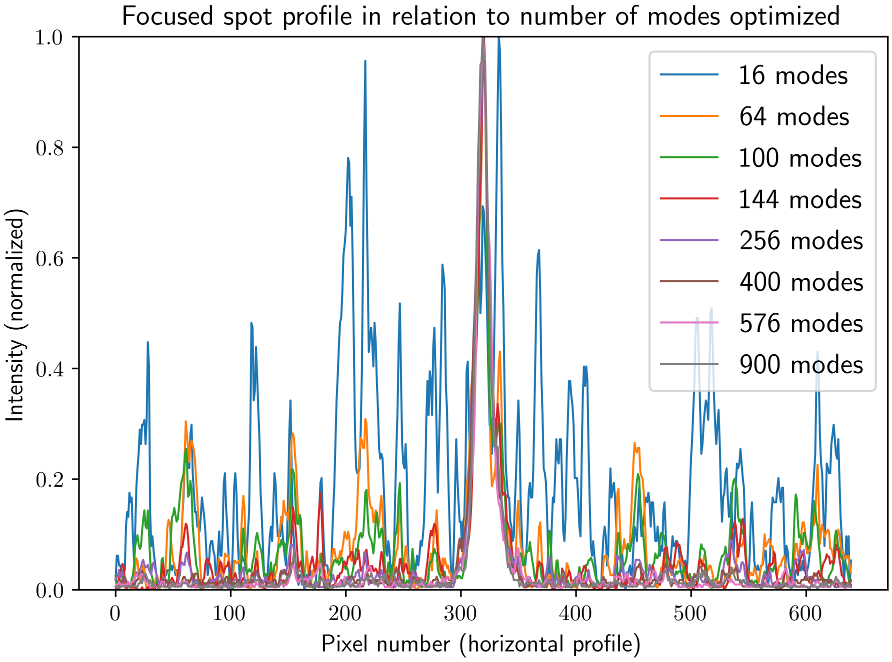

FIGURE 5.8: Line profile of a single focused spot for various number of modes optimized (normalized).

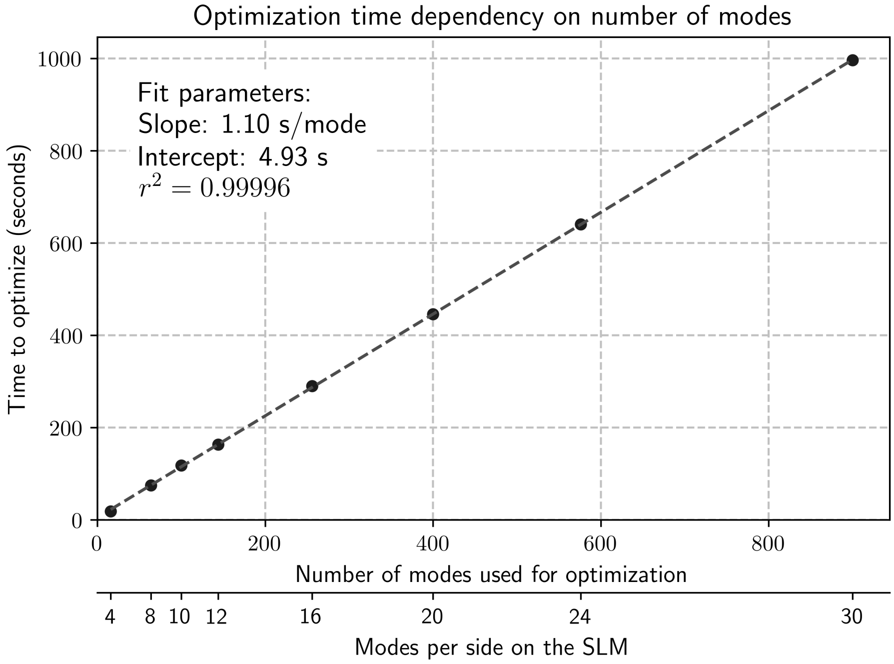

FIGURE 5.9: Time to optimize a given number of modes.

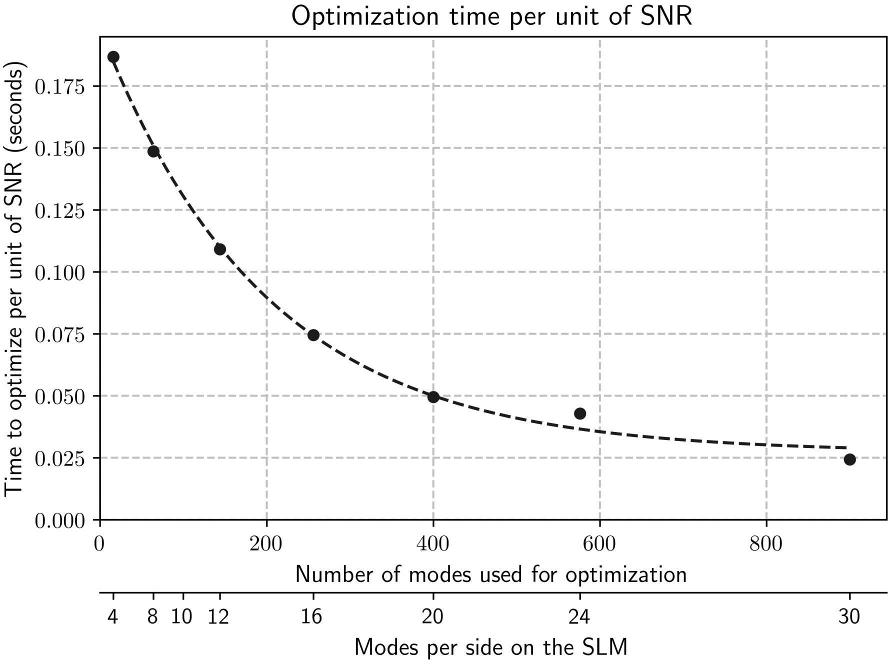

FIGURE 5.10: Cost/benefit relation with the number of modes optimized.

5.3.4.2 Optimization response to the number of phases per mode

In this test we used 256 modes, with one pass each and varied the number of possible phases for each mode. In figure 5.11 we can see that using a greater number of possible phases for the input modes results in an increase in SNR. However, as it can be seen in figure 5.12, this also means extra time to optimize. As with the study of the dependence of the algorithm in the number of modes used, we plot the ratio between the time needed to optimize the input phase mask and the achieved SNR for the tested number of possible phases for the input modes. This can be seen in figure 5.13, where we find that, for the higher number of possible phases tested, the ratio is almost constant. This means the gains in SNR go by the same amount as the penalty in time. This behaviour will not last forever as the maximum achievable SNR is finite and the resolution limits of the SLM would come into play. Furthermore, at almost 5 minutes, 9 phases per mode at 256 modes becomes the ceiling of what what is reasonable in practical applications. Finally, in figure 5.14 are displayed profile cuts of spots optimized using these different number of possible modes per phase. We can see that for 3 phases there is actually no light concentration in the centre region, which is the defined target. Using 9 possible phases per mode already provides a clear spot with a low noise floor.

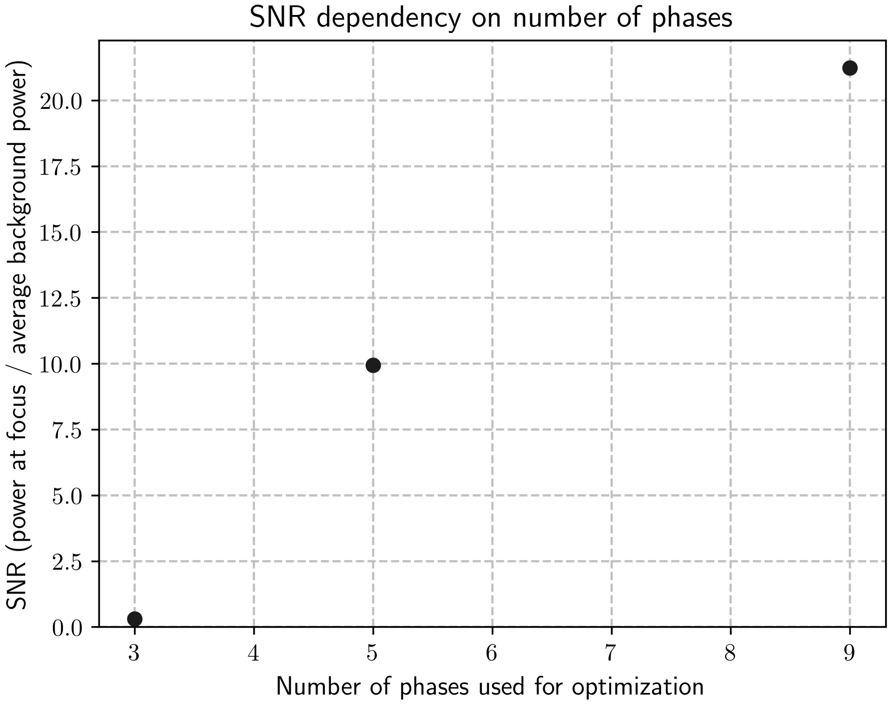

FIGURE 5.11: SNR evolution with the number of possible phases per mode.

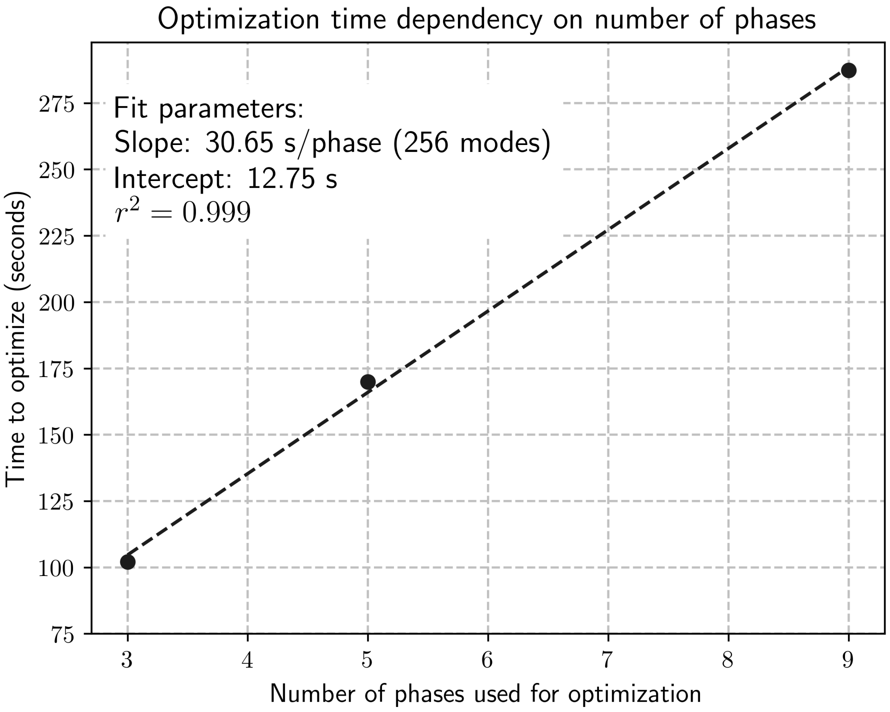

FIGURE 5.12: Time to optimize using given number of possible phases per mode.

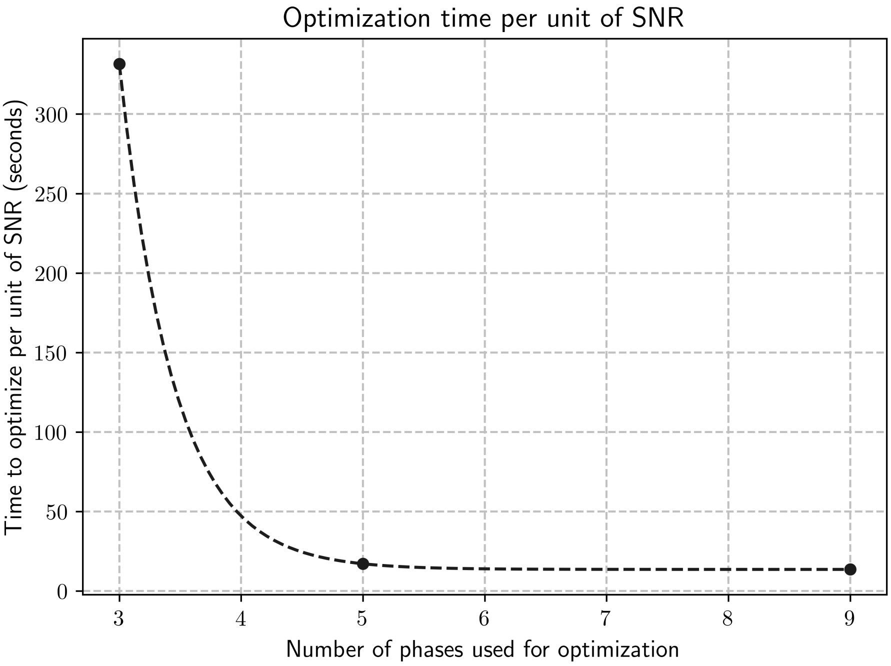

FIGURE 5.13: Cost/benefit relation with the number of modes optimized.

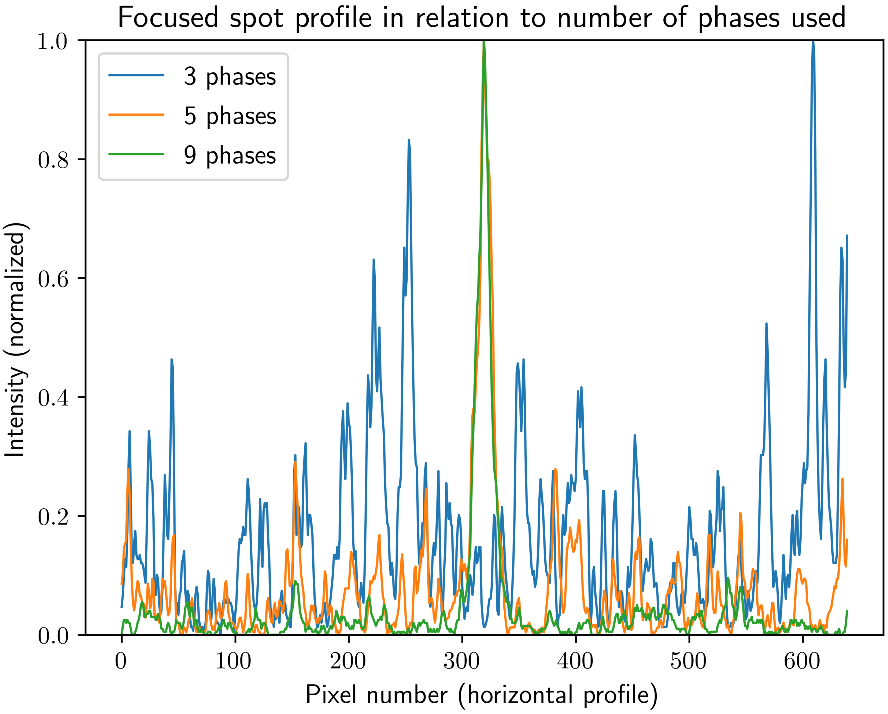

FIGURE 5.14: Line profile of a single focused spot for various number of possible phases per mode (normalized).

5.4 Discussion and conclusions

With this experiment, we achieved focusing through complex media, created multiple spot patterns and manipulated light to occupy an arbitrary region of space. The signal to noise ratio of the optimization process for focused spots is in par with the one obtained via the measurement of the transmission matrix. For comparison, using 256 input modes in both systems and nine possible phases for the optimization algorithm, for a single spot in the centre of the camera sensor, we achieved an SNR of 21.69 with the optimization algorithm and an SNR of 23.4 using the TM calibration scheme. However, while with the TM measurement scheme the next step of possible input modes, 1024, is a power of four away, meaning a 4-fold increase in optimization time, in the optimization algorithm we can increase the number of input modes to 576, achieving a SNR or 27.44 in these conditions, at the cost of doubling the optimization time. The time for a single optimization is comparable to the one it takes to calibrate the transmission matrix using the mentioned 256 input modes and nine possible phases per mode regarding the optimization algorithm.

While, in theory, the TM provides a single measurement for all the space at the same

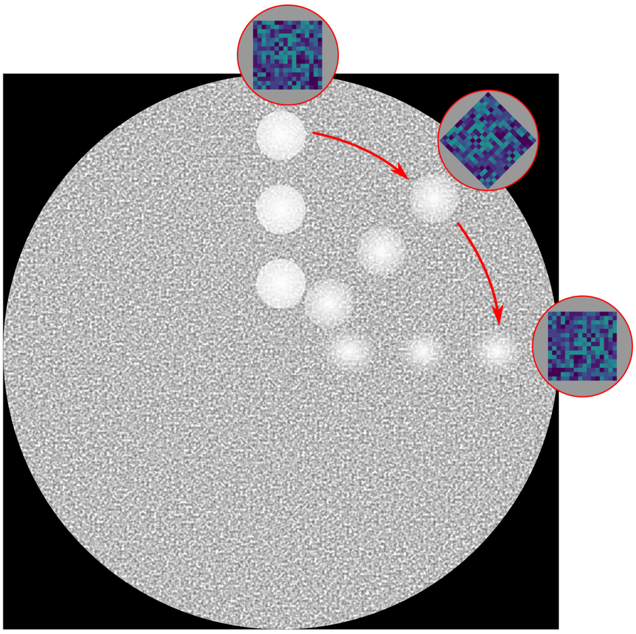

FIGURE 5.15: Use of the rotational memory effect to focus through fibre optics. If we optimize focused spots in one radial dimension we can move those focused spots by rotating the image displayed on the SLM. This assumes the centre of the image on the SLM is co-axial with the optical fibre.

time, the optimization algorithm requires a re-run for every different target pattern/position. In the case where an optical fibre is being used as complex medium of propagation, a clever solution, based on the so-called rotational memory effect, may be explored. The optical rotational memory effect means that if the input field entering the fibre is rotated by some amount in relation to the fibre axis, the output rotates by the same amount, as long as the angle is in the limit of the so-called rotational memory effect range. This effect has been demonstrated and measured by Amitonova et al. [42]. Exploiting this effect, we can calibrate focused spots in the radial axis of the fibre, separated angularly by twice the rotational memory effect range, and just rotate the input to fill out the rest. This would allow for an interesting imaging and/or optical manipulation system (optical tweezers). The trade-off is a relatively small loss of quality of the focus. Figure 5.15 is explicative of this effect.

As with the TM experiment, the system suffers from the fact that the medium has to be perfectly static during the optimization process. This comes mainly from the fact that, by using the SLM as source of phase modulation, any optimization takes longer than the characteristic times of any dynamic media. A solution proposed Caravaca-Aguirre et al. [31] suggests the use of a DMD and Lee Holography. Using a custom firmware on the

FPGA of the DMD, they manage to exploit the high speed characteristics of the DMD to provide a dynamic re-focusing system.

It becomes clear that the transitioning from the SLM to the DMD using Lee holography, or even directly, is the next logical step regarding work in light manipulation through complex media. A combination of the exploitation of the memory effect and fast light control using a DMD is a promising path that clearly must be explored.

Chapter 6

Concluding remarks

Light manipulation and object imaging through complex media is a new subject at INESC-TEC's Centre for Applied Photonics (CAP). That being, it was important to establish a solid base of knowledge in the theory and techniques commonly employed in this topic. We successfully implemented three different techniques: imaging through diffuse media using the shower curtain effect, measuring the transmission matrix of a complex medium, and finally, manipulating light through complex media via optimization algorithms.

These techniques require speciality hardware and more-or-less complicated chains of digital signal processing. In chapter 2, we discussed the hardware and software we used, including a spatial light modulator from Holoeye, a CMOS camera from Ximea, and a digital micro-mirror device from Vialux. To code our software, we used the Python language with its scientific and numeric libraries. The scripts were developed as Jupyter notebooks as the notebook paradigm offers flexibility in executing the scripts.

Regarding the experiments performed, we started by discussing our take on the shower curtain effect imaging technique on chapter 3. We managed to retrieve objects that were illuminated with speckle light and placed behind diffuse media, and managed to retrieve information about a microscopic object without the use of an objective lens. We learned that the far-field condition for the diffraction of an object illuminated with a speckle pattern is dramatically reduced when comparing with a full coherent illumination. We also acquired a thorough understanding of phase retrieval algorithms, which might become useful for other techniques. N'Gom et al. [28] actually developed a system to measure the transmission matrix using phase retrieval techniques, showcasing the wide range of application of this family of algorithms. For the future, the exploration of these phase retrieval algorithms is of the uttermost importance. In them, it may lay the key to interesting answers in the quest for diffuse media imaging techniques.

In chapter 4 one can find our report on measuring the transmission matrix without a reference arm. Here, we managed to focus light through a diffuse medium and through an optical fibre. We consolidated the knowledge for a model on how light propagates through these media. The development of this technique got us comfortable with the use of the spatial light modulator and the use of Hadamard matrices as source for an input modes basis. However, there is still much to do. The biggest problem with our setup is the time it takes to measure the TM. To try and solve this, we experimented with a digital micro-mirror device as source of phase modulation using Lee holography. At the time of writing, we did not manage to get useful results with this scheme. This is an absolute must for the work in the near future. The use of the DMD allows for a dramatical increase in the speed at which data can be acquired, also allowing for larger wave basis to be used.

The third experiment we developed has to do with optimization algorithms as a way to manipulate light through complex media and it is discussed in chapter 5. We managed to focus light through a diffuser and through an optical fibre. We also managed to generate multiple focused spots and even arbitrary patterns. The signal to background noise ratio was comparable to the one achieved by measuring the TM. The optimization time, and the fact it has to be re-run every time we wish to change the position of a focused spot or the position/shape of any arbitrary pattern are the two main disadvantages of this technique. Again, this is where the use of a DMD would dramatically help things. It is clear by now that this piece of equipment should be studied as a tool in the field of diffuse media manipulation. As mentioned in section 2.1.1, we actually did experiment with the DMD, even though we have not achieved any definitive result at the time of writing. In appendix A, we describe the technical knowledge acquired and what we have done regarding the use of the DMD.

In the future, we suggest the use of these two last techniques as imaging techniques or that their light manipulation ability is used for practical purposes like optical tweezers. CAP/INESC-TEC has a solid background in optical tweezers and integrated optics where the techniques studied in this work may be used. Optical trapping via multimode waveguides in integrated optics or single multimode-fibre trapping and imaging are two open paths left for exploration.

With this work the research group at CAP/INESC-TEC is now ready to take on more advanced challenges in the subjects of light manipulation and optical imaging through complex media.

Appendix A

Experiments with the DMD

Even though the digital micromirror device described in section 2.1.1.2 was not used for any final experiments, there was an effort to understand its working mechanism, API and hardware interfacing, which are described in this appendix.

A.1 Interfacing with the device

A.1.1 The software

The Vialux DLP V-7000 comes with an API written in the C language. Popoff [59] wrote a wrapper for the Python language, which we used. It implements all the functionality the C library provides, except for the board LEDs controls, which are not necessary for this project anyway. The work flow when using the DMD goes as follows:

1. Import modules
2. Create DMD object
3. Initialize DMD
4. Allocate memory for the display data
5. Upload display data
6. Set framerate and timing parameters
7. Run job
8. Acquire data
9. Stop job
10. Free memory
11. Release DMD

A.1.2 Timing parameters

There are two timing parameters: picture time and illuminate time. The first defines the frame duration while the second defines the period where the frame in memory is actually being displayed. Therefore, illuminate time can only be smaller or equal to picture time. If it is indeed smaller, the difference is called the “dark phase” and it’s split evenly between the beginning and ending of the picture time. Figure A.1 provides a visual explanation of these timing settings. In our work, we aimed for no dark times, so picture time was always set the same as illuminate time.

FIGURE A.1: Vialux DLP V-7000’s timing settings [77].

A.1.3 Synchronizing the display and the acquisition

The Vialux DLP V-7000 does not provide any means of software trigger. This means that the frame change is not controllable by the user in software once a display job is running. So any triggering must be done via hardware. We had many options for this. An external trigger could be added using, for example, the National Instruments DAQ family of devices. This solution is not desirable as it adds another rather expensive piece of hardware into the setup. The solution is in the use of built-in trigger solutions present in both Ximea’s “XiQ” family of cameras and on the DMD itself. Both devices support being master or slave devices regarding triggering. A custom cable to interface the camera’s GPIO plug (Hirose Connector, HRS SR38-4P-3P) and the DMD’s multi-purpose connector (Molex header, part number 53261-1071, with crimp contacts 50058-8000) was built in house to accommodate this. The DMD’s trigger behaviour in both master and slave modes is pictured in figure A.2. Since it makes sense that the camera only starts acquiring after the DMD has finished changing frame, the camera was chosen to be the slave device and the DMD as master device. Therefore, the general purpose input pin on the camera is set, via a command in the scripts were this scheme is used, to work as trigger input, responsive to rising edge.

(A) Master mode.

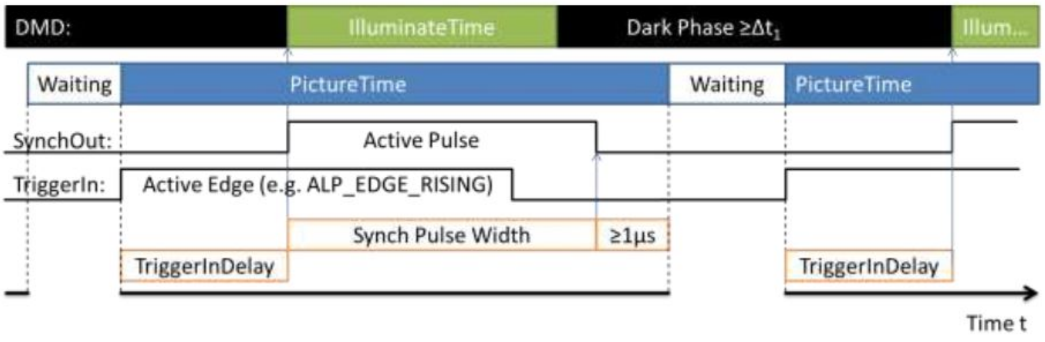

(B) Slave mode.

FIGURE A.2: DMD's trigger behaviour when is master or slave modes [77].

A.2 Work done with the DMD

The experiment regarding calibrating the transmission matrix of a complex optical medium was ported into the DMD. Time constraints did not allow for proper experimentation and debugging. Using the DMD as source of phase modulation is a challenge as its performance is dependent on various parameters, plus a proper optical setup. This makes debugging a challenge.

At the time of writing, it was already developed a function that generates the gratings used for phase modulation using Lee holography from arbitrary phase masks, as described in section 2.1.1.2. The function takes all the parameters as variables making it easier to do an experimental search for optimal parameters. A Jupyter notebook responsible to generate the frames to be used on the DMD for the three and four phases method, using the aforementioned function, was also fully developed at the time of writing, as well as an acquisition script using the described triggering scheme. The data processing script is common to both this scheme and with the use of the SLM. The final script we developed to provide validation of the measured transmission matrix by generating a focused spot was also ported for use with the DMD, although the version used for the SLM suffered revisions since the idea of using a DMD was abandoned, so this needs revision.

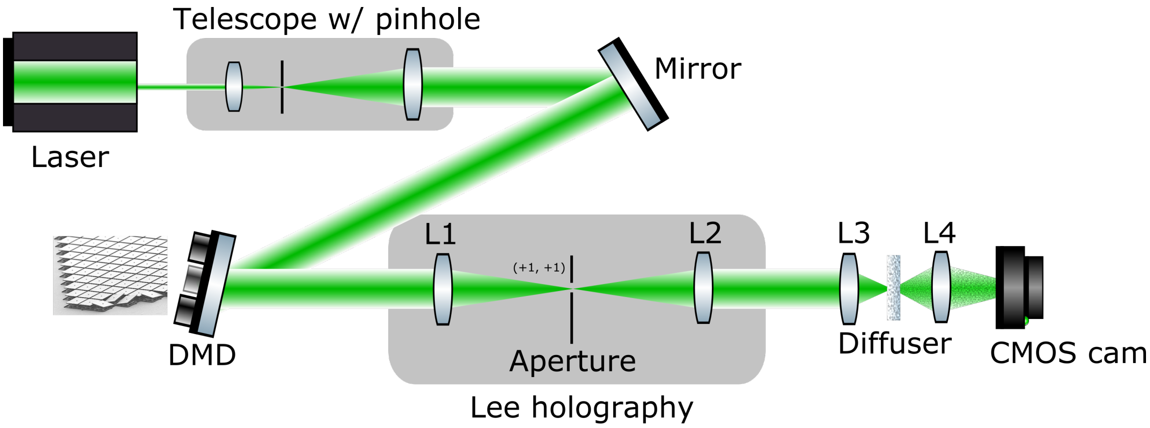

FIGURE A.3: Optical setup to use the DMD as source of spatial phase modulation for use in light manipulation through complex media.

We assembled an optical setup to accompany the code developed, which is an adaptation of the one described in figure 4.4. This setup is presented in figure A.3. The use of the mirror to skew the beam and having the DMD tilted is to compensate the 12.5 degree angle the micromirrors make with the DMD plane when in the "on" state. This generates a horizontal beam at the output, parallel with the original laser beam.

Bibliography

[1] G. Sines and Y. Sakellarakis, "Lenses in antiquity," *American Journal of Archaeology*, vol. 91, no. 2, pp. 191–196, apr 1987. [Online]. Available: https://www.jstor.org/stable/505216?origin=crossrefhttp://www.jstor.org/stable/505216

[2] P. the Elder and H. H. Rackham, *Natural history*. Cambridge Mass.: Harvard University Press, 1938. [Online]. Available: http://www.worldcat.org/title/natural-history/oclc/313293

[3] S. Andersson-Engels, O. Jarlman, R. Berg, and S. Svanberg, "Time-resolved transillumination for medical diagnostics," *Optics Letters*, vol. 15, no. 21, p. 1179, nov 1990. [Online]. Available: https://www.osapublishing.org/abstract.cfm?URI=ol-15-21-1179

[4] E. Leith, H. Chen, Y. Chen, D. Dilworth, J. Lopez, R. Masri, J. Rudd, and J. Valdmanis, "Electronic holography and speckle methods for imaging through tissue using femtosecond gated pulses," *Applied Optics*, vol. 30, no. 29, p. 4204, oct 1991. [Online]. Available: https://www.osapublishing.org/abstract.cfm?URI=ao-30-29-4204

[5] B. B. Das, K. M. Yoo, and R. R. Alfano, "Ultrafast time-gated imaging in thick tissues: a step toward optical mammography," *Optics Letters*, vol. 18, no. 13, p. 1092, jul 1993. [Online]. Available: https://www.osapublishing.org/abstract.cfm?URI=ol-18-13-1092

[6] H. Ramachandran and A. Narayanan, "Two-dimensional imaging through turbid media using a continuous wave light source," *Optics Communications*, vol. 154, no. 5-6, pp. 255–260, 1998.

[7] H. Horinaka, K. Hashimoto, K. Wada, Y. Cho, and M. Osawa, "Extraction of quasi-straightforward-propagating photons from diffused light transmitting through a scattering medium by polarization modulation." *Optics letters*, vol. 20, no. 13, pp. 1501–3, jul 1995. [Online]. Available: http://www.ncbi.nlm.nih.gov/pubmed/19862062https://www.osapublishing.org/ol/viewmedia.cfm?uri=ol-20-13-1501&seq=0

[8] S. G. Demos and R. R. Alfano, "Temporal gating in highly scattering media by the degree of optical polarization," *Optics Letters*, vol. 21, no. 2, p. 161, jan 1996. [Online]. Available: https://www.osapublishing.org/abstract.cfm?URI=ol-21-2-161

[9] ——, "Optical polarization imaging," *Applied Optics*, vol. 36, no. 1, p. 150, jan 1997. [Online]. Available: https://www.osapublishing.org/abstract.cfm?URI=ao-36-1-150

[10] O. Emile, F. Bretenaker, a. L. Floch, A. Le Floch, a. L. Floch, and A. Le Floch, "Rotating polarization imaging in turbid media." *Optics letters*, vol. 21, no. 20, pp. 1706–1708, oct 1996. [Online]. Available: https://www.osapublishing.org/abstract.cfm?URI=ol-21-20-1706

[11] S. Mujumdar and H. Ramachandran, "Imaging through turbid media using polarization modulation: Dependence on scattering anisotropy," *Optics Communications*, vol. 241, no. 1-3, pp. 1–9, 2004.

[12] Y. Choi, T. D. Yang, C. Fang-Yen, P. Kang, K. J. Lee, R. R. Dasari, M. S. Feld, and W. Choi, "Overcoming the diffraction limit using multiple light scattering in a highly disordered medium," *Physical Review Letters*, vol. 107, no. 2, pp. 1–4, 2011.

[13] Y. Choi, C. Yoon, M. Kim, T. D. Yang, C. Fang-Yen, R. R. Dasari, K. J. Lee, and W. Choi, "Scanner-free and wide-field endoscopic imaging by using a single multimode optical fiber," *Physical Review Letters*, vol. 109, no. 20, pp. 1–5, 2012. [Online]. Available: http://www.scopus.com/inward/record.url?eid=2-s2.0-84869069707&partnerID=40&md5=3bfebe1e907a03f7fffd765c26d8c0e4

[14] H. Jang, C. Yoon, E. Chung, W. Choi, and H.-N. Lee, "Holistic random encoding for imaging through multimode fibers," *Optics Express*, vol. 23, no. 5, p. 6705, 2015. [Online]. Available: https://www.osapublishing.org/abstract.cfm?URI=oe-23-5-6705

[15] S. Li and J. Zhong, "Dynamic imaging through turbid media based on digital holography," *Journal of the Optical Society of America A*, vol. 31, no. 3, p. 480, 2014. [Online]. Available: https://www.osapublishing.org/abstract.cfm?URI=josaa-31-3-480

[16] I. N. Papadopoulos, S. Farahi, C. Moser, and D. Psaltis, "Focusing and scanning light through a multimode optical fiber using digital phase conjugation," *Optics Express*, vol. 20, no. 10, p. 10583, 2012. [Online]. Available: https://www.osapublishing.org/abstract.cfm?URI=oe-20-10-10583

[17] ——, "Increasing the imaging capabilities of multimode fibers by exploiting the properties of highly scattering media." *Optics letters*, vol. 38, no. 15, pp. 2776–8, 2013. [Online]. Available: http://www.ncbi.nlm.nih.gov/pubmed/23903139

[18] T. Čižmár and K. Dholakia, "Shaping the light transmission through a multimode optical fibre: complex transformation analysis and applications in biophotonics," *Optics Express*, vol. 19, no. 20, p. 18871, 2011. [Online]. Available: https://www.osapublishing.org/abstract.cfm?URI=oe-19-20-18871

[19] ——, "Exploiting multimode waveguides for pure fibre-based imaging," *Nature Communications*, vol. 3, no. May, 2012.

[20] S. Farahi, D. Ziegler, I. N. Papadopoulos, D. Psaltis, and C. Moser, "Dynamic bending compensation while focusing through a multimode fiber," *Optics Express*, vol. 21, no. 19, p. 22504, sep 2013. [Online]. Available: https://www.osapublishing.org/abstract.cfm?URI=oe-21-19-22504

[21] M. Kim, W. W. Choi, Y. Choi, C. Yoon, and W. W. Choi, "Transmission matrix of a scattering medium and its applications in biophotonics," *Optics Express*, vol. 23, no. 10, p. 12648, may 2015. [Online]. Available: https://www.osapublishing.org/abstract.cfm?URI=oe-23-10-12648

[22] S. Gigan, "Endoscopy Slims Down," *Physics*, vol. 5, p. 127, 2012. [Online]. Available: https://link.aps.org/doi/10.1103/Physics.5.127

[23] S. M. Popoff, G. Lerosey, R. Carminati, M. Fink, A. C. Boccara, and S. Gigan, "Measuring the Transmission Matrix in Optics: An Approach to the Study and Control of Light Propagation in Disordered Media," *Physical*

Review Letters, vol. 104, no. 10, p. 100601, mar 2010. [Online]. Available: https://link.aps.org/doi/10.1103/PhysRevLett.104.100601

[24] D. B. Conkey, A. M. Caravaca-Aguirre, and R. Piestun, "High-speed scattering medium characterization with application to focusing light through turbid media," *Optics Express*, vol. 20, no. 2, p. 1733, jan 2012. [Online]. Available: https://www.osapublishing.org/abstract.cfm?URI=oe-20-2-1733

[25] A. M. Caravaca-Aguirre and R. Piestun, "Single multimode fiber endoscope," *Optics Express*, vol. 25, no. 3, p. 1656, feb 2017. [Online]. Available: https://www.osapublishing.org/abstract.cfm?URI=oe-25-3-1656

[26] X. Tao, D. Bodington, M. Reinig, and J. Kubby, "High-speed scanning interferometric focusing by fast measurement of binary transmission matrix for channel demixing," *Optics Express*, vol. 23, no. 11, p. 14168, jun 2015. [Online]. Available: https://www.osapublishing.org/abstract.cfm?URI=oe-23-11-14168

[27] A. Dremeau, A. Liutkus, D. Martina, O. Katz, C. Schulke, F. Krzakala, S. Gigan, and L. Daudet, "Reference-less measurement of the transmission matrix of a highly scattering material using a DMD and phase retrieval techniques," *Optics Express*, vol. 10583, feb 2015. [Online]. Available: http://arxiv.org/abs/1502.03324%0Ahttp://dx.doi.org/10.1364/OE.23.011898https://www.osapublishing.org/oe/abstract.cfm?uri=oe-23-9-11898https://doi.org/10.1364/OE.23.011898

[28] M. N'Gom, T. B. Norris, E. Michielssen, R. R. Nadakuditi, M. N'Gom, T. B. Norris, E. Michielssen, and R. R. Nadakuditi, "Mode Control in a Multimode Fiber Through Acquiring its Transmission Matrix from a Reference-less Optical System," *Optics Letters*, vol. 43, no. 3, pp. 1–7, feb 2018. [Online]. Available: https://www.osapublishing.org/abstract.cfm?URI=ol-43-3-419http://arxiv.org/abs/1707.02634%0Ahttp://dx.doi.org/10.1364/OL.43.000419https://doi.org/10.1364/OL.43.000419

[29] I. M. Vellekoop and A. P. Mosk, "Focusing coherent light through opaque strongly scattering media," *Optics Letters*, vol. 32, no. 16, p. 2309, 2007. [Online]. Available: https://www.osapublishing.org/abstract.cfm?URI=ol-32-16-2309

[30] ——, "Phase control algorithms for focusing light through turbid media," *Optics Communications*, vol. 281, no. 11, pp. 3071–3080, 2008.

[31] A. M. Caravaca-Aguirre, E. Niv, D. B. Conkey, and R. Piestun, "Real-time resilient focusing through a bending multimode fiber," *Optics Express*, vol. 21, no. 10, p. 12881, 2013. [Online]. Available: https://www.osapublishing.org/abstract.cfm?URI=oe-21-10-12881

[32] D. Akbulut, T. J. Huisman, E. G. van Putten, W. L. Vos, and A. P. Mosk, "Focusing light through random photonic media by binary amplitude modulation," *Optics Express*, vol. 19, no. 5, feb 2011. [Online]. Available: https://www.osapublishing.org/oe/abstract.cfm?uri=oe-19-5-4017http://www.ncbi.nlm.nih.gov/pubmed/21369229

[33] G. Tremblay, R. Bernier, and G. Roy, "The shower curtain effect paradoxes," *Proc. SPIE*, vol. 9641, p. 964107, 2015. [Online]. Available: http://proceedings.spiedigitallibrary.org/proceeding.aspx?doi=10.1117/12.2194837

[34] E. Edrei and G. Scarcelli, "Optical imaging through dynamic turbid media using the Fourier-domain shower-curtain effect," *Optica*, vol. 3, no. 1, p. 71, 2016. [Online]. Available: https://www.osapublishing.org/abstract.cfm?URI=optica-3-1-71

[35] ——, "Optical imaging through dynamic turbid media using the Fourier - domain shower - curtain effect : supplementary material," *Optica*, vol. 3, no. 1, 2016.

[36] G. Osnabrugge, R. Horstmeyer, I. N. Papadopoulos, B. Judkewitz, and I. M. Vellekoop, "Generalized optical memory effect," *Optica*, vol. 4, no. 8, p. 886, 2017. [Online]. Available: https://www.osapublishing.org/abstract.cfm?URI=optica-4-8-886

[37] J. Bertolotti, E. G. Van Putten, C. Blum, A. Lagendijk, W. L. Vos, and A. P. Mosk, "Non-invasive imaging through opaque scattering layers," *Nature*, vol. 491, no. 7423, pp. 232–234, 2012. [Online]. Available: http://dx.doi.org/10.1038/nature11578

[38] X. Yang, Y. Pu, and D. Psaltis, "Imaging blood cells through scattering biological tissue using speckle scanning microscopy," *Optics Express*, vol. 22, no. 3, p. 3405, 2014. [Online]. Available: https://www.osapublishing.org/oe/abstract.cfm?uri=oe-22-3-3405

[39] J. R. Fienup, "Phase retrieval algorithms: a comparison," *Applied Optics*, vol. 21, no. 15, p. 2758, 1982. [Online]. Available: https://www.osapublishing.org/abstract.cfm?URI=ao-21-15-2758

[40] ——, "Phase retrieval algorithms: a personal tour [Invited]," *Applied Optics*, vol. 52, no. 1, p. 45, 2013. [Online]. Available: https://www.osapublishing.org/abstract.cfm?URI=ao-52-1-45

[41] ——, "Lensless coherent imaging by phase retrieval with an illumination pattern constraint," *Optics Express*, vol. 14, no. 2, p. 498, 2006. [Online]. Available: https://www.osapublishing.org/oe/abstract.cfm?uri=oe-14-2-498

[42] L. V. Amitonova, A. P. Mosk, and P. W. H. Pinkse, "Rotational memory effect of a multimode fiber," *Optics Express*, vol. 23, no. 16, p. 20569, 2015. [Online]. Available: https://www.osapublishing.org/abstract.cfm?URI=oe-23-16-20569

[43] N. Stasio, C. Moser, and D. Psaltis, "Calibration-free imaging through a multicore fiber using speckle scanning microscopy," *Optics Letters*, vol. 41, no. 13, p. 3078, 2016. [Online]. Available: https://www.osapublishing.org/abstract.cfm?URI=ol-41-13-3078

[44] N. Stasio, D. B. Conkey, C. Moser, and D. Psaltis, "Light control in a multicore fiber using the memory effect," *Optics Express*, vol. 23, no. 23, p. 30532, 2015. [Online]. Available: https://www.osapublishing.org/abstract.cfm?URI=oe-23-23-30532

[45] A. K. Singh, D. N. Naik, G. Pedrini, M. Takeda, and W. Osten, "Looking through a diffuser and around an opaque surface: A holographic approach," *Optics Express*, vol. 22, no. 7, p. 7694, 2014. [Online]. Available: https://www.osapublishing.org/oe/abstract.cfm?uri=oe-22-7-7694

[46] J. C. Dainty, *Laser Speckle and Related Phenomena*. Springer-Verlag, 1975, vol. 9. [Online]. Available: http://link.springer.com/10.1007/BFb0111434

[47] HOLOEYE Photonics AG, "PLUTO-2 Phase Only Spatial Light Modulator (Reflective) – Product page," 2018. [Online]. Available: https://holoeye.com/spatial-light-modulators/slm-pluto-phase-only/

[48] ViALUX GmbH, "V-7000 Hi-Speed DMD Specification - Product page," 2018. [Online]. Available: https://www.vialux.de/en/hi-speed-specification.html

[49] W.-H. Lee, "III Computer-Generated Holograms: Techniques and Applications," in *Progress in Optics*. Elsevier, jan 1978, vol. 16, pp. 119–232. [Online]. Available: https://www.sciencedirect.com/science/article/pii/S0079663808700726?via%3Dihub

[50] Sébastien Popoff, "How to use a binary amplitude Deformable Miror Device (DMD) as a phase modulator: Lee hologram method," 2018. [Online]. Available: http://wavefrontshaping.net/index.php/top/57-community/tutorials/spatial-lights-modulators-slms/70-how-to-get-amplitude-and-phase-modulation-using-a-binary-amplitude-deformable-miror-device-dmd

[51] XIMEA, "XIMEA - MQ013MG-ON - Product page," 2018. [Online]. Available: https://www.ximea.com/en/products/usb3-vision-cameras-xiq-line/mq013mg-on

[52] ——, "XiApi Manual - APIs - ximea support (webpage)," 2018. [Online]. Available: https://www.ximea.com/support/wiki/apis/XiAPI_Manual

[53] Python Fundation, "Welcome to Python.org (webpage)," 2018. [Online]. Available: https://www.python.org/

[54] Anaconda.org, "Python :: Anaconda Cloud (webpage)," 2018. [Online]. Available: https://anaconda.org/anaconda/python

[55] NumPy, "NumPy — Webpage," 2018. [Online]. Available: http://www.numpy.org/

[56] Matplotlib, "Matplotlib: Python plotting — Matplotlib 2.2.2 documentation (webpage)," 2018. [Online]. Available: https://matplotlib.org/

[57] Pyzo, "Python vs Matlab — Pyzo - Python to the people (webpage)," 2018. [Online]. Available: http://www.pyzo.org/python_vs_matlab.html

[58] Project Jupyter, "Project Jupyter (webpage)," 2018. [Online]. Available: http://jupyter.org/

[59] S. M. Popoff, "ALP4lib: A Python module to control Vialux DMDs," oct 2016. [Online]. Available: https://zenodo.org/record/1160714#.WuMVEcIh2Ukhttps://zenodo.org/record/1160714

[60] E. W. Weisstein, "Cross-Correlation Theorem," 1999. [Online]. Available: http://mathworld.wolfram.com/Cross-CorrelationTheorem.html

[61] ——, "Wiener-Khinchin Theorem," 1999. [Online]. Available: http://mathworld.wolfram.com/Wiener-KhinchinTheorem.html

[62] Y. Kuga and A. Ishimaru, "Modulation transfer function of layered inhomogeneous random media using the small-angle approximation," *Applied Optics*, vol. 25, no. 3, pp. 1–4, dec 1986. [Online]. Available: https://www.osapublishing.org/abstract.cfm?URI=ao-25-23-4382

[63] I. Dror, A. Sandrov, and N. S. Kopeika, "Experimental investigation of the influence of the relative position of the scattering layer on image quality: the shower curtain effect," *Applied Optics*, vol. 37, no. 27, p. 6495, sep 1998. [Online]. Available: https://www.osapublishing.org/abstract.cfm?URI=ao-37-27-6495

[64] J. W. Goodman, *Statistical optics*. New York: Wiley, 2000. [Online]. Available: http://www.worldcat.org/title/statistical-optics/oclc/45223800

[65] E. Wolf, *Introduction to the theory of coherence and polarization of light*. Cambridge: Cambridge University Press, 2007. [Online]. Available: http://www.worldcat.org/title/introduction-to-the-theory-of-coherence-and-polarization-of-light/oclc/149011826

[66] P. scientific, "High Precision Diffraction Slits, OS-8453 (manual)," 2012. [Online]. Available: https://www.pasco.com/file_downloads/Downloads_Manuals/Precision-Diffraction-Slits-Manual-OS-8453.pdf

[67] S. Suritasirikun, S. T. Khlaynoonme, and W. Thowladda, "Phase-shifting interferometry for surface roughness measurement on glass substrates," *Advanced Material Researchs*, vol. 974, no. July 2015, pp. 463–466, 2014.

[68] J. M. Park, W. J. Song, and W. a. Pearlman, "Speckle filtering of SAR images based on adaptive windowing," *IEE Proceedings - Vision, Image, and Signal Processing*, vol. 146, no. 4, p. 191, 1999. [Online]. Available: http://link.aip.org/link/IVIPEK/v146/i4/p191/s1&Agg=doi

[69] A. Dubois, "Phase-map measurements by interferometry with sinusoidal phase modulation and four integrating-buckets," *Journal of the Optical Society of America A*, vol. 18, no. 8, p. 1972, aug 2012. [Online]. Available: https://www.osapublishing.org/abstract.cfm?URI=josaa-18-8-1972

[70] L. L. Deck, "Model-based phase shifting interferometry," *Applied Optics*, vol. 53, no. 21, p. 4628, 2014. [Online]. Available: https://www.osapublishing.org/abstract.cfm?URI=ao-53-21-4628

[71] A. Dubois, L. Vabre, A.-C. Boccara, and E. Beaurepaire, "High-resolution full-field optical coherence tomography with a Linnik microscope," *Applied Optics*, vol. 41, no. 4, p. 805, 2002. [Online]. Available: https://www.osapublishing.org/abstract.cfm?URI=ao-41-4-805

[72] E. P. Goodwin, J. C. Wyant, and Society of Photo-optical Instrumentation Engineers., *Field guide to interferometric optical testing*. SPIE, 2006. [Online]. Available: http://spie.org/Publications/Book/702897?SSO=1#

[73] C. S. Park, "Edge-based intramode selection for depth-map coding in 3D-HEVC," *IEEE Transactions on Image Processing*, vol. 24, no. 1, pp. 155–162, jan 2015. [Online]. Available: http://ieeexplore.ieee.org/document/6966781/

[74] J. Hadamard, "Résolution d'une question relative aux déterminants," *Bulletin des Sciences Mathématiques*, no. 17, pp. 240–246, 1893.

[75] R. E. A. C. Paley, "On Orthogonal Matrices," *Journal of Mathematics and Physics*, vol. 12, no. 1-4, pp. 311–320, apr 1933. [Online]. Available: http://doi.wiley.com/10.1002/sapm1933121311

[76] J. Sylvester, "Thoughts on inverse orthogonal matrices, simultaneous sign-successions, and tessellated pavements in two or more colours, with applications to Newton's rule, ornamental tile-work and the theory of numbers," *The London, Edinburgh, and Dublin Philosophical Magazine and Journal of Science*, vol. 34, no. 232, pp. 461–475, dec 1867. [Online]. Available: https://www.tandfonline.com/doi/full/10.1080/14786446708639914

[77] ViALUX GmbH, "V4100 Technical Reference."